# Reconfigurable wave manipulation in smart cellular solids

A DISSERTATION
SUBMITTED TO THE FACULTY OF THE GRADUATE SCHOOL
OF THE UNIVERSITY OF MINNESOTA
BY

Paolo Celli

IN PARTIAL FULFILLMENT OF THE REQUIREMENTS
FOR THE DEGREE OF
DOCTOR OF PHILOSOPHY

Stefano Gonella, Advisor

July, 2017

# Acknowledgements

Many key figures have helped me succeed in graduate school, from my advisor, to the great teachers I was fortunate to encounter, to colleagues and friends, and to staff members of the Department of Civil, Environmental, and Geo- Engineering and of the University of Minnesota at large. I hope my daily interactions with all these individuals—more than the words written here—have reflected my gratefulness towards them.

Few words in this venue cannot really convey how grateful I am towards my advisor Stefano, for being the best mentor one could ask for and for allowing me to have a fun and fulfilling experience at the University of Minnesota. For many years to come, I plan to remind him how thankful I am for the opportunity he has given me.

The financial support of the National Science Foundation, of my Department through the Sommerfeld Fellowship, and of the University through the Doctoral Dissertation Fellowship is greatly appreciated. Without a steady financial support over the course of these years, my time as a graduate student would have been much more stressful.

I would like to thank professors Bojan Guzina, Henryk Stolarski and Ellad Tadmor for being part of my thesis committee, for patiently answering my many emails and for dedicating me some of their time.

Without a doubt, I will cherish my experience at the University of Minnesota for the rest of my life. This is largely thanks to all the students and postdocs of the Department of Civil, Environmental, and Geo- Engineering, both "old" ones and "new" ones, that crossed paths with me. Thank you guys!

I would like to thank my parents, Lilla and her family. This accomplishment is as much theirs as it is mine. Finally, I would like to thank Peter and Geli; none of this would have happened if it were not for them.

## Abstract

Metamaterials are man-made materials designed to display properties which are not attainable by conventional materials. They owe their behavior to their mesoscale architecture, which often revolves around the periodic arrangement of a repetitive volume element, or unit cell. A particularly prominent application of metamaterials is in the context of wave control, where they have been used as mechanical filters, energy steering devices, and optical and acoustic cloaks. This thesis work tackles a few open problems within this fertile and fast-growing field. Specifically, one of our main aims is to unveil the relationship between the symmetry of the unit cell of a given periodic medium and the symmetry of its wave response, and to provide a mechanistic rationale for the generation of anisotropic wave patterns in specific frequency ranges. We then propose two strategies to modify these patterns in the context of periodic cellular solids (lattice structures). The first strategy, based on the concept of cell symmetry relaxation, relies on a symmetry-driven microstructural design of the unit cell, in which the geometric and material characteristics of certain microstructural features are modulated to modify the symmetry landscape of the cell. The second one, that we named anisotropy overriding, is based on the interplay between the intrinsically anisotropic wave patterns of the medium and the corrective action of a small number of strategically-placed resonators. We also propose tunable implementations of these strategies, which are achieved by incorporating into the periodic architectures smart material inserts (e.g., shunted piezoelectric patches and curlable dielectric elastomers) which are activated using external non-mechanical stimuli. The resulting wave manipulation effects are illustrated through a series of numerical simulations and experimental tests.

# Contents

# List of Tables

# List of Figures

# Chapter 1

# Introduction

## 1.1 An overview of wave propagation in periodic media

Periodic media originate from the spatial repetition of a fundamental unit, called *unit cell* or *repetitive volume element* (RVE). The choice of RVE is not unique. As an example, consider the one-dimensional spring-mass chain shown in Fig. 1.1a. Clearly,

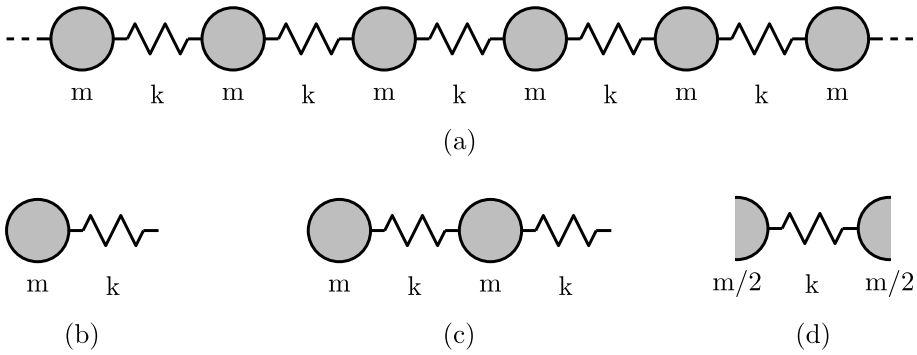


Figure 1.1: (a) A spring-mass chain featuring identical masses and identical springs. (b), (c), (d) Three plausible RVEs for the periodic structure in (a).

the RVEs shown in Figs. 1.1b-d all represent valid alternatives. In general, however, it is convenient to work with an RVE that is irreducible (e.g. Fig. 1.1b or d), i.e. that cannot be divided into smaller RVEs. Many of the characteristics of periodic media can be assessed by studying the behavior of their RVEs, subject to proper periodicity-enforcing boundary conditions.

Periodic or quasi-periodic media are ubiquitous in nature; among many examples, one could mention crystal structures (Fig. 1.2a), honey bee cells (Fig. 1.2b) and compound eyes in arthropods (Fig. 1.2c). Their omnipresence in natural systems, together

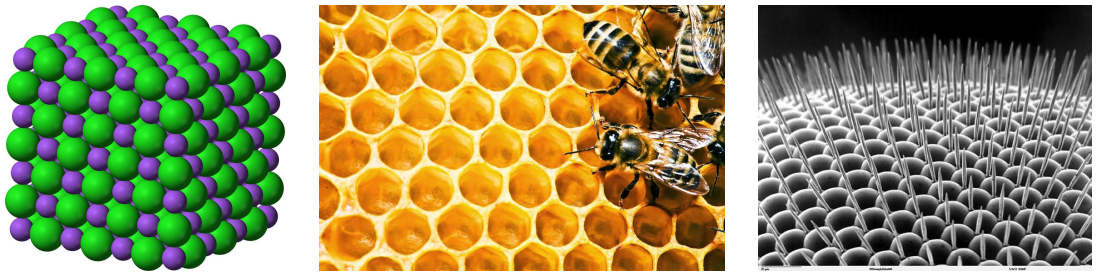

(a) (b) (c)

Figure 1.2: Examples of periodic or quasi-periodic media in nature. (a) Crystal structure of sodium chloride (from en.wikipedia.org/wiki/Crystal_structure). (b) Honey bee cells, or honeycombs (from voices.canonical.com/tag/lxc/). (c) SEM image of a Drosophilidae compound eye (from remf.dartmouth.edu/imagesindex.html).

with humans' innate fascination for order and symmetry, are some of the reasons why scientists have long been interested in their behavior. According to Léon Brillouin, one of the most prominent pioneers of the field of wave propagation in periodic structures, Isaac Newton began to work on a one-dimensional "lattice" in his 1686 *Principia*, in an attempt to derive a formula for the speed of sound [1]. In the Nineteenth century, with the work of Augustin-Louis Cauchy, Baden Powell and Lord Kelvin, and in the early Twentieth century with the work of Max Born, it was discovered that periodic arrangements of particles (chains) behave as frequency-selective mechanical filters. In particular mono-atomic chains, i.e. uniform arrangements of identical springs and masses, behave as *low-pass* filters, while diatomic chains and two- or three-dimensional arrangements of particles behave as *band-pass* filters. In the Twentieth century it was understood that electron states in atomic lattices feature *bandgaps* (forbidden energy gaps), a property that proved to be fundamental in semiconductor physics. Moreover, the discovery that macroscopic periodic media support photonic and phononic bandgaps—frequency ranges in which electromagnetic and mechanical waves, respectively, are filtered—paved the way for the fields of *photonics* [2] and *phononics* [3, 4].

The parallelism between photonic and phononic "crystals" (the term evokes the

crystal-like nature of these systems) is well established, and provides a common theoretical framework for electromagnetic and mechanical wave propagation in periodic media. To date, a vast amount of research efforts has lead to important breakthroughs in the steadily-growing field of photonics, where the desired high frequency/small wavelengths of operation allow for compact and widely applicable devices. On the other hand, the field of phononics has only begun to witness a significant growth in the past decade, fueled by the the so-called "metamaterial revolution" [5]. *Metamaterials* ("meta" in Greek means "beyond") are material systems (often, but not necessarily, periodic), whose internal architecture yields properties that are not attainable by conventional materials available in nature. In the context of electromagnetics, examples of these exotic properties are negative permittivity and permeability [6]. In mechanics, examples are negative elastic moduli [7, 8] and negative effective mass density [9, 10]. In the context of wave control, metamaterials have been shown to elicit effects such as negative refraction, cloaking, focusing, filtering and waveguiding; these effects can extend to the subwavelength regime—at wavelengths that are much larger than the characteristic lengthscales of the medium. This aspect has proven to be especially crucial in phononics, where the frequencies of interest tend to be extremely low and the wavelengths large.

In this introductory Chapter, we illustrate the spectral and spatial wave manipulation capabilities of phononic crystals and metamaterials, in the context of elastodynamics. To this end, we leverage a suite of results obtained through laboratory experiments. We then introduce the concept of tunability and discuss classes of strategies that have been proposed to achieve it. Tunability is essentially the ability of a medium to morph, geometrically and/or functionally, in response to an external stimulus. Finally, we concentrate our attention on a class of periodic media known as cellular structures which, due to their inherent structural and mechanical characteristics, are particularly interesting from an engineering application standpoint.

## 1.2 Phononic crystals and metamaterials

As discussed in the previous Section, *phononic crystals* are periodic media associated with the propagation of mechanical waves. The term "phononic" derives from *phonon*,

i.e. a quantum of atom vibration. Phononic crystals display unique spectral and spatial wave manipulation capabilities, due to their complex, spatially-repeating patterns of mechanical properties. *Acoustic/elastic/mechanical metamaterials*, on the other hand, are non-necessarily-periodic media whose characteristics allow them to overcome some of the limitations of phononic systems. Note that the choice of the materials used to fabricate phononic crystals and metamaterials does not generally affect the availability or nature of their functionalities, but is nevertheless limited by practical constraints: one of the limiting factors is damping, which can affect the wave propagation properties [11] to the extent that large damping values may cause complete suppression of a propagating wave [12], thus impeding the onset of any appreciable phononic effect of interest.

### 1.2.1 Spectral wave manipulation

Phononic crystals possess the ability to spectrally manipulate waves, a phenomenon that manifests in the opening of bandgaps—frequency ranges of forbidden wave propagation—in the crystals' band structures. Bandgaps in phononic crystals are the result of *Bragg* scattering mechanisms due to periodic variations in acoustic impedance in the lattice domain. When the wavelengths involved are comparable in size to the unit cell's characteristic lengthscale, scattered and incident waves interact destructively resulting in effective signal cancellation [1]. In 1993, Kushwaha et al. [3] and Sigalas et al. [4] independently demonstrated the existence of total bandgaps in composite materials—Ni alloy cylinders in an Al alloy background and Au cylinders in Be host, respectively. Note that, unlike partial bandgaps, total or omni-directional bandgaps affect waves with any wave-vector content in the considered domain [12].

A significant limitation to the broad applicability of phononic materials featuring Bragg-type bandgaps as mechanical filters is represented by the "wavelength limit": since the unit cell size ought to be comparable to the excitation wavelength to elicit bandgaps of this type, and since low frequency excitations are associated with large wavelengths, applications at low frequencies typically require impractically-large cell sizes. To overcome this obstacle, scientists are embracing the metamaterial paradigm. Historically, the early use of the term metamaterial is associated with the work of Veselago, who theorized that electromagnetic waves are refracted with negative angles at

the interface between a medium with doubly-negative indices (permittivity and permeability) and a medium with conventional indices [13]. Pendry was later instrumental in identifying an avenue to practically realize these "left-handed" materials (or metamaterials) with doubly-negative properties—a feature that cannot be found in materials available in nature [14]. The first electromagnetic metamaterial was shortly-thereafter fabricated by coupling a periodic dielectric medium with split-ring resonators [6]. Since then, the same term has been used with several different, yet related, connotations. In mechanics, metamaterials are structural materials presenting extraordinary effective mechanical properties (in a homogenized sense), as a result of their carefully-designed *mesoscale architectures*. An example of mechanical metamaterial is an *auxetic* cellular material, which displays an effective negative Poisson's ratio at the global level, as a result of the kinematics of its individual structural components at the mesoscale level [7]. The definition of metamaterial carries an inherent multiscale notion, whereby one can establish mechanistic links between the lower-scale features of the structural constituents and the corresponding properties observed at the macroscale. It is interesting to point out that the constitutive elements of a mechanical metamaterial, taken individually, are often conventional structural elements. However, because of their spatial arrangement and connectivity, the medium enjoys global properties that transcend those of its parts. From a mechanical wave propagation standpoint, metamaterials' outstanding characteristics stem from the availability of negative effective mass density, negative elastic moduli or the combination of the two. In particular, negative effective mass density results from the availability of resonating units and relies on the phase characteristics of their relative motion with respect to the wave carrying medium; this property is associated with the formation of *locally resonant bandgaps*. Liu and coworkers were the first to show the existence of locally resonant gaps for acoustic waves in a periodic structure made by lead spheres coated with silicone rubber [9]. Bandgaps of this type can also be explained invoking Fano-type interference mechanisms [15], whereby a resonator impinged upon by an incident wave stores energy and re-radiates waves into the medium; if the frequency of the incoming wave is slightly larger than its resonance, incoming and re-radiated waves have opposite phase and destructively interfere, causing the opening of a bandgap (which in fact begins at resonance and ends when the amplitude of the resonator spectrum drops); at frequencies right before resonance, on the other hand,

incoming and re-radiated waves interact constructively (this explains the appearance of resonant modes before the bandgap onset). Due to their sole dependence on the characteristics of the resonators, locally resonant bandgaps can occur at wavelengths that are much larger than the size of the RVE. Note that metamaterials need not be periodic, as long as the spatial density and location of the resonating units is chosen as to guarantee sufficiently strong interactions with the incoming waves [16, 17, 18].

To better elucidate the dichotomy between Bragg-based and locally resonant bandgap mechanisms, we resort to in-house experimental results on 2D metamaterial *stubbed plates* [19, 20, 21] created by arranging cylindrical LEGO® bricks on a thin LEGO® baseplate [18]. The bricks, anchored to small protuberances of the baseplate via frictional forces, act as resonating stubs. The response of each metamaterial configuration to a pseudo-random signal is given in terms of its transmission spectrum, which represents a measure of the propagation and attenuation characteristics of the medium (calculated by normalizing the average response near the center of the medium by the response outside the metamaterial). The dense configuration in Fig. 1.3a is made by

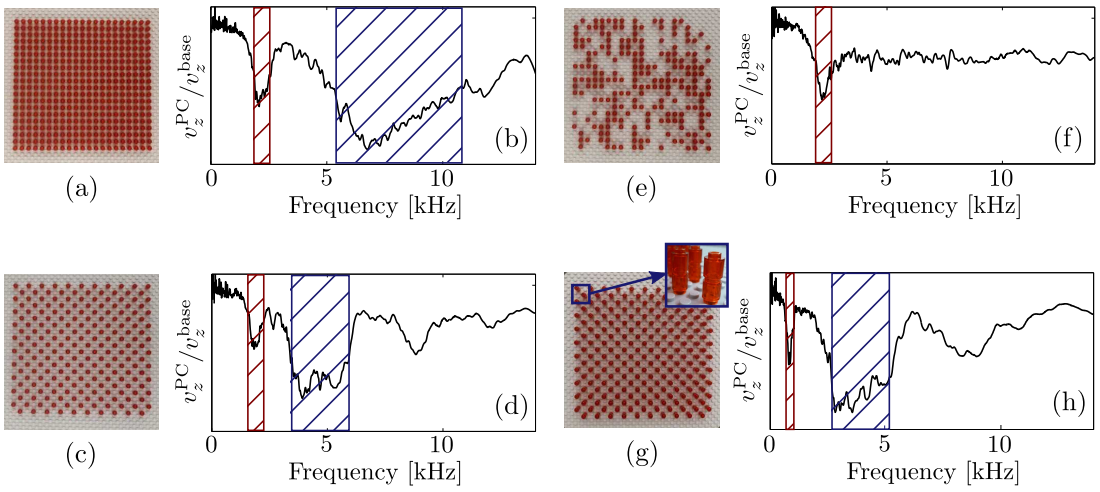


Figure 1.3: Bandgap dichotomy at a glance. (a) Dense periodic configuration: 420 single-stacked, periodically-placed bricks. (c) Coarse periodic configuration: 210 single-stacked, periodically-placed bricks. (e) Random configuration: 210 single-stacked bricks, placed according to a random pattern. (g) Tall coarse periodic configuration: 210 double-stacked, periodically-placed bricks. (b), (d), (f), (h) Experimental transmission spectra for the configurations in (a), (c), (e), (g), respectively.

420 cylindrical bricks organized in a square lattice arrangement. Its transmissibility response, shown in Fig. 1.3b, highlights the presence of two bandgaps (shaded regions). To understand their nature, we test the coarse periodic configuration shown in Fig. 1.3c, characterized by 210 bricks and by a larger unit cell with respect to the dense case. From Fig. 1.3d, we can see that the large high-frequency bandgap shifts towards lower frequencies and becomes narrower; on the other hand, the low-frequency gap is preserved at the same frequencies. Invoking the notion that Bragg bandgaps are sensitive to changes in lattice spacing, while locally resonant bandgaps only depend upon the availability of resonating elements, we conclude that the narrow low-frequency bandgap is locally resonant in nature, while the large high frequency one is of the Bragg type. To further corroborate this statement, we analyze an alternate configuration made by 210 randomly placed bricks (Fig. 1.3e). Its response, shown in Fig. 1.3f, highlights how the low frequency gap survives the periodicity loss, thus confirming its locally resonant nature. Finally, in Fig. 1.3g we analyze a coarse configuration with double-stacked resonators. The response in Fig. 1.3h shows that the locally resonant bandgap shifts due to the lowering of the resonators' natural frequency. In this case, the modification of the high frequency Bragg gap with respect to Fig. 1.3d is due to the inevitable acoustic impedance modification that takes place as we double the resonators' height.

As previously mentioned, bandgaps make periodic media appealing as frequency-selective mechanical filters that can shield sensitive targets from harmful excitations. This property finds application in sound cancellation and noise insulation in mechanical and automotive engineering components, and has been extended to infrastructural engineering applications for seismic isolation. With respect to the latter application, in 2014, Brûlé and coworkers demonstrated in a large scale experiment the applicability of a periodic array of cylindrical empty boreholes as a seismic isolation device [22]. More recently, Krödel et al. introduced metamaterial seismic shields [23], in which the typically-narrow locally resonant bandgap provided by resonating columns immersed in soil is enlarged by resorting to heterogeneous populations of resonators (*rainbow trapping* [24]). More recent work has been devoted to perfecting these techniques in the context of Rayleigh waves [25].

### 1.2.2 Spatial wave manipulation

In addition to their filtering capabilities, phononic crystals and metamaterials also allow for *spatial wave manipulation*. One popular strategy to attain spatially-designable propagation patterns involves the activation of *waveguides* through the realization of phononic crystals or metamaterials operating in bandgap mode and featuring directional paths of defects [26, 27, 28, 29]. This phenomenon is illustrated in Fig. 1.4; once again, simple in-house experiments can be used to effectively demonstrate this concept. The specimen in Fig. 1.4a is obtained by introducing a 2-brick-wide path of defects in

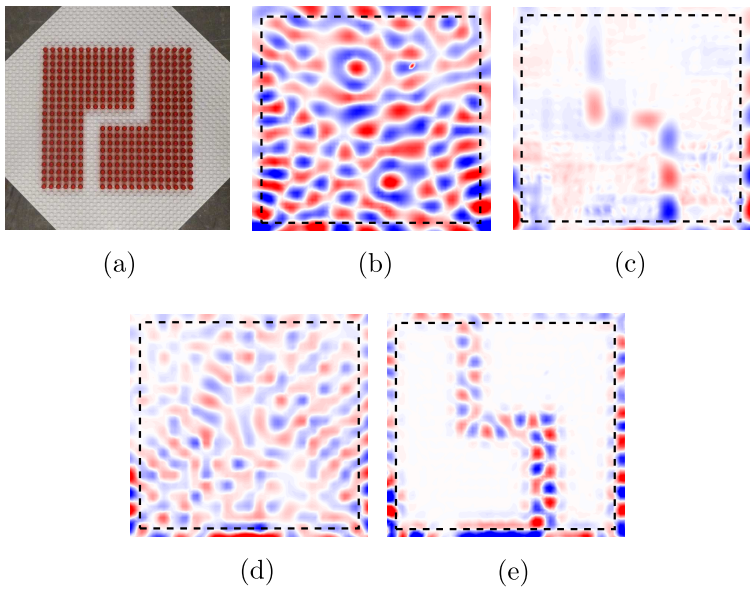


Figure 1.4: Experimental evidence of waveguiding. (a) Dense periodic configuration with a 2-brick-wide waveguide. (b) Waveguide response at 1500 Hz. (c) Waveguide response at 2512.5 Hz. (d) Waveguide response at 4000 Hz. (e) Waveguide response at 7000 Hz. In (b-e) the dashed lines delimit the region occupied by the bricks. Note that the apparent mirroring of the response with respect to the brick arrangement is due to the fact that the wavefields are acquired via laser measurements performed on the back-side of the plate.

the dense architecture shown in Fig. 1.3a. Figs. 1.4b-e represent the velocity wavefields recorded by scanning the rear side of the baseplate with a 3D Scanning Laser Doppler Vibrometer. In particular, Fig. 1.4b and Fig. 1.4d correspond to frequencies within the band-pass regions of the dense configuration (recall Figs. 1.3a-b), while Fig. 1.4c

and Fig. 1.4e correspond to locally resonant and Bragg-based bandgaps, respectively. When the frequency of excitation falls inside one of the bandgaps, waves are forced to propagate along the path of defects, thus activating a waveguide. Waveguides of this type are limited by the fact that they can only be activated within the narrow frequency bands corresponding to total bandgaps of the non-defected configuration. Moreover, for the waveguide to be activated at the low frequencies corresponding to locally resonant bandgaps, the path of defects needs to be wide enough to be "visible" to a long-wavelength wave. Note that recent studies suggest that this constraint can be overcome by inserting, in the defected path, units that resonate when the surrounding medium is in bandgap mode; waveguides of this type are referred to as *subwavelength waveguides* [15, 30].

Additional opportunities for spatial wave manipulation rely on the inherent frequency-dependent anisotropy of the wavefields propagating in phononic crystals and periodic metamaterials, which can be linked to the geometric characteristics of the unit cell. This form of dynamic anisotropy known as *wave directivity* or *directionality* was first investigated by Langley [31] and experimentally demonstrated early on for beam grillages [32]. Later on, other theoretical/numerical studies on the topic were conducted by Ruzzene and coworkers [33, 34, 35], Srikantha Phani and coworkers [36], Casadei and Rimoli [37] and, more recently, by Zelhofer and Kochmann [38]. An experimental work on the topic, dealing with in-plane wave propagation in a regular hexagonal structure and providing the first experimental reconstruction of in-plane anisotropic wave patterns, was produced within our research efforts [39]; the results of this study are summarized in Fig. 1.5. The regular hexagonal specimen used for the experimental investigation is shown in Fig. 1.5a and Fig. 1.5b. The wavefields in Fig. 1.5c and Fig. 1.5d are obtained by measuring the response of the specimen at several locations with a 3D Laser Vibrometer and by spatially interpolating the data at each time instant of the acquisition. Fig. 1.5c, corresponding to a frequency of excitation where the first mode of wave propagation (the S-mode) is dominant, shows pronounced wave anisotropy. On the other hand, the wavefield in Fig. 1.5d, recorded at a higher frequency corresponding to the P-mode, is characterized by waves propagating with circular-crested wavefronts. This type of frequency-dependent wave anisotropy, albeit different in terms of propagation patterns and frequency ranges, is ubiquitously found across periodic structures and

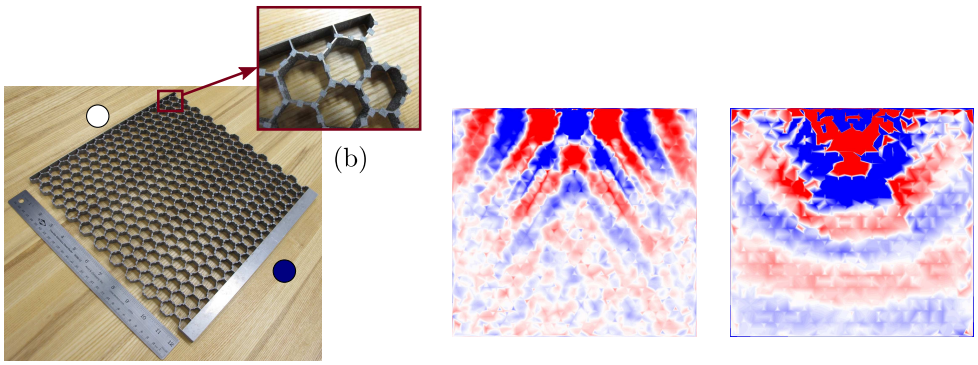


Figure 1.5: Experimental evidence of wave anisotropy. (a) Regular hexagonal lattice specimen. The dark marker highlights the constrained edge, while the lighter one indicates the excitation location. (b) Detail of the specimen. (c) Transient wavefield at one time instant, for a frequency of excitation where the first mode of wave propagation (S-mode) is dominant. (d) Transient wavefield at one time instant, for a frequency of excitation that intersects the second mode of wave propagation (P-mode).

can be leveraged to produce media that behave as *spatial filters*. The main advantage of a spatial manipulation strategy based on a crystal's intrinsic anisotropy lies in its availability at relatively low frequencies. However, a significant drawback is represented by the *stellar*, multi-lobed morphology of the wave propagation patterns: since propagation occurs along multiple radial paths stemming from the excitation point with cyclic symmetry, with the energy being equally partitioned among all the available paths, wave focusing along a single desired direction is not achievable [40]. This prevents the possibility to selectively channel the energy into a single region (or quadrant) of the crystal domain, while de-energizing the others. Note that, if possible, such channelling would be beneficial in the design of acoustic or seismic deflectors (deflecting harmful energy bursts away from sensitive targets) or acoustic radars (probing media along selected directions).

As previously mentioned, electromagnetic metamaterials are historically known to allow for negative refractive indices, a spatial wave phenomenon that also extends to their mechanical counterparts [41, 42]. These unusual refraction characteristics are also attainable in phononic crystals [43, 44, 45]. Negative refraction has been exploited to design media with wave focusing [43, 46] and superlensing [47] (i.e. subwavelength

imaging) capabilities.

## 1.3 Tunable phononic crystals and metamaterials

One of the most daunting limitations of phononic crystals and metamaterials is their inherent passivity. These media are designed to manipulate waves with specific frequency contents; if the operational conditions change, they are incapable of adjusting their functionality to tailor it to the evolved scenario, forcing the user to re-design the medium to operate in the new regime. To overcome these limitations, it is desirable to devise strategies that allow a certain system to adjust its properties based on some externally applied stimulus, i.e. strategies to attain tunable/reconfigurable wave properties. An attempt to provide a taxonomy of the tunability strategies introduced to date is given in Table 1.1. In general, all the reported strategies result in *reversible* modifications of the properties of the medium (e.g. mechanical or geometrical properties) which, consequently, affect its wave propagation behavior. While some strategies introduce a local modification of the medium's characteristics, others produce global effects appreciable at the macroscopic level.

The simplest (and among the first to be introduced) strategy involves the manual adjustment of the position of the constitutive elements of a phononic crystal. This approach was introduced by Goffaux and coworkers [48]; in their theoretical work, the bandgap characteristics of solid-air pillar-based phononic crystals can be modified by rotating the square-cross-sectioned pillars. A neat experimental realization of this concept is carried out in the work of Romero-Garcia et al. [50]. The main advantage of this strategy is its flexibility: since the pillars can be individually rotated, the properties of the medium can be altered to modify the extent and frequency location of bandgaps, or to produce waveguides and cavities with extreme agility. However, this strategy is intrusive, since it requires the user to manually rotate one pillar at a time, and only practical for large-scale specimens. Similarly, in metamaterials featuring periodically-placed fluid-filled Helmholtz resonators, the resonant characteristics of individual resonators can be modified by changing the fluid level. This concept has been demonstrated in a series of ingenious tests involving soda cans filled with water [51] (Fig. 1.6a), and has also been used to demonstrate subwavelength waveguiding [15].

| **Effect** / **Philosophy** | Local properties modification | Global properties modification |
|---|---|---|
| Manual modification of the constituent elements | Individual rotation of anisotropic pillars in solid-solid or solid-air phononic crystals [48, 49, 50]. | |
| | Modification of the characteristics of individually-tunable resonators [51, 15]. | |
| Tuning performed on the active phase of "multi-physics" media | Modification of the equivalent mechanical properties of piezoelectric elements by tuning passive shunting circuits [52, 53, 54, 55, 56, 57, 58, 59, 60, 61, 62, 63]. | Modification of the equivalent mechanical properties of smart material inclusions/phases via external non-mechanical stimuli. Examples: phononic crystals comprising magnetoelastic inclusions [69, 70, 71, 72], electro- and magnetorheological phases [73, 74], shape memory alloys inserts [75], thermally-stimulable polymeric materials [76], aerodynamic-loading-sensitive microstructures [77]. |
| | Modification of the equivalent mechanical properties of electroactive polymer inclusions through electric fields [64, 65, 66, 67, 68]. | |
| Nonlinearity-based tunability | | Shape morphing of bucklable structures via static loads [78, 79, 80, 81], or via magnetic loads in the case of magnetorheological lattices [82]. |
| | | Modification of the intensity of nonlinearity in granular media via precompression [83, 84, 85, 86]. |

Table 1.1: Strategies for tuning the wave characteristics of phononic crystals and metamaterials. Strategies are classified based on their underlying philosophy and on whether they produce local or global properties modifications.

The most popular class of tunability strategies exploits different forms of multi-physical coupling: through non-mechanical stimuli, it is possible to tune the equivalent mechanical properties of certain material phases and, consequently, achieve a modification of the wave characteristics of the whole phononic medium. The first strategy of this kind was introduced by Ruzzene and Baz [75]. In their work, the Young's

(a)

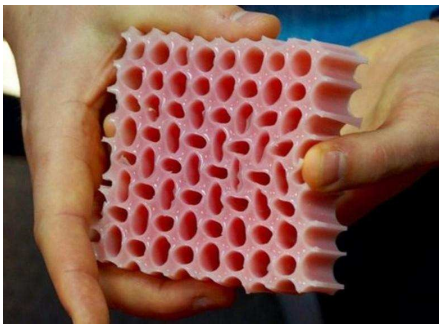

(c)

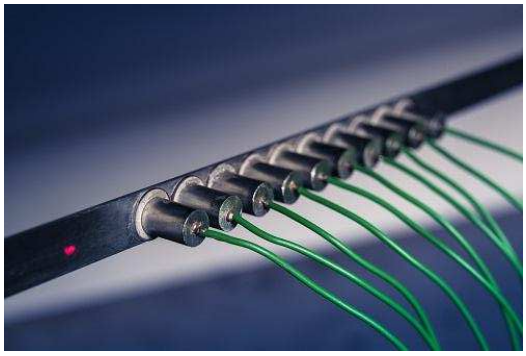

(b)

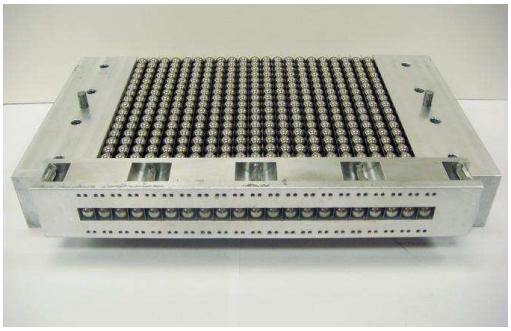

(d)

Figure 1.6: Some of the tunability strategies described in this section. (a) Helmholtz resonators disguised as soda cans (from http://www.nature.com/news/). (b) Periodic array of resonators with piezo-shunted-based tunable connectors (from http://www.opli.net/). (c) Instability-triggered shape change in a polymeric lattice (from www.bbc.com/news/). (d) Granular metamaterial lens to generate sound bullets (from news.nationalgeographic.com/).

modulus of shape memory alloy inserts in a 1D phononic crystal can be adjusted via thermal activation to modify the bandgap characteristics of the medium. Similarly, other coupling phenomena have been investigated and other effects, such as reconfigurable wave directivity, have been attained. In particular, periodic structures with magnetoelastic inclusions [69, 70, 71, 72], electro- and magnetorheological phases [73, 74], thermally-stimulable polymeric materials [76] and aerodynamic-loading-sensitive airfoil-shaped microstructural elements [77] have been proposed. All these strategies follow the same philosophy, aimed at a global modification of the mechanical properties, and require that all the active elements in the medium are activated at the same time. This

could represent an advantage in terms of simplicity of realization, but undermines the achievable flexibility.

To achieve more flexibility, it is convenient to pursue tunability via strategies that produce *localized* modifications of the mechanical properties. To this end, all the active elements in a given metamaterial need to be separately controllable. For example, this is achievable in periodic structures containing piezoelectric elements. By connecting each piezo element to a separate *shunt*—a passive electrical circuit—it is possible to modify the equivalent mechanical modulus of the piezoelectric material [52]; within this paradigm, tuning is achieved by actively modifying the circuits' characteristics. While resonant resistor-inductor (RL) shunts, when connected to a piezoelectric element, behave as electrical resonators and cause the appearance of locally resonant bandgaps in the mechanical response of a periodic system [52, 53, 54, 55, 57, 58, 59, 63], negative capacitance circuits produce mechanical properties variations over large frequency ranges and have been used to tune bandgaps [60] or to spatially manipulate waves [61, 62]. As a representative example of this strategy, we report in Fig. 1.6b the tunable one-dimensional metamaterial realized by Bergamini and coworkers [59], in which the properties of piezoelectric disks connecting beam and resonators can be tuned via RL resonant shunting circuits. Strategies of this sort are extremely flexible, due to the independent controllability of the piezoelectric elements and have therefore been studied in the context of reconfigurable waveguides [56, 58]. A significant drawback is represented by the complexity of these electromechanical systems, that often require the use of many piezoelectric elements (and circuits). Along similar lines, piezoelectric elements have been substituted by electroactive polymer inserts, which can be separately tuned via the application of electric fields to achieve localized modifications of the geometry or mechanical properties [64, 65, 66, 67, 68].

Tunable wave characteristics are also accessible in nonlinear periodic structures, i.e. periodic structures undergoing nonlinear large deformations or whose behavior is governed by nonlinear constitutive relations. For example, a strategy to tune the bandgap properties of soft cellular structures was proposed by Bertoldi and Boyce [78]: the size and shape of the unit cell can be reconfigured by applying an external static load, which causes the buckling of the soft and thin structural constituents, as shown in Fig. 1.6c. An experimental validation of this concept is reported in [80]; this idea has

also been applied to attain reconfigurable wave anisotropy [79]. A similar strategy has also been used by Rudykh and Boyce [81], whereby external loads are used to create instability-induced surface wrinkles in layered media, thus generating reconfigurable periodic patterns with varying wavelengths. Note that strategies based on instability-induced shape modifications affect the structure's properties at a global level, i.e. the whole medium is affected by the external static load.

Another class of nonlinear periodic structures is represented by granular media, where the nonlinearity stems from the Hertzian contact between beads [87]. It is understood that changing the level of precompression of a granular periodic structure causes the intensity of the nonlinear effects to be modified on a global level [88]; this concept has been exploited to produce media with tunable bandgaps [84], wave anisotropy [85] and with tunable wave focusing capabilities [83]. As an example, the tunable acoustic lens proposed by Spadoni and Daraio is shown in Fig. 1.6d. Strategies based on precompression, similarly to what stated for reconfigurable soft lattices, result in global modifications of the characteristics of the medium.

## 1.4 Cellular periodic structures

Over the past few decades, scientists have investigated the wave propagation capabilities of a vast array of periodic architectures. During the 90's, physicists mostly concentrated on arrays of solid pillars immersed in air or water [4, 89] and on bi-material composites [3]. Starting from the discovery of locally resonant bandgap mechanisms in the early 2000's, more and more studies on resonant structures such as stubbed plates have been reported [19, 20, 21, 17, 18]. Plates with periodic patterns of stubs/pillars allow for both locally resonant and Bragg bandgaps, and they also allow for flexibility in the choice of pillar height. A class of periodic structures that has received noteworthy attention for engineering applications consists of *cellular periodic structures*, sometimes referred to as *lattice structures*, i.e. "regular" porous media in which the principal constituents are thin beams or *struts*. From a static standpoint, cellular structures occupy regions of the material property space that are forbidden to fully dense solids (e.g. regions corresponding to high stiffness, strength or fracture toughness at low density [90]). Cellular structures are often bio-inspired: since the time of R. Hooke and his *Micrographia*, it

has been observed that materials such as cork owe their uncommon properties to their cellular microstructure (see Fig. 1.7a). While the first man-made cellular structures

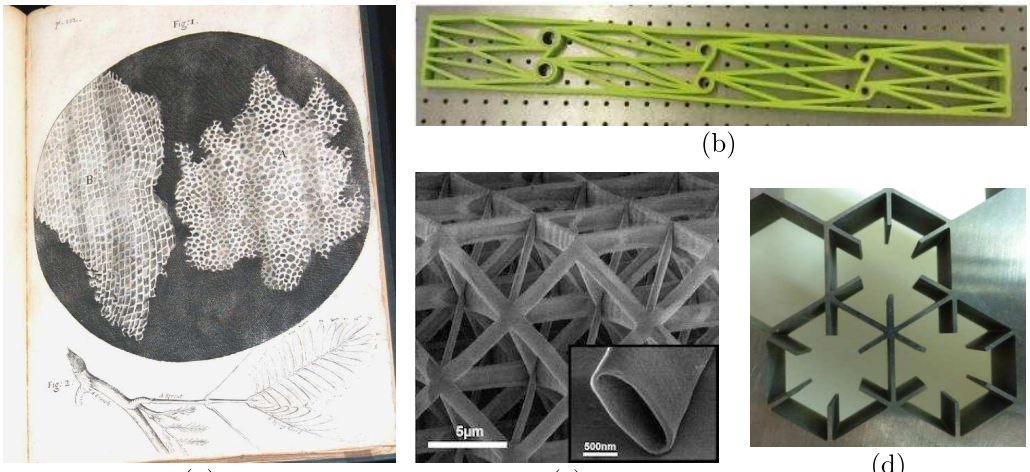


(a) (b) (c) (d)

Figure 1.7: Few of the cellular structures discussed in this section. (a) Robert Hooke's sketch of the cellular microstructure of cork (from www.nlm.nih.gov/). (b) Beam with chiral lattice microstructure (from [91]). (c) SEM detail of a hollow-tube aluminum oxide nanolattice (from ceramics.org/ceramic-tech-today/). (d) Detail of few regular hexagonal lattice cells with cantilever beams acting as auxiliary resonators.

to be investigated were random foams, there has been a recent interest shift towards ordered, "architected" cellular structures. Synthetic, perfectly-periodic lattices, like the one shown in Fig. 1.7c, have gained much attention in recent years, due to their extraordinary light-weight characteristics [92, 93] and their ability to recover their shape after static load removal [94].

The first published results on the wave propagation behavior of "beam grillages" (a synonym for lattice structures) are those authored by Langley and coworkers [32]; in their paper, the authors resort to roving accelerometers to study the wave anisotropy of square lattice structures. Martinnsson and Movchan, a few years later, discussed the locally resonant bandgap behavior of regular hexagonal lattice structures presenting resonating microstructures inside their cells [95]. Much research on the topic has been carried out by Ruzzene and coworkers, including studies on wave propagation in sandwich panels with periodic cellular cores [96, 97], further studies on wave anisotropy [33, 34], on chiral [98] and undulated lattice structures [99], and an experimental demonstration

of the bandgap behavior of square lattices [100]. One of the seminal contributions to the topic is the work of Srikantha Phani et al. [36], describing the bandgap and anisotropy characteristics of common lattice structures, with architectures ranging from square to Kagome to hexagonal. Another interesting work on the topic is that of Gonella et al. [101], in which auxiliary resonators with embedded piezoelectric elements are located inside the hollow cells of a lattice to modify the bandgap characteristics and harvest vibrational energy. The effect of auxiliary microstructural elements and lumped masses is also discussed in the work of Krödel et al. [102], while the effects of variations in the lattice connectivity are discussed in the articles of Baravelli and Ruzzene [91] (one of their beam specimens with chiral microstructure is shown in Fig. 1.7b) and Wang et al. [103]. Locally-resonant fluid-filled poroelastic metamaterials have also been studied in the past few years by Spadoni and coworkers [104]. Also, "smart" lattices with piezoelectric [61] and magnetoelastic inclusions [71, 72], and magnetorheological lattices [82] have been studied for their tunable wave properties. Moreover, most of the mechanically-tunable metamaterials discussed in Section 1.3 are soft lattice structures [78, 80]. Recently, nanolattices have also been studied from an electromagnetic wave propagation standpoint and have been shown to display mechanically-induced tunable photonic bandgaps [105].

While the brief literature review in the previous paragraph should have already made the case for the popularity of cellular phononic crystals and metamaterials, it is worth spending few words on the advantages presented by such architectures. First and foremost, at least as far as metallic lattices are concerned, choosing cellular designs allows to integrate the wave manipulating medium within other, larger structural systems. For example, they can be used as core of sandwich panels [97] and airfoils [106]. Other advantages are available for all cellular structures: due to the extremely high impedance mismatch between the constitutive material and air, waves are forced to follow the path dictated by the lattice links, allowing for more extreme wave anisotropy patterns than in other periodic media. The thin lattice struts also prove to be fundamental when trying to achieve shape-switching via external loads, due to their bucklable nature. Classical lattice structures are inherently non-resonant. However, chiral architectures [35, 107] and architectures featuring nodal masses [103] have been shown to possess locally-resonant bandgaps. Moreover, their void-dominated architectures allow

for the introduction of *auxiliary* microstructural elements that are external to the main periodic lattice, i.e. auxiliary to the main wave-carrying medium [101]. An example is represented by cantilever beams placed at the nodal locations of a regular hexagonal lattice, as shown in Fig. 1.7d. The fact that auxiliary resonators can be added to a given lattice without dramatically changing its static characteristics represents one of the unique aspects of cellular media.

## 1.5 Motivation and outline

More than twenty years after their discovery, phononic crystals and metamaterials are still broadly viewed as "bandgap materials". The attention devoted to spatial wave manipulation is on the rise, but only few of the current research efforts are devoted to harnessing and enhancing the wave anisotropy inherent to periodic architectures. The aim of this dissertation work is two-fold. On one hand, we propose a symmetry breaking based framework to alter the anisotropic wave propagation patterns established across the frequency spectra of periodic cellular media, with the aim of obtaining highly beamed and strongly asymmetric wave patterns. A second and broader objective is to explore tunable modifications of the wave characteristics of phononic media (with special attention to cellular architectures) through the integration of externally-controllable smart material inserts.

This dissertation is organized as follows. In Chapter 2, we discuss some fundamental aspects of the wave propagation behavior of periodic cellular media, seen through the framework of unit cell analysis. We especially discuss the anisotropy of the wavefields that can be excited at low frequencies. In Chapter 3, we introduce two strategies to enhance the wave anisotropy characteristics of periodic cellular solids: *symmetry relaxation* and *anisotropy overriding*. In Chapter 4, we present an avenue for tunable wave anisotropy, based on the concept of relaxed cell symmetry in lattice structures with smart auxiliary cantilevers. Each cantilever features piezoelectric patches shunted with negative capacitance circuits; tuning the circuits allows to locally alter the equivalent mechanical properties of the cantilevers and, therefore, the global wave anisotropy characteristics of the medium. At the end of this Chapter, we briefly mention another

avenue towards tunable relaxed cell symmetry, enabled by soft lattices with smart cantilevers featuring electroactive polymer inserts. By applying a voltage to one of the cantilevers, it is possible to attain localized shape modifications that alter the resonant characteristics of the cantilevers and, as a consequence, affect the global wave propagation properties of the medium. Note that all the results discussed up to this point are theoretical/numerical in nature. In Chapter 5, we discuss a tunable experimental implementation of the idea of anisotropy overriding by means of tunable electromechanical resonators. The resonators comprise a piezoelectric patch and a resistor-inductor shunting circuit. First, we analyze the behavior of a single resonator attached to a one dimensional beam/waveguide. We then analyze the interplay of several resonators with the dispersion characteristics of a square lattice structure. Finally, the conclusions of this dissertation, together with the discussion of possible avenues for future work on this topic, are presented in Chapter 6.

# Chapter 2

# Wave propagation in periodic cellular structures

## 2.1 Unit cell analysis

The wave propagation behavior of any macroscopic periodic structure can be studied through the application of Bloch's theorem, which was originally developed to describe the conduction of electrons in three-dimensional crystalline solids [1]. Through Bloch's theorem, we can infer the behavior of infinitely-extended periodic media by analyzing a single unit cell and applying periodic boundary conditions which account for the harmonic nature of the waves involved. Note that, to completely characterize any medium from a wave propagation standpoint, independently from the type of waves involved, it is sufficient to compute its *dispersion relation*, i.e. a relationship between wave properties (e.g. frequency and wavenumber). In other words, a dispersion relation is the "wave propagation portrait" of a given structure. All the techniques to compute the dispersion relation of a periodic medium, i.e. to perform a *unit cell analysis*, leverage some form of Bloch's theorem [1]. The most popular techniques are the transfer matrix (TM) method, which is exact, the plane wave expansion method (PWE) and the finite element (FE)-based method, which are both approximate. A brief discussion of all these techniques can be found in the review article by Hussein et al. [11]. In the following, we resort to a FE-based method, which allows to treat unit cells of arbitrarily complex shape.

## 2.2 The benchmark problem of a 2D hexagonal lattice

In this work, we discuss several two-dimensional lattice architectures. Among others, the one we use most extensively is the regular hexagonal (RH) lattice. For this reason, we use this architecture as benchmark to explain the procedure and outcomes of a unit cell analysis based on Bloch's theorem coupled to the FE method. Note that, even if we consider the same architecture, the unit cell depends on the type of element we use for the FE analysis; the one in Fig. 2.1a is one of the possible RVE choices if the links are modeled as beam elements, while the one in Fig. 2.1b is the RVE in the case of a 2D elasticity model. The drawings in Fig. 2.1 also indicate the main dimensions of the

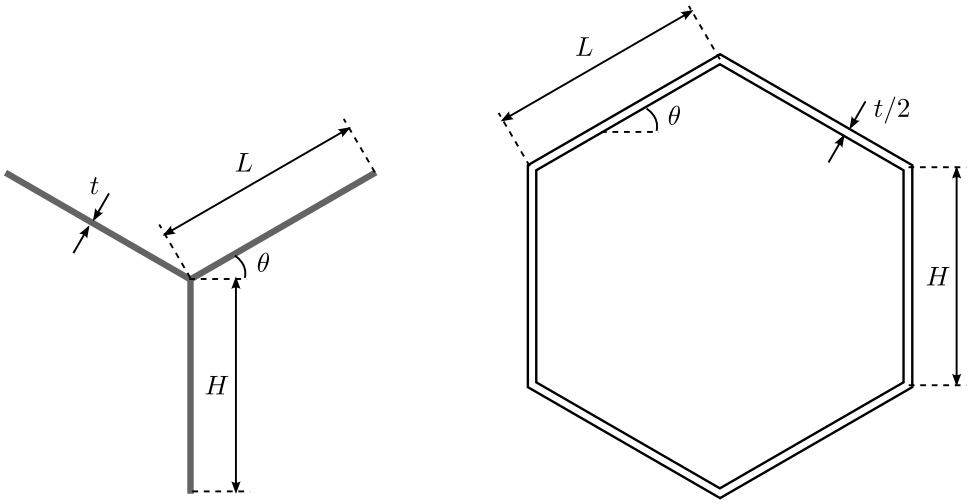


Figure 2.1: Unit cells of a regular hexagonal lattice: (a) when the struts are modeled as beams; (b) when a 2D elasticity model is used.

two models. Note that, in the case of a RH lattice, $H = L$ and $\theta = \pi/6$. From this point on, we only consider the lattice modeled with beam elements, i.e. the unit cell in Fig. 2.1a. Note that, with a few modifications, this procedure can be applied to unit cells of any shape and size.

We now introduce three useful vector bases, which are drawn on a discretized unit cell in Fig. 2.2. A Cartesian (rectilinear) coordinate system is defined by the orthonormal vector basis $\mathbf{i}_i$, with $i = 1, 2$ (with $x_i$ directed along $\mathbf{i}_i$). We define the non-orthogonal

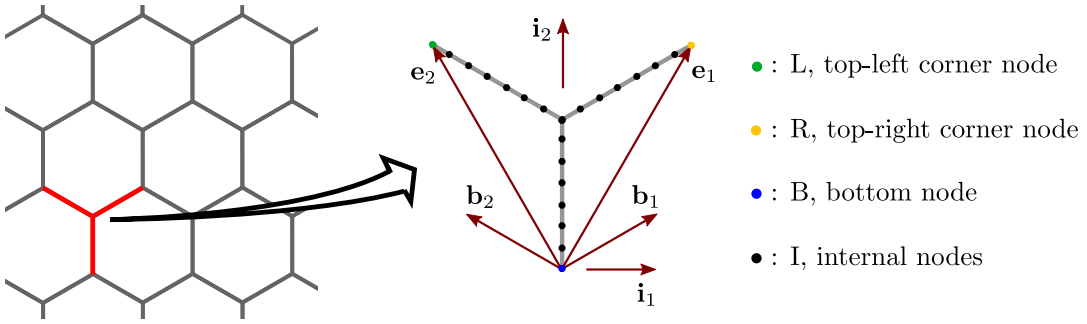


Figure 2.2: Unit cell of a RH lattice, with struts modeled as beams. The dots represent the nodes of a hypothetical FE mesh. The node nomenclature shown here will be used throughout this section. The arrows represent vectors belonging to bases of interest for the unit cell analysis.

*direct lattice* vector basis $\mathbf{e}_i$ as the one that comprises the lattice vectors, i.e. vectors that connect material points whose relative position within a unit cell is the same. For the RH lattice, projecting $\mathbf{e}_i$ on $\mathbf{i}_i$, we obtain

$$\mathbf{e}_1 = L\cos\theta\,\mathbf{i}_1 + (H + L\sin\theta)\,\mathbf{i}_2 = \frac{\sqrt{3}L}{2}\,\mathbf{i}_1 + \frac{3L}{2}\,\mathbf{i}_2 \quad , \tag{2.1}$$

$$\mathbf{e}_2 = -L\cos\theta\,\mathbf{i}_1 + (H + L\sin\theta)\,\mathbf{i}_2 = -\frac{\sqrt{3}L}{2}\,\mathbf{i}_1 + \frac{3L}{2}\,\mathbf{i}_2 \quad . \tag{2.2}$$

We now define $n_1$ and $n_2$, integers that identify an arbitrary cell of the lattice. They correspond to the number of translations along the directions of vectors $\mathbf{e}_1$ and $\mathbf{e}_2$, respectively, that are needed, starting from the $(0,0)$ reference cell, to obtain the $(n_1, n_2)$ cell. The position of any point P of the lattice with respect to the origin of the Cartesian coordinate system can be expressed as a function of the position of its corresponding point in the reference cell:

$$\boldsymbol{\rho}^{\mathrm{P}}(n_1, n_2) = \mathbf{r}^{\mathrm{P}}(0,0) + n_1\mathbf{e}_1 + n_2\mathbf{e}_2 \quad . \tag{2.3}$$

Note that "corresponding" means that the two points occupy the same location within their respective unit cells. To avoid confusion, $\mathbf{r}^{\mathrm{P}}$ is the position vector of the point belonging to the reference cell and $\boldsymbol{\rho}^{\mathrm{P}}$ is the position of the point of the translated cell.

We now introduce the *reciprocal lattice* basis $\mathbf{b}_i$, which is dual to $\mathbf{e}_i$ and, therefore, satisfies

$$\mathbf{b}_i \cdot \mathbf{e}_j = \delta_{ij} \quad , \tag{2.4}$$

where $\delta_{ij}$ is the *Kronecker* delta. From Eq 2.4, $\mathbf{b}_1 \perp \mathbf{e}_2$ and vector $\mathbf{b}_2 \perp \mathbf{e}_1$. Projecting $\mathbf{b}_i$ on $\mathbf{i}_i$ in the RH lattice case, we obtain

$$\mathbf{b}_1 = \frac{1}{2L\cos\theta}\,\mathbf{i}_1 + \frac{1}{2(H+L\sin\theta)}\,\mathbf{i}_2 = \frac{1}{\sqrt{3}L}\,\mathbf{i}_1 + \frac{1}{3L}\,\mathbf{i}_2 \quad , \tag{2.5}$$

$$\mathbf{b}_2 = -\frac{1}{2L\cos\theta}\,\mathbf{i}_1 + \frac{1}{2(H+L\sin\theta)}\,\mathbf{i}_2 = -\frac{1}{\sqrt{3}L}\,\mathbf{i}_1 + \frac{1}{3L}\,\mathbf{i}_2 \quad . \tag{2.6}$$

It is also useful to define transformation matrices that allow to move between vector bases and between coordinate systems. Matrix $\mathbf{D}$ contains the projections of $\mathbf{e}_1$ and $\mathbf{e}_2$ along $\mathbf{i}_1$ and $\mathbf{i}_2$, i.e. it relates the orthonormal vector basis to the direct lattice one:

$$\begin{bmatrix}\mathbf{e}_1\\ \mathbf{e}_2\end{bmatrix} = \begin{bmatrix}\mathbf{D}\end{bmatrix}\begin{bmatrix}\mathbf{i}_1\\ \mathbf{i}_2\end{bmatrix} = \begin{bmatrix}\mathbf{e}_1\cdot\mathbf{i}_1 & \mathbf{e}_1\cdot\mathbf{i}_2\\ \mathbf{e}_2\cdot\mathbf{i}_1 & \mathbf{e}_2\cdot\mathbf{i}_2\end{bmatrix}\begin{bmatrix}\mathbf{i}_1\\ \mathbf{i}_2\end{bmatrix} = \begin{bmatrix}\frac{\sqrt{3}L}{2} & \frac{3L}{2}\\ -\frac{\sqrt{3}L}{2} & \frac{3L}{2}\end{bmatrix}\begin{bmatrix}\mathbf{i}_1\\ \mathbf{i}_2\end{bmatrix} \quad . \tag{2.7}$$

Matrix $\mathbf{D}^*$ relates the orthonormal vector basis to the reciprocal lattice one:

$$\begin{bmatrix}\mathbf{b}_1\\ \mathbf{b}_2\end{bmatrix} = \begin{bmatrix}\mathbf{D}^*\end{bmatrix}\begin{bmatrix}\mathbf{i}_1\\ \mathbf{i}_2\end{bmatrix} = \begin{bmatrix}\mathbf{b}_1\cdot\mathbf{i}_1 & \mathbf{b}_1\cdot\mathbf{i}_2\\ \mathbf{b}_2\cdot\mathbf{i}_1 & \mathbf{b}_2\cdot\mathbf{i}_2\end{bmatrix}\begin{bmatrix}\mathbf{i}_1\\ \mathbf{i}_2\end{bmatrix} = \begin{bmatrix}\frac{1}{\sqrt{3}L} & \frac{1}{3L}\\ -\frac{1}{\sqrt{3}L} & \frac{1}{3L}\end{bmatrix}\begin{bmatrix}\mathbf{i}_1\\ \mathbf{i}_2\end{bmatrix} \quad . \tag{2.8}$$

Calling $(\eta_1,\ \eta_2)$ the coordinates of a point in the direct lattice coordinate system and $(x_1,\ x_2)$ the coordinates of the same point in the Cartesian coordinate system, these sets of coordinates are related through $\mathbf{E}$:

$$\begin{bmatrix}x_1\\ x_2\end{bmatrix} = \begin{bmatrix}\mathbf{E}\end{bmatrix}\begin{bmatrix}\eta_1\\ \eta_2\end{bmatrix} = \begin{bmatrix}\mathbf{e}_1\cdot\mathbf{i}_1 & \mathbf{e}_2\cdot\mathbf{i}_1\\ \mathbf{e}_1\cdot\mathbf{i}_2 & \mathbf{e}_2\cdot\mathbf{i}_2\end{bmatrix}\begin{bmatrix}\eta_1\\ \eta_2\end{bmatrix} = \begin{bmatrix}\frac{\sqrt{3}L}{2} & -\frac{\sqrt{3}L}{2}\\ \frac{3L}{2} & \frac{3L}{2}\end{bmatrix}\begin{bmatrix}\eta_1\\ \eta_2\end{bmatrix} \quad . \tag{2.9}$$

Calling $(\chi_1,\ \chi_2)$ the coordinates of a point in the reciprocal lattice coordinate system and $(x_1,\ x_2)$ the coordinates of the same point in the Cartesian coordinate system, these sets of coordinates are related through $\mathbf{E}^*$:

$$\begin{bmatrix}x_1\\ x_2\end{bmatrix} = \begin{bmatrix}\mathbf{E}^*\end{bmatrix}\begin{bmatrix}\chi_1\\ \chi_2\end{bmatrix} = \begin{bmatrix}\mathbf{b}_1\cdot\mathbf{i}_1 & \mathbf{b}_2\cdot\mathbf{i}_1\\ \mathbf{b}_1\cdot\mathbf{i}_2 & \mathbf{b}_2\cdot\mathbf{i}_2\end{bmatrix}\begin{bmatrix}\chi_1\\ \chi_2\end{bmatrix} = \begin{bmatrix}\frac{1}{\sqrt{3}L} & -\frac{1}{\sqrt{3}L}\\ \frac{1}{3L} & \frac{1}{3L}\end{bmatrix}\begin{bmatrix}\chi_1\\ \chi_2\end{bmatrix} \quad . \tag{2.10}$$

It can be also proved that, in the case of a RH lattice, $\mathbf{E} = \mathbf{D}^T$, $\mathbf{E}^* = \mathbf{D}^{*T}$, $\mathbf{E}^*\mathbf{E}^T = \mathbf{I}$ and $\mathbf{D}^*\mathbf{D}^T = \mathbf{I}$.

## 2.3 Wave propagation and Bloch's theorem

After defining the geometry of the unit cell, we now begin our treatment of elastic wave propagation. Considering the response to a harmonic wave with frequency $\omega$, the displacement of a point P of the reference unit cell is

$$\mathbf{w}(\mathbf{r}^{\mathrm{P}}) = \mathbf{w}^{\mathrm{P}_0} e^{i(\omega t - \mathbf{k}\cdot\mathbf{r}^{\mathrm{P}})} \quad , \tag{2.11}$$

where $\mathbf{w}^{\mathrm{P}_0}$ is a vector of amplitudes and $\mathbf{k}$ is the wave vector, whose modulus is the wave number $k = |\mathbf{k}| = 2\pi/\lambda$, reciprocal of the wavelength $\lambda$ and such that $[k] = \mathrm{rad\,m^{-1}}$. Note also that $t$ indicates time and $\omega$ is the angular frequency. Similarly, the displacement of the point corresponding to P and belonging to the $(n_1, n_2)$ cell is

$$\mathbf{w}(\boldsymbol{\rho}^{\mathrm{P}}) = \mathbf{w}^{\mathrm{P}_0} e^{i(\omega t - \mathbf{k}\cdot\boldsymbol{\rho}^{\mathrm{P}})} \quad . \tag{2.12}$$

Eq. 2.12 can be manipulated by substituting the expression for $\boldsymbol{\rho}^{\mathrm{P}}$ (Eq. 2.3) and by projecting the wave vector along one of the vector bases. Decomposing $\mathbf{k}$ on the reciprocal lattice vector basis, we obtain

$$\mathbf{k} = \xi_1 \mathbf{b}_1 + \xi_2 \mathbf{b}_2 \quad . \tag{2.13}$$

Since $\mathbf{b}_i$ have dimensions of $\mathrm{m^{-1}}$, it follows that $[\xi_1] = [\xi_2] = \mathrm{rad}$. As written in Eq. 2.13, $\xi_1$ and $\xi_2$ are components of the vector $\mathbf{k}$ in the reciprocal lattice coordinate system. Additionally, they are also the components of $\mathbf{k}$ along the directions of vectors $\mathbf{e}_1$ and $\mathbf{e}_2$. In fact, using Eq. 2.4 and Eq. 2.13, we have

$$\mathbf{e}_1 \cdot \mathbf{k} = \xi_1 \mathbf{b}_1 \cdot \mathbf{e}_1 + \xi_2 \mathbf{b}_2 \cdot \mathbf{e}_1 = \xi_1 \quad , \tag{2.14}$$

$$\mathbf{e}_2 \cdot \mathbf{k} = \xi_1 \mathbf{b}_1 \cdot \mathbf{e}_2 + \xi_2 \mathbf{b}_2 \cdot \mathbf{e}_2 = \xi_2 \quad . \tag{2.15}$$

Now, substituting Eq. 2.3 and Eq. 2.13 into Eq. 2.12, we obtain

$$\mathbf{w}(\boldsymbol{\rho}^{\mathrm{P}}) = \mathbf{w}^{\mathrm{P}_0} e^{i(\omega t - (\xi_1 \mathbf{b}_1 + \xi_2 \mathbf{b}_2)\cdot(\mathbf{r}^{\mathrm{P}} + n_1 \mathbf{e}_1 + n_2 \mathbf{e}_2))} \quad . \tag{2.16}$$

We now develop the dot product at the exponent and we apply all the proper simplifications. Note that, if we were to choose a different basis other than the reciprocal one

to decompose $\mathbf{k}$, many of these simplifications wouldn't have been possible. By defining the components of $\mathbf{r}^{\mathrm{P}}$ in the reciprocal lattice coordinate system as $\mathbf{b}_1 \cdot \mathbf{r}^{\mathrm{P}} = \eta_1$ and $\mathbf{b}_2 \cdot \mathbf{r}^{\mathrm{P}} = \eta_2$, we can write

$$\mathbf{w}(\boldsymbol{\rho}^{\mathrm{P}}) = \mathbf{w}^{\mathrm{P}_0} e^{i(\omega t - \xi_1\eta_1 - \xi_2\eta_2)} e^{-i(\xi_1 n_1 + \xi_2 n_2)} = \mathbf{w}(\mathbf{r}^{\mathrm{P}}) e^{-i(\xi_1 n_1 + \xi_2 n_2)} \quad . \tag{2.17}$$

This equation can be seen as an expression of Bloch's theorem and it can be generalized in the following way:

$$\mathbf{w}\left(\boldsymbol{\rho}^{\mathrm{P}}(n_1+1, n_2+1), t\right) = \mathbf{w}\left(\boldsymbol{\rho}^{\mathrm{P}}(n_1, n_2), t\right) e^{-i(\xi_1+\xi_2)} \qquad \forall n_1,\, n_2 \in \mathbb{Z} \quad . \tag{2.18}$$

From this expression of Bloch's theorem, we can see that the solution of the wave propagation problem is periodic in the lattice. Thus, once we apply some periodic boundary conditions, we can evince the wave behavior of a periodic structure having infinite dimensions by studying its unit cell.

## 2.4 Finite element-based unit cell analysis

As previously mentioned, in this work we couple Bloch's theorem and a FE model of the unit cell. Within the RH lattice example, we consider the hypothetical element discretization shown in Fig. 2.2. For the $i$-th node, where $i = 1, ..., m$ ($m$ is the total number of nodes in the unit cell model), we define $\mathbf{u}_i$ as the vector of nodal degrees of freedom. Resorting to a Timoshenko beam model, this vector comprises $\mathbf{u}_i = (u_{x_1},\, u_{x_2},\, \phi)^T$, i.e. the displacement components in the Cartesian coordinate system and the angle of rotation of the beam's cross section. For the whole system, we let the vector of degrees of freedom be organized in the following manner:

$$\mathbf{u} = (\mathbf{u}_{\mathrm{B}},\, \mathbf{u}_{\mathrm{I}},\, \mathbf{u}_{\mathrm{L}},\, \mathbf{u}_{\mathrm{R}})^T \quad , \tag{2.19}$$

where we followed the node nomenclature indicated in the legend of Fig. 2.1. We then write the following discrete eigenvalue problem to obtain the free response of the system:

$$(\mathbf{K} - \omega^2 \mathbf{M})\mathbf{u} = \mathbf{0} \quad , \tag{2.20}$$

where $\mathbf{M}$ and $\mathbf{K}$ are the mass and stiffness matrices of the unit cell, respectively, and $\omega$ is the frequency in rad/s. The size of this eigenvalue problem can be reduced if we

consider that, due to the periodicity of the lattice, some of the boundary nodes of the unit cell model are related through Bloch's theorem. In this specific case, the vectors of nodal degrees of freedom for nodes R and L are related to node B. In particular, since node L can be obtained from B via the translation $0\mathbf{e}_1 + 1\mathbf{e}_2$, i.e. setting the translation indices to $n_1 = 0$ and $n_2 = 1$, we can use Eq. 2.17 to write $\mathbf{u}_\mathrm{L} = \mathbf{u}_\mathrm{B} e^{-i\xi_2}$. Similarly, $\mathbf{u}_\mathrm{R} = \mathbf{u}_\mathrm{B} e^{-i\xi_1}$. In light of these observations, the dynamics of the unit cell can be described via a reduced vector of degrees of freedom $\mathbf{u}_r = (\mathbf{u}_\mathrm{B},\, \mathbf{u}_\mathrm{I})^T$, such that

$$\mathbf{u} = \mathbf{W}\mathbf{u}_r \quad . \tag{2.21}$$

For the specific case of a RH lattice discretized with beam elements as in Fig. 2.2, matrix $\mathbf{W}$ can be written as

$$\mathbf{W} = \begin{bmatrix} [\mathbf{I}]_{\mathrm{nB}\times\mathrm{nB}} & [\mathbf{0}]_{\mathrm{nB}\times\mathrm{nI}} \\ [\mathbf{0}]_{\mathrm{nI}\times\mathrm{nB}} & [\mathbf{I}]_{\mathrm{nI}\times\mathrm{nI}} \\ [\mathbf{I}\cdot e^{-i\xi_2}]_{\mathrm{nL}\times\mathrm{nB}} & [\mathbf{0}]_{\mathrm{nL}\times\mathrm{nI}} \\ [\mathbf{I}\cdot e^{-i\xi_1}]_{\mathrm{nR}\times\mathrm{nB}} & [\mathbf{0}]_{\mathrm{nR}\times\mathrm{nI}} \end{bmatrix} \quad , \tag{2.22}$$

where the dimensions of the sub-matrices are reported as subscripts, where $\mathbf{I}$ is the identity matrix, $\mathbf{0}$ is the zero matrix and where nB, nI, nL and nR represent the number of nodes in each subgroup. Note that the number of nodes in groups related via Bloch's theorem needs to be the same, i.e. $\mathrm{nR} = \mathrm{nL} = \mathrm{nB}$.

Substituting Eq. 2.21 into Eq. 2.20 and pre-multiplying by the Hermitian transpose of matrix $\mathbf{W}$ to preserve the square nature of the matrices involved, we obtain

$$\left(\mathbf{W}^H\mathbf{K}\mathbf{W} - \omega^2\mathbf{W}^H\mathbf{M}\mathbf{W}\right)\mathbf{u}_r = \mathbf{0} \quad . \tag{2.23}$$

Defining the reduced mass and stiffness matrices as

$$\mathbf{M}_r(\xi_1,\xi_2) = \mathbf{W}^H\mathbf{M}\mathbf{W} \;, \quad \mathbf{K}_r(\xi_1,\xi_2) = \mathbf{W}^H\mathbf{K}\mathbf{W} \quad , \tag{2.24}$$

we obtain the reduced eigenvalue problem:

$$\left(\mathbf{K}_r(\xi_1,\xi_2) - \omega^2\mathbf{M}_r(\xi_1,\xi_2)\right)\mathbf{u}_r = \mathbf{0} \quad . \tag{2.25}$$

## 2.5 The dispersion relation

The dispersion relation $\omega(\xi_1, \xi_2)$ of any periodic medium can be obtained by solving the eigenvalue problem in Eq. 2.25. First of all, we consider an array of $(\xi_1, \xi_2)$ values that spans the region of interest in the reciprocal lattice coordinate system. For any pair of $(\xi_1, \xi_2)$, we solve the reduced eigenproblem and obtain as many roots, i.e. values of $\omega$, as the dimension of the eigenproblem itself. Connecting the values of $\omega(\xi_1, \xi_2)$ that correspond to the same root (e.g. first, second and so on), we obtain a "root locus" called *dispersion surface*. Note that, in general, any frequency versus wave vector function is a dispersion relation. Due to the 1-to-1 mapping between components of the wave vector $\mathbf{k}$ in the reciprocal lattice coordinate system $(\xi_1, \xi_2)$ and in the Cartesian coordinate system $(k_1, k_2)$, regulated by matrix $\mathbf{E}^T$, we can map $\omega(\xi_1, \xi_2)$ to $\omega(k_1, k_2)$; the latter provides a better representation of the wave behavior along physical directions. The first three surfaces of the $\Omega(k_1 L, k_2 L)$ dispersion relation for a RH lattice are shown in Fig. 2.3. Note that $L$, the length of a lattice strut, is used to non-dimensionalize $k_1$ and $k_2$. Also, the result shown in Fig. 2.3 and all other results in this section correspond to an Aluminum lattice ($E = 71\,\mathrm{GPa}$, $\rho = 2700\,\mathrm{kg\,m^{-3}}$, $\nu = 0.33$) in which the links have a slenderness ratio of $t/L = 1/15$ and a unit depth (throughout this work, we deal with plane-stress conditions, i.e. we model thin cellular structures); the FE model we use comprises 10 beam elements per link. Moreover, we define the non-dimensional frequency $\Omega = \omega/\omega_0$, where $\omega_0$ is the first natural frequency of a pinned-pinned beam having the same characteristics of a lattice link, whose expression is:

$$\omega_0 = \frac{\pi^2}{L^2}\sqrt{\frac{E\,I}{\rho\,A}} \quad , \tag{2.26}$$

where $L$ is the link length, $A$ is its cross-section and $I$ is the second moment of area of the cross-section, while $E$ and $\rho$ are Young's modulus and density of the material, respectively.

Theoretically, each surface should correspond to a mode of wave propagation. However, for some specific wave vector values and for some modes only, surfaces approach each other but veer away without intersecting (see detail in Fig. 2.3). This behavior is called *veering* [108] and it causes physical wave propagation modes to extend over multiple dispersion surfaces [39].

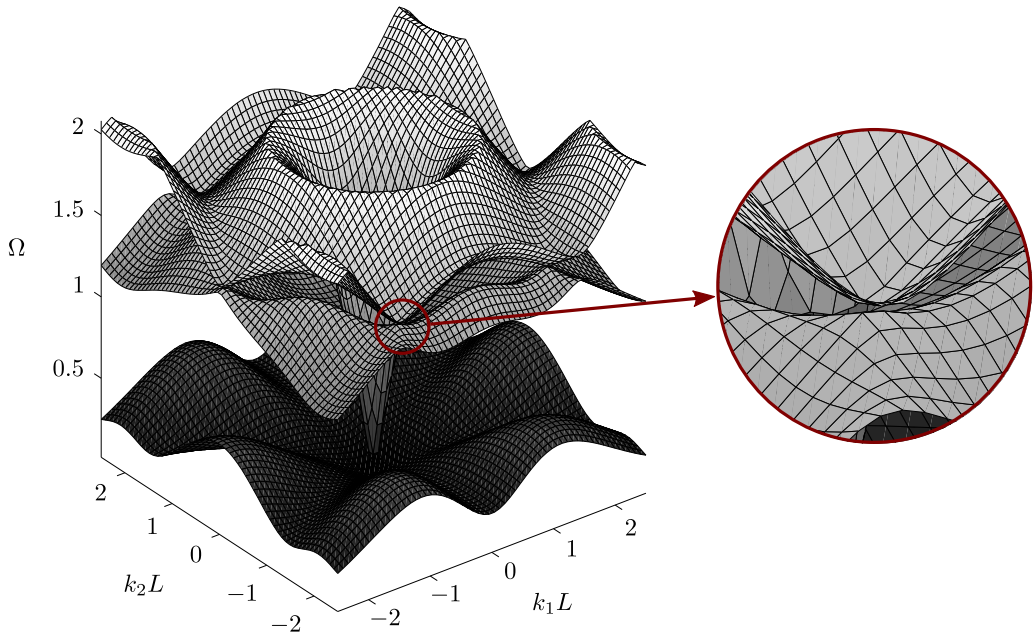


Figure 2.3: Non-dimensional, Cartesian dispersion relation (comprising the first three surfaces only) for a RH lattice, and detail of one the veering regions between second and third surfaces.

### 2.5.1 Spectral wave analysis: Brillouin zones and the band diagram

Due to the periodicity of the selected architecture, the dispersion relation $\omega(\xi_1, \xi_2)$ is periodic in the wave vector space. For this reason, to access all the information on the wave propagation behavior of a certain periodic structure, it is sufficient to consider the region of the reciprocal wave vector space delimited by the (First) *Brillouin zone* (BZ) [1], which is a Voronoi tessellation of the reciprocal lattice. The BZ of a RH lattice is shown as a dashed contour in Fig. 2.4. Note that, in this representation, we rectified the $\xi_1$ and $\xi_2$ axes. Due to the inevitable symmetries of the dispersion relation (e.g. time reversal symmetry imposes an identical wave response for opposite wave vectors), all the relevant information on wave propagation is contained in a subregion of the BZ called *irreducible* Brillouin zone (IBZ). Note that, in the way we intend it, the IBZ reflects the symmetry landscape of the response and not that of the cell. In Fig. 2.4, the IBZ of the RH lattice is represented by the shaded OAB region.

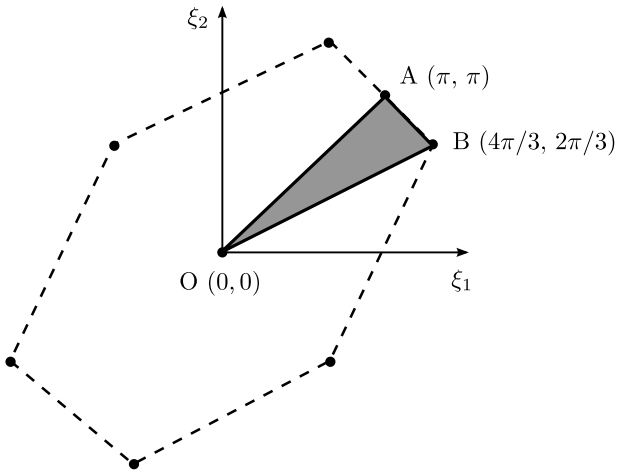


Figure 2.4: First Brillouin zone (BZ) of a RH lattice. The shaded area is the irreducible Brillouin zone (IBZ).

A compact representation of the spectral wave characteristics of a periodic medium, called *band diagram*, is obtained by solving Eq. 2.25 along the $(\xi_1, \xi_2)$ pairs belonging to the IBZ contour, which encompasses all the maxima and minima of each dispersion surface. The band diagram of the RH lattice is shown in Fig. 2.5. This representation allows

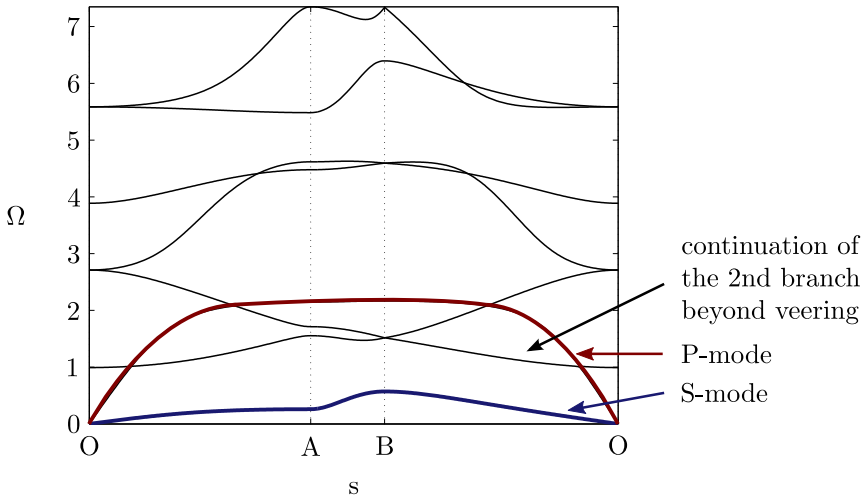


Figure 2.5: Band diagram of a RH lattice. The s coordinate spans the contour of the IBZ in Fig. 2.4. A bandgap can be seen in the neighborhood of $\Omega = 5$.

to conveniently assess which dispersion surfaces, here called *branches*, exist at a certain

frequency. For example, we can see that the low frequency region is dominated by two modes: a slow, short wavelength mode, corresponding to the first branch (S-mode, blue curve), and a fast, long-wavelength mode, which spans multiple branches and experiences veering around $\Omega = 1$ (P-mode, maroon curve). In making our considerations, we took into account that the slope of the branches is indicative of the velocity of energy propagation. Band diagrams also allow to determine where the bandgaps—frequency ranges of forbidden wave propagation—are located. For example, the lowest-frequency bandgap of the RH lattice is highlighted in Fig. 2.5 by the absence of branches in the neighborhood of $\Omega = 5$.

### 2.5.2 Spatial wave analysis: iso-frequency, phase and group velocity contours

Despite their advantages, band diagrams do not represent a convenient tool to understand spatial wave features. In this sense, the iso-frequency contours of the dispersion surfaces are an excellent source of information. The contours of the first two surfaces of the RH lattice in the reciprocal wave vector plane are shown in Fig. 2.6a and Fig. 2.6b. These surfaces highlight how the response of the structure is periodic in the wave vector plane, with the BZ being a sort of repetitive volume element. Clearer information on the spatial wave propagation features can be evinced from the iso-frequency contours in the Cartesian wave vector plane, shown in Fig. 2.6c and Fig. 2.6d. For example, we can see that both first and second surfaces display a transition from isotropic to anisotropic wave propagation; this represents a signature of the *wave anisotropy* inherent to a RH lattice. We can also visualize how the response is characterized by the same 6-folded symmetry of the unit cell. However, note that Fig. 2.6c is representative of a single mode (S-mode), while Fig. 2.6d is not. The sudden transition from isotropic to anisotropic contours showcased by the second branch is a byproduct of veering: the second mode (P-mode) is in fact known to display isotropic propagation features throughout its whole frequency range.

While representing a valuable tool to assess the presence of anisotropic wave patterns, the iso-frequency contours do not provide direct information on the principal directions of wave propagation. For this reason, we introduce the (iso-frequency) velocity contours. Two velocity measures are typically considered when analyzing wave

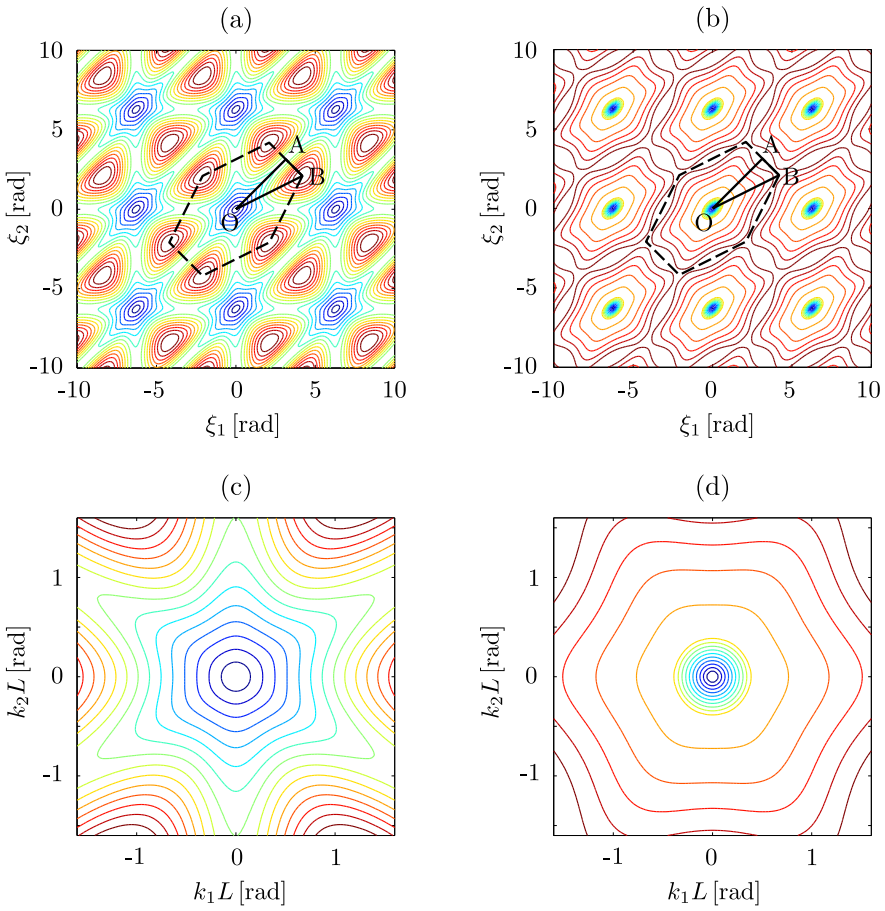


Figure 2.6: Iso-frequency contours of a RH lattice. (a), (b) Contours of first and second dispersion surfaces, respectively, in the reciprocal wave vector plane. (c), (d) Contours of first and second dispersion surfaces, respectively, in the Cartesian wave vector plane.

propagation events. The *phase velocity* is the speed of single peaks of a wave packet; in two-dimensions, it is given by

$$\mathbf{c}^p = \frac{\omega}{k^2}\mathbf{k} \quad , \tag{2.27}$$

The *group velocity* is the speed of the centroid of a propagating wave packet. It is defined as

$$\mathbf{c}^g = \nabla\omega(k_1, k_2) = \left(\frac{\partial\omega}{\partial k_1}, \frac{\partial\omega}{\partial k_2}\right)^T \quad , \tag{2.28}$$

and it is known to highlight the main avenues of energy propagation within a structure [98]. The phase and group velocity contours of the first dispersion surface (S-mode)

of the RH lattice are shown in Fig. 2.7a and Fig. 2.7b, respectively. We can see that,

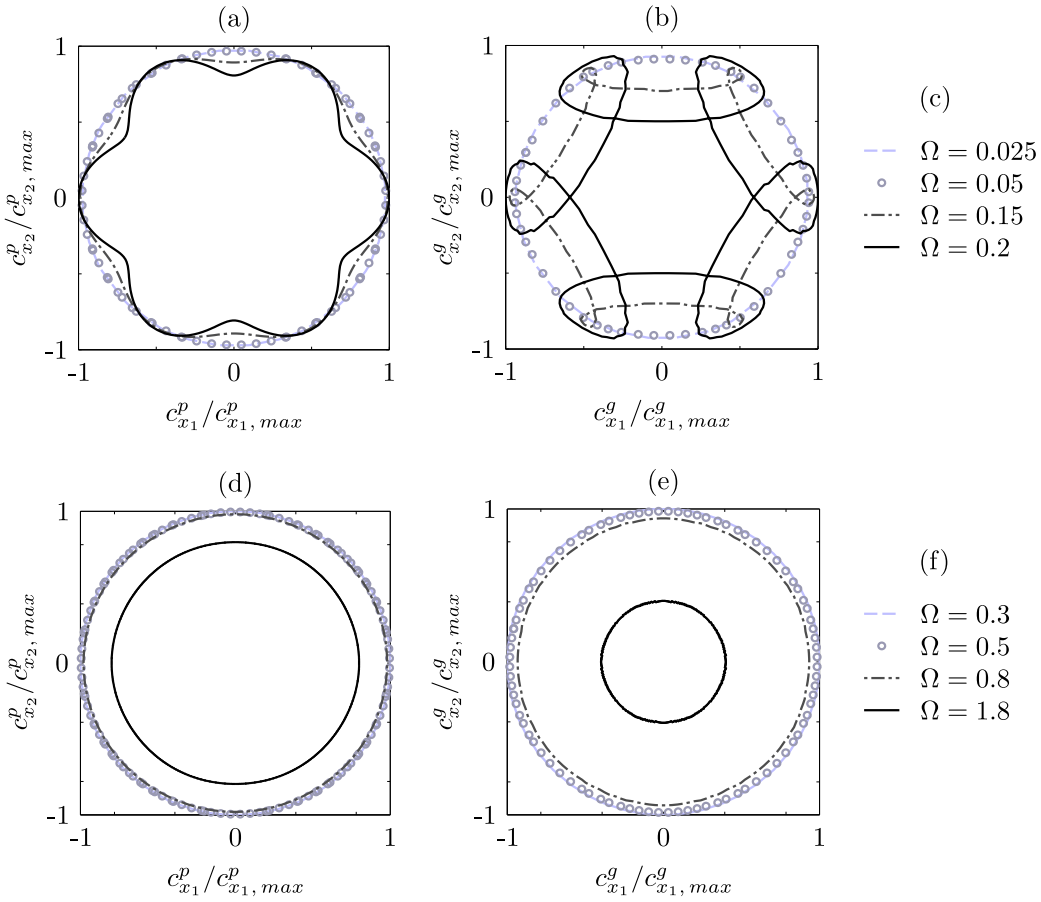


Figure 2.7: Nondimensional velocity contours of a RH lattice. (a), (b) Phase and group velocity contours of the S-mode. (c) Frequency legend for (a), (b). (d), (e) Phase and group velocity contours of the P-mode. (f) Frequency legend for (d), (e).

when the behavior is still non-dispersive (at low frequencies), both peaks and packets propagate isotropically throughout the lattice, as evidenced by the circular velocity contours. As frequency increases, the S-mode becomes anisotropic; phase velocity contours show *lobes* corresponding to the main directions of wavefronts propagation, while group velocity plots present *caustics* corresponding to preferential avenues of energy propagation. Note how these anisotropic propagation patterns are "stellar", i.e. they display multiple equipotent wave propagation avenues. The phase and group velocity contours of the P-mode (across the first three branches) of the same lattice are shown in Fig. 2.7d

and Fig. 2.7e, respectively. They highlight how this mode retains isotropic features over a broad frequency region, while eventually showing signatures of dispersive behavior (contours become smaller in radius) as the frequency increases.

# Chapter 3

# Tailoring wave anisotropy

## 3.1 The ideal wave manipulation strategy

In this Chapter, we discuss the theoretical foundations of two wave control strategies whose objective is to attain desired tailoring of the wave anisotropy characteristics of cellular solids. An overview of the most popular spatial manipulation strategies introduced to date was given in Sec. 1.2.2, together with their advantages and limitations. In an attempt to overcome some of these limitations, we begin by listing a number of desirable attributes that an ideal strategy should possess:

1. *Low-frequency.* Most mechanical excitations of practical interest are low-frequency in nature. A spatial manipulation strategy of practical interest should target those low frequencies without requiring periodic structures of very large dimensions.

2. *Single-direction wave focusing.* We would like the energy of a propagating wave packet to be channeled along a single direction of the medium. In other words, we would like to replace the highly-symmetric "stellar" patterns of default dispersion surfaces with a directionally-biased field featuring a single wave beaming direction.

3. *Tunable.* Tunability of the wave characteristics of periodic media is a very active area of research, as highlighted in Sec. 1.3. The optimal spatial manipulation strategy should, therefore, be tunable or compatible with existing tunability strategies (e.g. those involving smart materials).

4. *Non-invasive*. To retain its ability to be integrated in larger structural systems and its applicability to structural vibration problems, the spatial wave manipulation strategy should not undermine the static properties or the load bearing capabilities of the periodic medium.

While tunability is one of the requirements we impose for our spatial wave manipulation strategies, in this Chapter we limit ourselves to describing our proposed methods in their "passive" form, without introducing any element of tunability. The integration of tunable characteristics will be discussed in the following Chapters.

## 3.2 Wave beaming via cell symmetry relaxation

In this Section, based on the requirements discussed above, we introduce a low-frequency strategy for spatial wave manipulation which allows to achieve single-direction wave beaming, while remaining non-invasive and potentially allowing for the incorporation of active material phases to attain tunability (as discussed in the following Chapters). This approach relies on the enhancement of the inherent wave anisotropy of lattice structures through a *symmetry-driven microstructural design* of the unit cell.

### 3.2.1 Lattice structures with relaxed cell symmetry

The analysis of the regular hexagonal lattice in Section 2 highlighted how cellular structures feature low frequency, anisotropic wave propagation patterns. At the same time, we also mentioned that these patterns are generally stellar—they present multiple equipotent wave focusing directions. For example, in a regular hexagonal lattice, the phase and group velocity contours (Figs. 2.7a-b) display six principal directions of wave propagation. The 6-folded symmetry of these contours hints at the existence of a direct relationship between the symmetry landscape of the unit cell geometry and that of the response. To attain highly anisotropic responses characterized by low degrees of symmetry, we initially consider regular unit cells, e.g. the hexagonal one shown in Fig. 3.1a, and we populate the voids with a symmetric population of *auxiliary microstructural elements*, as shown in Fig. 3.1b. Here, the microstructural elements are cantilever beams located at the nodes of the hexagons; they are "auxiliary" since they only marginally interfere with the main/principal lattice structure (they only cause a mass increase at

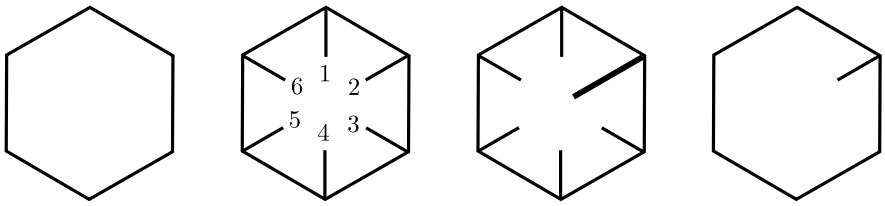


Figure 3.1: Relaxing the symmetry of a RH unit cell. (a) RH unit cell. (b) RH unit cell with a symmetric population of microstructural elements (cantilevers). Note that the cantilever numbering introduced here is used throughout this work. (c), (d) hexagonal unit cells with relaxed cell symmetry (RCS), featuring non-symmetric populations of cantilevers.

the nodal locations while exerting a minimal influence on its static response). This specific architecture, introduced by Gonella et al. [101] in the realm of phononic structures for energy harvesting, was later reprised by Hladky-Hennion et al. [109] for its "penta-mode" nature, which endows it with negative refraction capabilities. The key idea in our work is that the symmetry of the lattice response can be altered by "relaxing" the symmetry of the unit cell through modifications to the population of microstructural elements. Examples of cell configurations with *relaxed cell symmetry* (RCS) are those shown in Figs. 3.1c-d, obtained from the one in Figs. 3.1b by increasing the length and width of a single cantilever or by removing all cantilevers but one, respectively.

### 3.2.2 Theoretical implications of symmetry relaxation

The implications of symmetry relaxations of the unit cell on the lattice response are hereby investigated leveraging Bloch's theorem and the visualization tools introduced in Chapter 2. As a benchmark problem, we compare the unit cell of the RH lattice, shown in Fig. 3.1a, to the RCS unit cell featuring cantilever 2 only (the cantilever numbering is shown in Fig. 3.1b), shown in Fig. 3.1d. In both cases, the material properties we select are those of Aluminum ($E = 71\,\mathrm{GPa}$, $\rho = 2700\,\mathrm{kg\,m^{-3}}$, $\nu = 0.33$) and the slenderness ratio of the main lattice beams is $t/L = 1/15$. We define $L_c$ as the cantilever length and $t_c$ as the cantilever thickness. For convenience, we also introduce the non-dimensional ratios $\alpha = L_c/L$ and $\beta = t_c/t$. Note that, as in Chapter 2, we resort to a Timoshenko beam model for the finite element analysis. This choice provides

flexibility when modeling the behavior of large lattice structures—a task that would prove challenging from a computational standpoint if we were to use a 2D elasticity model. However, due to the particular geometry of the unit cell and due to the large thickness values we resort to in our analysis, it is legitimate to doubt the validity of beam models, especially at those "bulky" junctions where several beams converge. This aspect is addressed in Appendix A. It turns out that both beam and 2D elasticity models predict the same wave propagation features. However, the dispersion relations obtained in the two cases are shifted in frequency, with lattice struts and cantilevers appearing to be stiffer in the 2D model. For convenience, we keep this aspect in mind and carry out a beam-based FE analysis.

The unit cell analysis results for a RCS architecture with $\alpha = 1.2$ and $\beta = 1$ are shown in Figs. 3.2-3.3, and compared to the RH lattice response in Fig. 3.3. The

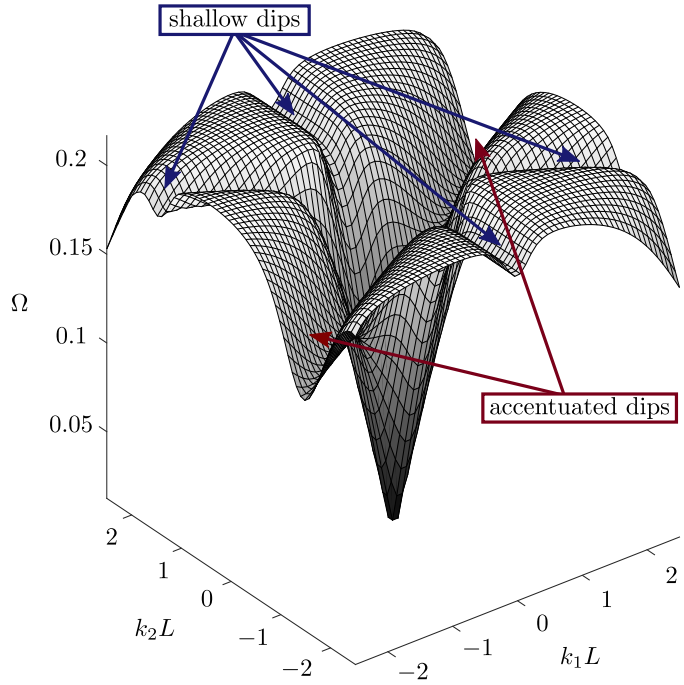


Figure 3.2: Non-dimensional, Cartesian dispersion relation (comprising only the first dispersion surface) of a RCS architecture.

symmetry relaxation of the cell geometry translates into a modification of the symmetry landscape of the phase constant surfaces and, consequently, of the structure's response.

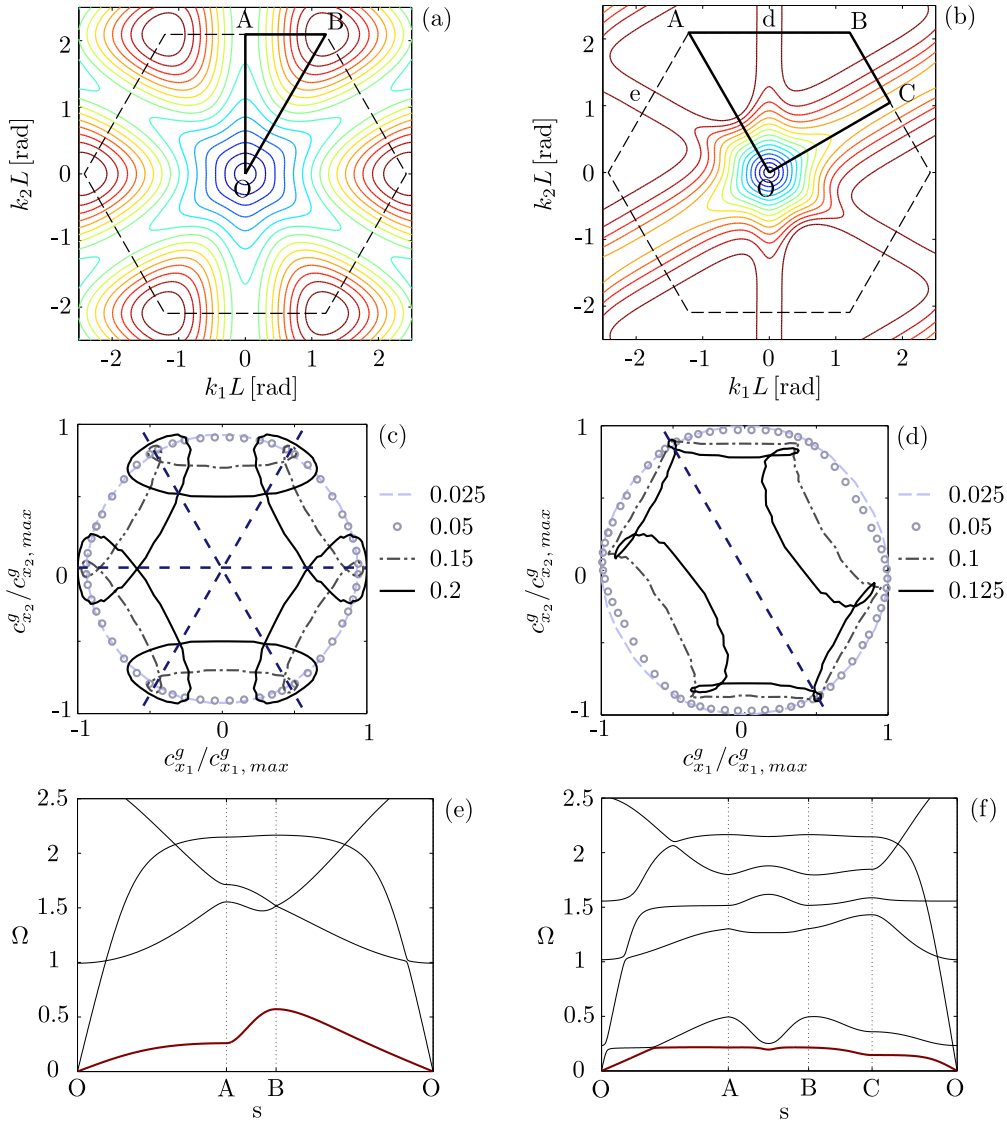


Figure 3.3: (a), (b) Iso-frequency contours of the 1st dispersion surface of RH and RCS ($\alpha = 1.2$, $\beta = 1$) architectures, respectively. Dashed contours represent BZs and continuous ones represent IBZs. (c), (d) Group velocity contours of the 1st dispersion surface of RH and RCS topologies, respectively. (e), (f) Low-frequency region of the band diagrams of RH and RCS architectures, respectively. The branches analyzed in (a), (b), (c), (d) are highlighted in red.

This can be evinced by noticing that the symmetry landscape of the first dispersion surface, shown in Fig. 3.2, loses its six-folded nature. This modification can be better

appreciated by comparing the iso-frequency contours of the first phase constant surface of the reference RH case (Fig. 3.3a) and of the RCS lattice of interest (Fig. 3.3b). The implications of symmetry relaxation on the wave response are further highlighted by the angular dependence of the group velocity vector. The group velocity contours derived from the first phase constant surface for the RH lattice and for the lattice with RCS are reported in Fig. 3.3c and Fig. 3.3d, respectively. The RH case, as expected, features a symmetric stellar response, that highlights how the energy is equally distributed among six directions (three axes). Upon cell symmetry relaxation, focusing is observed along one single axis, which connects the two major caustics and corresponds to the OA direction. Note that, in Fig. 3.3c-d, the main propagation axes are highlighted with dashed blue lines. Lastly, the symmetry relaxation at the unit cell level also affects the construction and morphology of the band diagram (see Figs. 3.3e-f). The First Brillouin zone (BZ) remains unchanged in going from the RH to the RCS case, since the direct and reciprocal lattice vectors are not affected by the presence of the microstructure. On the other hand, the Irreducible Brillouin zone (IBZ), which reflects symmetries in the spatial wave response, needs to be significantly modified—from the conventional triangle OAB to the polygon OABC. As expected, the introduction of an auxiliary microstructure is responsible for a higher modal density in the low-frequency region, as visible by comparing the band diagrams.

Further considerations on the relationship between symmetry of the cell geometry and symmetry of the response can be made by tabulating the symmetry landscapes of the responses of all the architectures that can be obtained, via cantilever subtraction, from the cell in Fig. 3.1b. This table, shown in Fig. 3.4, is drafted for configurations with $\alpha = 0.8$ and $\beta = 3$; however, the same symmetry considerations apply to any other choices of parameters. Similarly, even though we only report the iso-frequency contours of the first mode, similar considerations could apply to other modes. To classify symmetries in a rigorous way, we introduce the following *point symmetry operations* [110]:

- Rotation: a cell configuration/wave response possesses $n$-fold rotational symmetry if it remains unchanged after a $2\pi/n$ rotation about one axis.

- Reflection: a cell configuration/wave response possesses reflection symmetry with respect to a plane (an axis in our 2D case) if it remains unchanged after undergoing

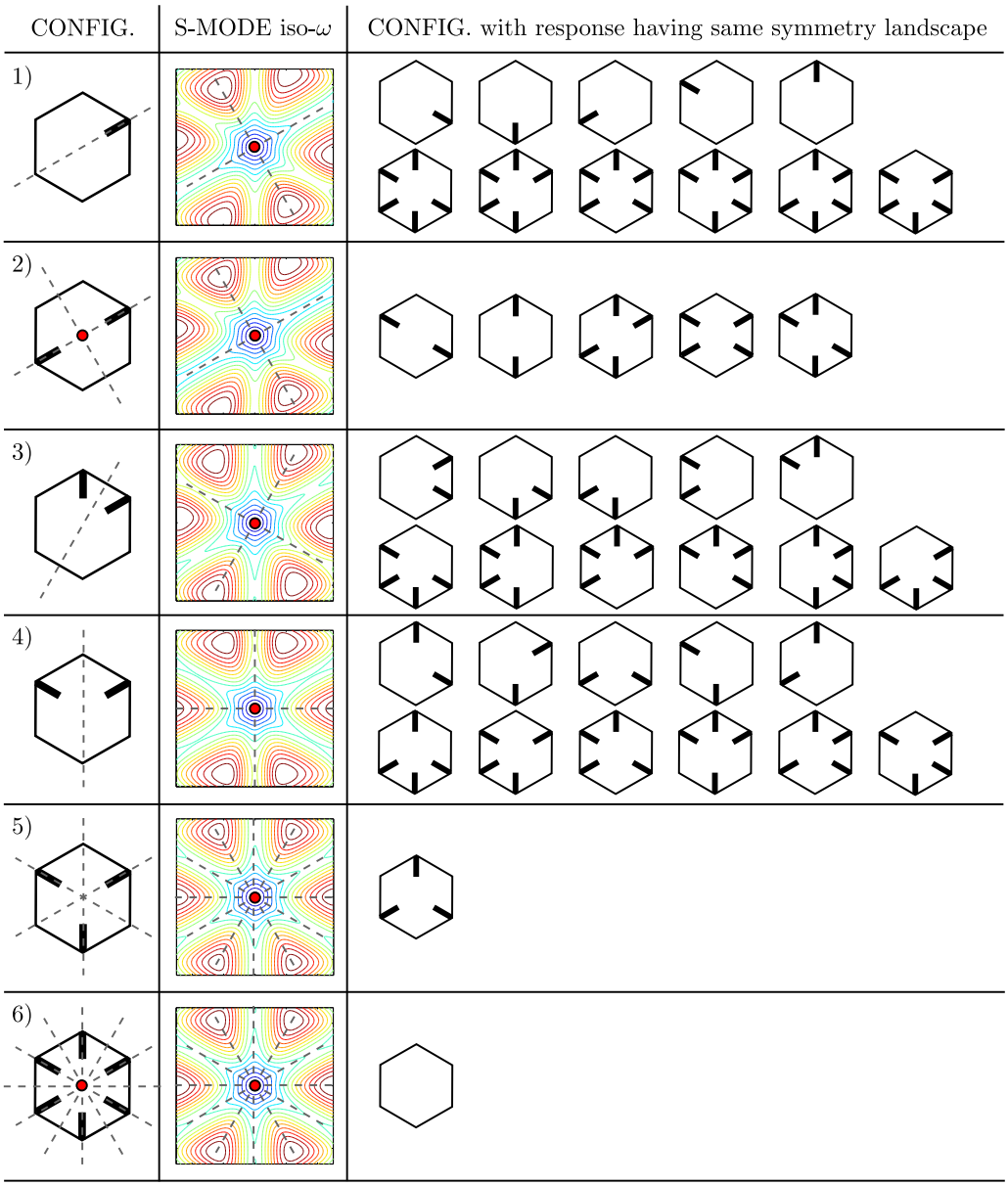


Figure 3.4: Relaxed cell symmetry scenarios for a RH lattice with cantilevers ($\alpha = 0.8$ and $\beta = 3$). The dashed lines indicate reflection planes; the circular red markers indicate the center of symmetry of those unit cells/wave responses featuring inversion symmetry.

mirroring with respect to that plane.

- Inversion: a cell configuration/wave response possesses inversion symmetry if each

point can be inverted with respect to a *center of symmetry*.

The considered cell configurations are divided into six groups, according to the numbering shown in Fig. 3.4. Configurations with a complementary number of cantilevers, e.g. those presenting only one or five cantilevers, display responses characterized by the same symmetry landscape, and are therefore grouped together. We now proceed with a group-by-group analysis. In group 1 the cell configuration features reflection symmetry about a single axis (the dashed line in the figure), while the response has two symmetry axes: one that coincides with that of the cell configuration and one perpendicular to it. We can also see that the response displays 2-fold and inversion symmetries, while the cell configuration does not. In group 2, cell configuration and response display the same symmetry features: they are characterized by the same two reflection axes, 2-fold and inversion symmetries (the center of symmetry is highlighted with a red circular marker). In groups 3 and 4 the cell configurations feature reflection symmetry about a single axis, no rotation and no inversion symmetries. The responses, on the other hand, display 2-fold symmetry, inversion symmetry and reflection symmetry with respect to two axes (the symmetry axis of the cell configuration and one perpendicular to it). In group 5, the cell configuration has 3-fold symmetry, reflection symmetry about three axes and no inversion symmetry. The response displays 6-fold symmetry, reflection symmetry about six axes (the symmetry axes of the unit cell and the lines perpendicular to them) and inversion symmetry. Finally, both cell configuration and response in group 6 feature 6-fold and inversion symmetries, and six reflection axes. From these observations, we can conclude that all the responses display inversion symmetry, regardless of the symmetry landscape of the respective cell configurations. Additionally, we can cluster the architectures in two big groups, based on their inversion symmetry. Those which display inversion symmetry present the same symmetry landscape of their responses; this is the case for groups 2 and 6 in Fig. 3.4. Those that do not display inversion symmetry (groups 1, 3, 4, 5) and are characterized by $n$-fold symmetry and by $m$ reflection axes feature responses with inversion and $2n$-fold symmetries, and present $2m$ reflection axes.

To understand why cell configurations with different symmetry portraits give way to responses that are identical in terms of symmetries, we need to keep in mind that responses are byproducts of wave mechanics considerations. According to the D'Alembert

solution of the wave equation, we cannot excite a wave with wave vector content $\bar{\mathbf{k}}$ without also exciting a wave along $-\bar{\mathbf{k}}$. This feature is also known as time reversal symmetry. For this reason, a cantilever is activated in the same manner by waves with wave vector content $\bar{\mathbf{k}}$ and $-\bar{\mathbf{k}}$; thus, the response of periodic structures (and all solids which do not feature time-varying properties [111]) is always characterized by inversion symmetry. It should also be pointed out that, despite producing responses with identical symmetry landscapes, cell configurations in group 2 display more dramatic wave focusing effects than those in group 1; this is due to the availability of a larger number of microstructural elements. Note that all these considerations are only valid if the auxiliary cantilevers are symmetric with respect to their neutral axes.

### 3.2.3 S-mode focusing

The theoretical predictions discussed in Section 3.2.2 are validated via FE-based transient simulations (using a Newmark-$\beta$ integration scheme) on a lattice of $54 \times 36$ cells along the horizontal and vertical directions, respectively. Figure 3.5 shows the response to a narrow-band burst excitation (with carrier frequency $\Omega = 0.125$) of a RH lattice (Fig. 3.5a-b), and of two RCS lattices featuring cantilever 2 only, but with different tuning parameters ($\alpha = 1.2$ and $\beta = 1$ in Fig. 3.5c-d, $\alpha = 1.2$ and $\beta = 3$ in Fig. 3.5e-f). Note that the excitation is applied at the midpoint of the upper edge of the lattice and directed along the Od direction. At this frequency, the P-mode is engaged in a steep region of the corresponding dispersion surface; this corresponds to a fast, long-wavelength packet which, in the time frame of our acquisition, quickly morphs into a low-amplitude standing mode. Therefore the observed wavefields correspond essentially to a pure S-mode. While in the RH case the energy is evenly partitioned between the left and right quadrants of the domain (Fig. 3.5a-b), the responses of the RCS architectures are characterized by a significant de-energization of the left quadrant (Fig. 3.5c-d and 3.5e-f), with the faster fronts advancing along the OA focusing direction, in agreement with the group velocity contours of Fig. 3.3d. Fig. 3.5 also suggests that $\beta$ plays an important role in the partition of the energy, which we adopt as a measure of wave manipulation. To investigate this dependence, we consider two benchmark cases: a flexible microstructure of slender cantilevers ($\beta = 1$) and a stiff microstructure of bulky cantilevers ($\beta = 3$); we find that the mechanisms of symmetry relaxation are profoundly

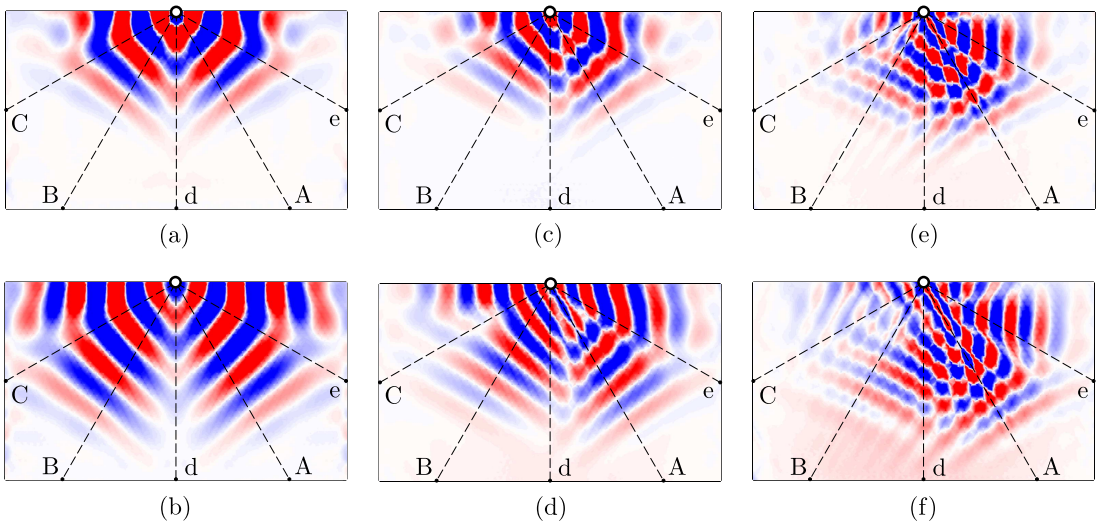


Figure 3.5: Effects of relaxed cell symmetry on the response of finite lattices ($54 \times 36$ unit cells). All wavefields are snapshots of $u_y$ obtained from numerical simulations at $\Omega = 0.125$, corresponding to the S-mode. (a-b), (c-d), (e-f) Wavefields at two time instants for the RH lattice, for the RCS lattice with parameters $\alpha = 1.2$ $\beta = 1$, and for the RCS lattice with parameters $\alpha = 1.2$ $\beta = 3$, respectively. The dashed lines represent directions of interest named after the corresponding BZ key points (refer to Fig. 3.3b). The white markers indicate the excitation point.

different in those two cases.

For $\beta = 1$, the left quadrant is mildly de-energized. To provide a mechanistic rationale for this effect, we investigate how the microstructure is engaged by an incident shear wave along different radial directions in the lattice. In particular, we monitor the OC direction (representative of slow propagation) and the OA direction (representative of fast propagation). When a shear wave with $\mathbf{k} \,/\!/\, \mathrm{OC}$ impinges on a cell (Fig. 3.6), its microstructural element (also aligned along OC) is immediately engaged and undergoes pure flexural motion. This results in significant lateral deflection of the cantilever and energy storage at its root. On the other hand, for $\mathbf{k} \,/\!/\, \mathrm{OA}$, the microstructure is engaged by the impinging shear wave after some delay and undergoes a blend of low-amplitude modes; group delay accumulates as the disturbance travels along the waveguiding path of the cell contour and mode conversion occurs at each cell node. To validate this conjecture, we study the angular evolution of the mode shapes along the iso-frequency contour of the S-mode dispersion surface at $\Omega = 0.125$, with emphasis on the directions

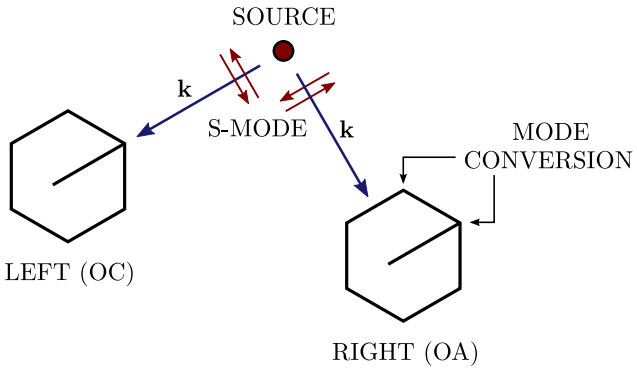


Figure 3.6: Schematic of the mechanistic conjecture for the symmetry relaxation of the response in RCS lattices ($\beta = 1$, S-mode).

of the wave vector highlighted by letters A, B, C, d and e in Fig. 3.3b, which are relevant to our discussion on focusing. The mode shapes are reported in Fig. 3.7. As expected,

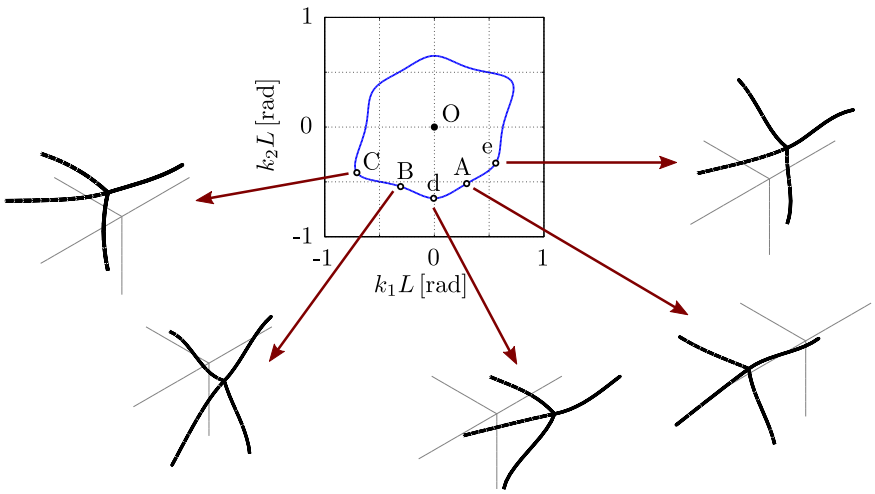


Figure 3.7: Mechanistic explanation of S-mode focusing for the RCS lattice with $\beta = 1$: deformed shapes for the S-mode, at frequency $\Omega = 0.125$, along selected directions relevant to our discussion.

when the wave vector is directed along OC, the corresponding mode shape features a markedly bent microstructural element. A similar behavior (with some fluctuation in intensity) is observed for wave vectors comprised in the angular neighborhood of OC (confined to the left quadrant and including direction OB). In contrast, the cantilevers

engaged by shear waves propagating along OA (and, to some extent, neighboring directions) feature negligible bending deformation. This dichotomy between left- and right-quadrant dynamics is in agreement with Fig. 3.6 and suggests that, even within a perfectly periodic medium, a wave emanating from a point source would interact differently with an angularly non-uniform set of effective microstructural properties. To further confirm this interpretation, we analyze the evolving energy landscape of a finite RCS lattice with $\beta = 1$ subjected to the same burst excitation. We consider a snapshot of the wavefield at a certain time instant and we focus our attention on five regions identified along a common (anisotropic) wavefront corresponding to the same directions discussed for the mode shapes (see Fig. 3.8). The color in the magnified windows cor-

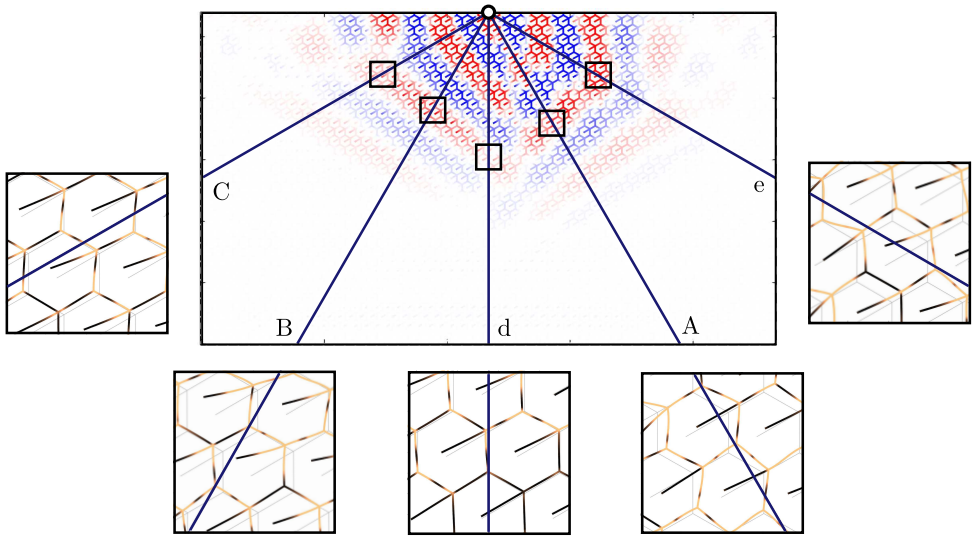


Figure 3.8: Mechanistic explanation of S-mode focusing for the RCS lattice with $\beta = 1$: mechanisms of energy partition in different regions along a propagating front; lighter color in the boxes corresponds to larger values of potential energy. Note that, in the boxes, the potential energy is plotted on the deformed lattice.

responds to the instantaneous potential energy (high potential energy, light color and vice versa), calculated for each element as

$$\mathbf{V}_e(t) = \frac{1}{2}\mathbf{u}_e^T(t)\,\mathbf{K}_e\,\mathbf{u}_e(t) \quad , \tag{3.1}$$

where $\mathbf{u}_e$ is the vector of elemental displacements and $\mathbf{K}_e$ is the element stiffness matrix. As expected, the microstructural elements along the OC direction seem to store

more potential energy (relative to that stored by the surrounding portion of the primary lattice) with respect to the other directions. While the cantilevers along OB and Oe also exhibit significant levels of potential energy, this is mostly due to the fact that the surrounding lattice is, overall, highly deformed. On the other hand, the microstructure is essentially undeformed along directions OA and Od. We can therefore link the radially non-uniform energy landscape to a non-uniform availability of energy trapping mechanisms in the lattice.

In the $\beta = 3$ case, the wavefield in the left quadrant is dramatically attenuated. This behavior can be explained by comparing the band diagrams for RCS lattices with different values of $\beta$, as shown in Fig. 3.9. As expected, as $\beta$ is increased, we observe a

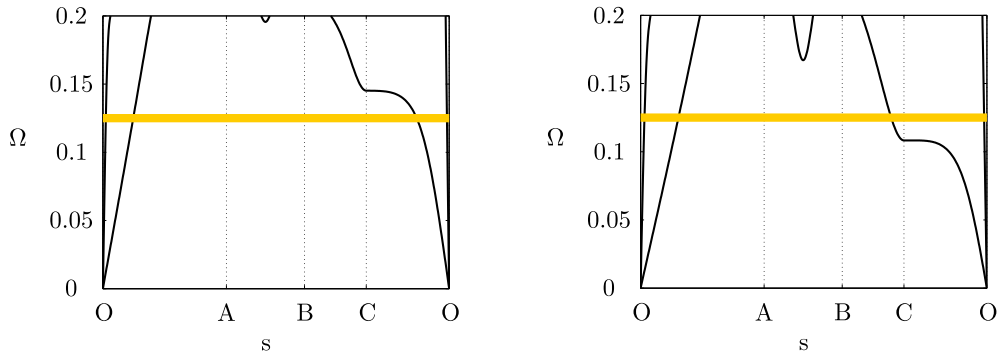


Figure 3.9: Comparison of the S-mode region of the band diagrams for RCS lattices with different values of $\beta$. (a) $\beta = 1$. (b) $\beta = 3$. The thick horizontal line highlights the $\Omega = 0.125$ excitation frequency.

progressive global lowering of the spectrum; eventually, when $\beta = 3$, a partial bandgap is generated along the OC direction, inducing strong attenuation in the wavefields along that same direction.

### 3.2.4 P-mode focusing

Let us now excite a P-mode by applying a burst excitation with carrier frequency $\Omega = 0.8$. In this analysis, we focus on a RCS lattice with $\alpha = 1.2$ and $\beta = 3$. For this specific configuration, this frequency pinpoints only the third branch of the dispersion relation; due to veering, this branch corresponds to the physical P-mode. Two successive snapshots of the resulting wavefield are shown in Fig. 3.10c-d, and compared

with equivalent stages of propagation in a RH lattice in Fig. 3.10a-b. In agreement

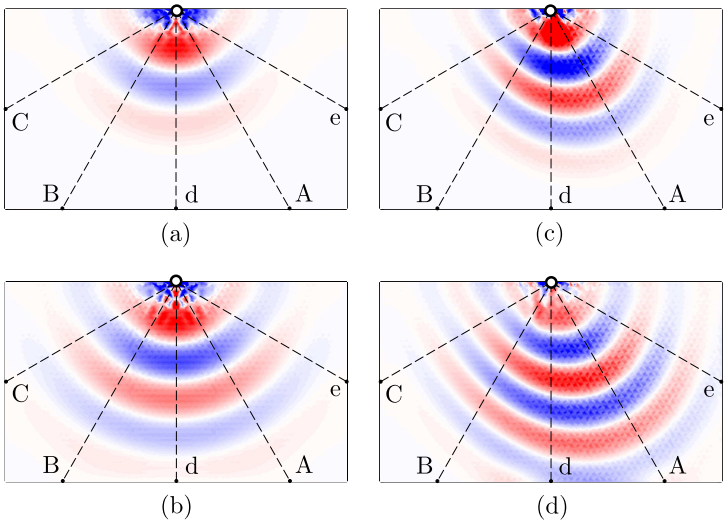


Figure 3.10: Effects of relaxed cell symmetry on the response of finite lattices ($54 \times 36$ unit cells). All wavefields are snapshots of $u_y$ obtained from numerical simulations at $\Omega = 0.8$, corresponding to the P-mode. (a-b), (c-d) Wavefields at two time instants for the RH lattice and for the RCS lattice with parameters $\alpha = 1.2$ $\beta = 3$.

with the results for the S-mode, we observe focusing along the OA direction. One can easily appreciate the substantial uneven partition of the energy between left and right quadrant.

To provide a rationale for the observed evolution of the response in the presence of longitudinal wave mechanisms, we monitor the mode shapes evaluated along the iso-frequency contour line of the third phase constant surface for $\Omega = 0.8$, reported in Fig. 3.11; we observe the opposite scenario with respect to what detected for the S-mode: the microstructure experiences some (mild) flexural dynamics along all directions except OC. This matches our expectation that longitudinal wave motion at the lattice scale, involving particle motion parallel to the wavevector, would induce purely axial (low-amplitude) wave motion in cantilevers that are themselves parallel to $\mathbf{k}$, while cantilevers that are otherwise oriented with respect to the incident front may experience some flexural dynamics upon mode conversion. Nevertheless, unlike the S-mode case, the directions along which the flexural mechanisms are activated are those where the energy is focused (the energy in the primary lattice is largest), which excludes arguments

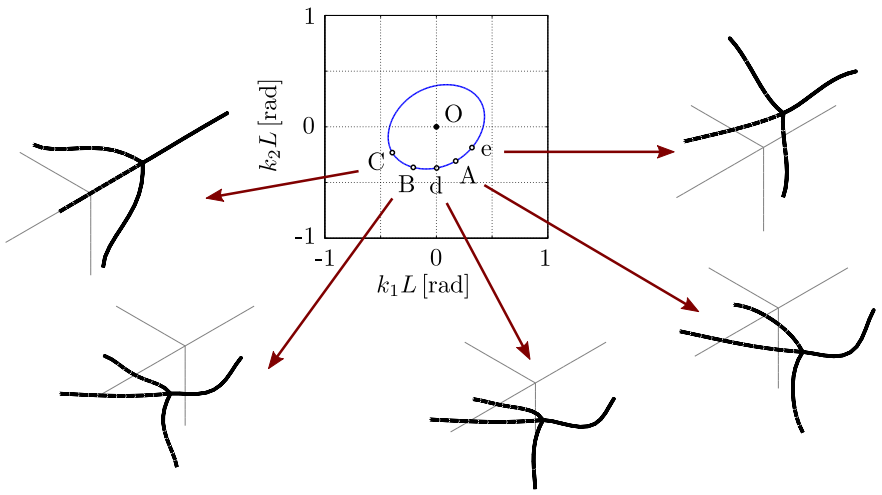


Figure 3.11: Mechanistic explanation of P-mode focusing for the RCS lattice with $\beta = 3$: deformed shapes for the P-mode, at frequency $\Omega = 0.8$, along selected directions relevant to our discussion.

based on energy trapping in the microstructure.

To relieve this apparent contradiction, we take a deeper look at the energy flow between primary and auxiliary structures. In Figs. 3.12a-b we plot the wavefield ($u_y$ displacement) at two successive stages of propagation and we monitor the evolution of the potential energy within a fixed region of the domain (corresponding to the blue box) positioned along the dominant direction of propagation OA. We note that, at the time instant corresponding to Fig. 3.12a, the region intercepts a node of the wave packet, where a sharp gradient of displacement (and consequently large strain) is established over few lattice cells; as expected, the potential energy of the primary hexagonal lattice, which is primarily associated with axial deformations of the beams, is locally high, as indicated by the bright color in the detail box. In sharp contrast, at the same time instant, the microstructure is essentially undeformed. On the other hand, in Fig. 3.12b, the highlighted region intercepts a peak of the wave packet; because of the long-wavelength nature of the P-mode at this frequency, the windowed portion of the packet features a smooth, relatively flat displacement profile. Accordingly, the potential energy stored in the primary hexagonal structure is overall significantly lower with respect to the previous time instant (note that, although visual inspection suggests that deformations are

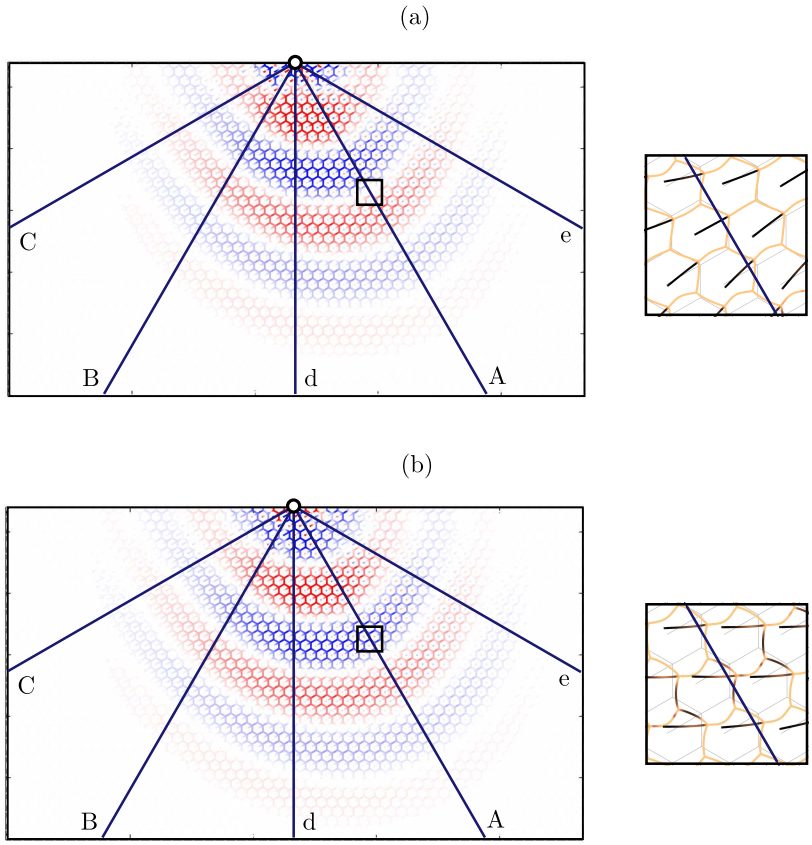


Figure 3.12: Mechanistic explanation of P-mode focusing for the RCS lattice with $\beta = 3$: analysis of the behavior of the lattice along the principal direction of propagation at two following time instants; left plots are displacement wavefields, while the color of the deformed lattice in the boxes represents potential energy (lighter color corresponds to larger energy values).

here larger than in the previous case, they mostly involve bending mechanisms, which store significantly lower levels of potential energy). In contrast, we notice that the microstructure is activated and the cantilevers store energy at their roots. In summary, a lag is observed between the local energy levels in the hexagonal lattice and those in the cantilevers: the cantilevers are maximally engaged when the surrounding lattice is de-energized and vice-versa. This suggests that a self-reinforcing mechanism is established along the main direction of propagation OA: the microstructure stores energy as the wave goes through the cell and restitutes it to the lattice at a later stage, in

correspondence to the next peak of the incoming energy packet.

## 3.3 Overriding wave anisotropy via strategically-located resonators

In this Section, we discuss an alternative strategy for spatial wave manipulation in cellular periodic structures. Rather than implementing a modification of the phononic characteristics through the introduction of non-symmetric populations of resonators internally to *each* as in the relaxed cell symmetry approach, we here leverage the interplay between the default anisotropically-propagating wave patterns of the cellular medium and the dynamics of resonators strategically placed at selected nodes of the lattice. Our starting point is the selection of a periodic cellular medium featuring anisotropic wave patterns at selected frequencies. We then consider a finite-size medium featuring the selected architecture and we introduce resonators in a subset of cells concentrated in certain subregion(s) of the lattice domain, in order to "override" only selected features of the anisotropic wave patterns. Note that this approach can be seen as the conceptual dual of the previous one, since placing resonators in some unit cells but not others results in periodicity and symmetry loss at the global—and not at the unit cell—level. The main advantage of this approach is that a large number of resonators is not required to achieve significant wave focusing results.

### 3.3.1 A square lattice of springs and masses

To illustrate the principles and potential of the *anisotropy overriding* approach, we adopt the simplest two-dimensional periodic structure—a square lattice of springs and point masses. As shown in Fig. 3.13a, the lattice is uniform—all springs have stiffness $s$, all point masses have mass $m$ and are equally spaced (the inter-mass distance along both $x_1$ and $x_2$ is $L$). Therefore, the position vector indicating a generic mass is $\mathbf{r} = n_1 L \mathbf{i}_1 + n_2 L \mathbf{i}_2$, where $n_1$ and $n_2$ are integer indices. As in previous Chapters, we compute the wave response of this periodic structure through a Bloch-based unit cell analysis. The unit cell used for our calculations is illustrated in Fig. 3.13b. Considering values of mass of $m/3$ instead of $m$ is necessary to obtain the exact configuration shown in Fig. 3.13a upon the application of Bloch's periodic boundary conditions. Each mass has a single

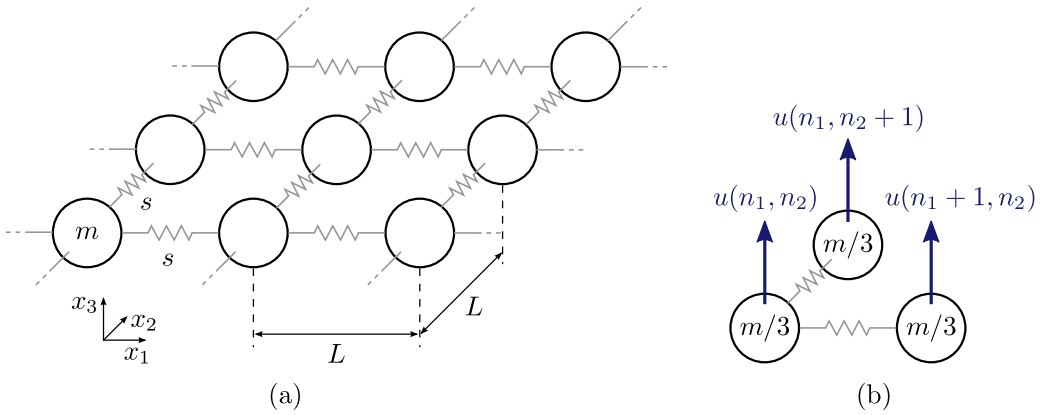


Figure 3.13: Two-dimensional square lattice of springs and masses. (a) Lattice configuration. (b) Unit cell (the arrows indicate the degrees of freedom) used for the Bloch analysis.

out-of-plane degree of freedom, i.e. it can move vertically as illustrated by the arrows in Fig. 3.13b; the displacement of the $(n_1, n_2)$ mass is labeled $u(n_1, n_2)$. Hence, the springs have to be intended as constraining the vertical motion of the masses. As a result, upon application of Bloch's conditions, characteristic equation leads to a mono-branch dispersion relation which corresponds to a single mode of wave propagation:

$$\omega = \sqrt{\frac{2s}{m}\left(2 - \cos k_1 L - \cos k_2 L\right)}\ , \tag{3.2}$$

where $\omega$ is the angular frequency, while $k_1$ and $k_2$ are the Cartesian components of the wave vector. The dispersion surface for parameters $s = m = L = 1$ is shown in Fig. 3.14a, where we used a normalization factor $\omega_0 = \sqrt{s/m}$ for $\omega$, and $L$ for $k_1$ and $k_2$. The response is more compactly represented by the band diagram in Fig. 3.14b, where $s_{\mathrm{BZ}}$ is a coordinate spanning the contour of the IBZ of the lattice. In the reciprocal lattice coordinate system, the coordinates of the corners of the IBZ are O $(0, 0)$, A $(0, \pi)$, B $(\pi, \pi)$. As the frequency increases, we record a transition from isotropic to anisotropic wave behavior. This aspect is clearly indicated by the iso-frequency contours of the dispersion surface, shown in Fig. 3.14c, and by the phase and group velocity contours in Fig. 3.14d and Fig. 3.14e, respectively. This anisotropy is correlated to the arising of partial bandgaps along the $x_1$ and $x_2$ directions (denoted by the absence of points along those directions for some of the iso-frequency contours), which cause the waves

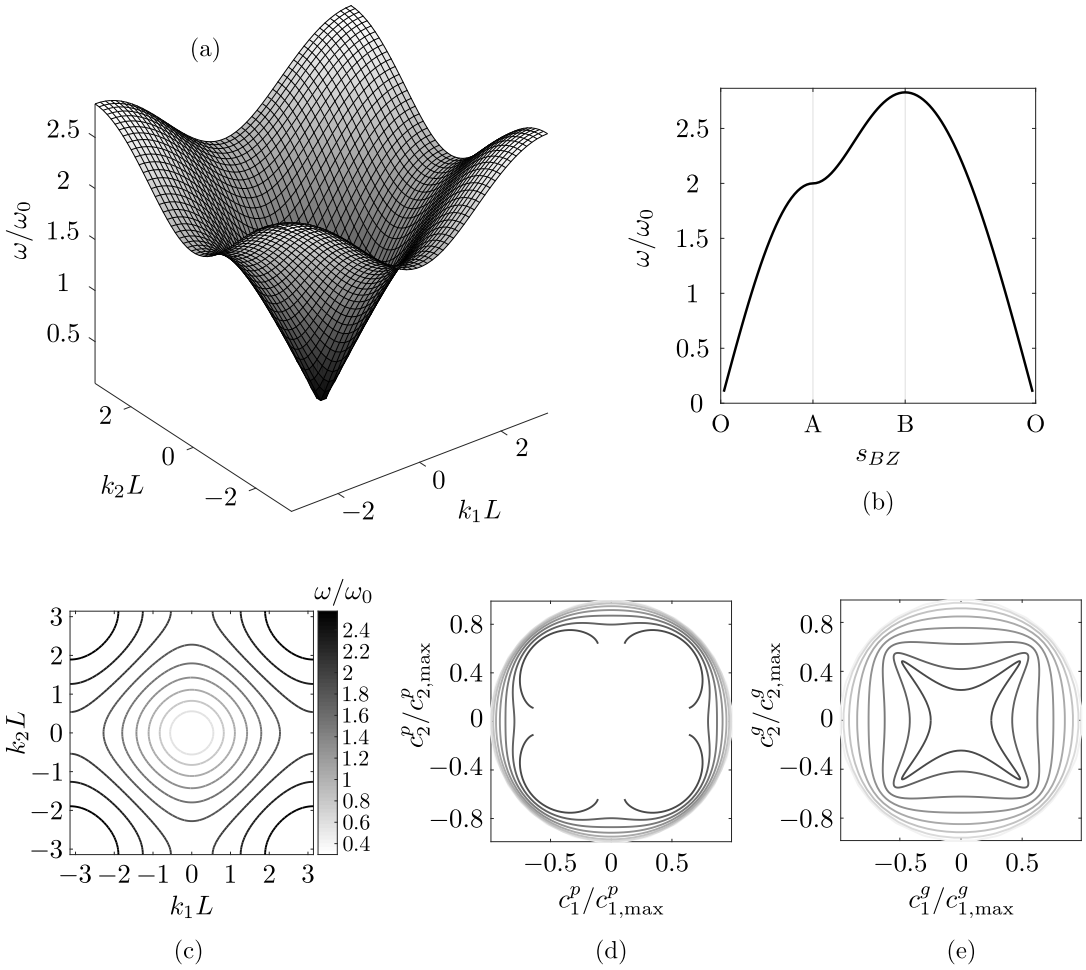


Figure 3.14: Results of the unit cell analysis for a two-dimensional lattice of springs and masses. (a) Dispersion surface. (b) Band diagram. (c) Iso-frequency contours. (d) Phase velocity contours. (e) Group velocity contours.

to predominantly propagate along $\pm 45^{\circ}$-oriented directions for frequencies greater than $\omega \approx 1.8\,\omega_0$.

### 3.3.2 A square lattice of springs, masses and resonators

To understand the influence of localized resonators on the wave response of the spring-mass lattice introduced in the previous Section, we consider a variation of the same lattice comprising an out-of-plane spring-mass resonator for each mass. This simple

model is similar in nature to the one-dimensional "mass-in-mass" one introduced by Huang et al. [10]. All resonators in the periodic lattice are characterized by stiffness $s_a$ and mass $m_a$. The lattice is sketched in Fig. 3.15a, while the unit cell with all its degrees of freedom is shown in Fig. 3.15b. To preserve the characteristics of the original

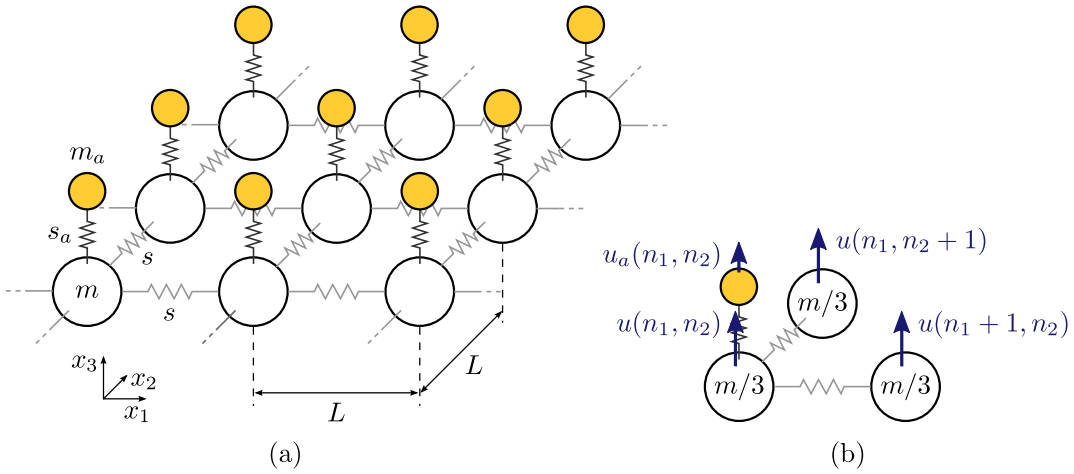


Figure 3.15: Two-dimensional square lattice of springs and masses, with auxiliary resonators (yellow masses). (a) Lattice configuration. (b) Unit cell (the arrows indicate the degrees of freedom) used for the Bloch analysis.

structure, the unit cell comprises a single resonator located at the $(n_1, n_2)$ mass. Upon the application of Bloch's conditions, the response of the infinite lattice reduces to a two degree of freedom problem. The two resulting dispersion surfaces can be computed by solving the following equation for $\omega$:

$$\begin{vmatrix} s_a + 2s\,(2 - \cos k_1 L - \cos k_2 L) - \omega^2 m & -s_a \\ -s_a & s_a - \omega^2 m_a \end{vmatrix} = 0 \ ,$$

and by selecting only the positive roots. The dispersion surface obtained with parameters $s = m = 1$, $s_a/s = 0.1$ and $m_a/m = 0.0233$ is shown in Fig. 3.16a. The band diagram in Fig. 3.16b features a thin locally-resonant bandgap, highlighted in yellow, whose onset matches the resonant frequency of the resonator $\sqrt{s_a/m_a} = 2.0717\,\omega_0$. The parameters of the resonator are chosen as to induce a locally resonant bandgap in a frequency region where the response of the lattice without resonators is strongly anisotropic (recall that, from Fig. 3.14, anisotropy is observed above $1.8\,\omega_0$). This choice

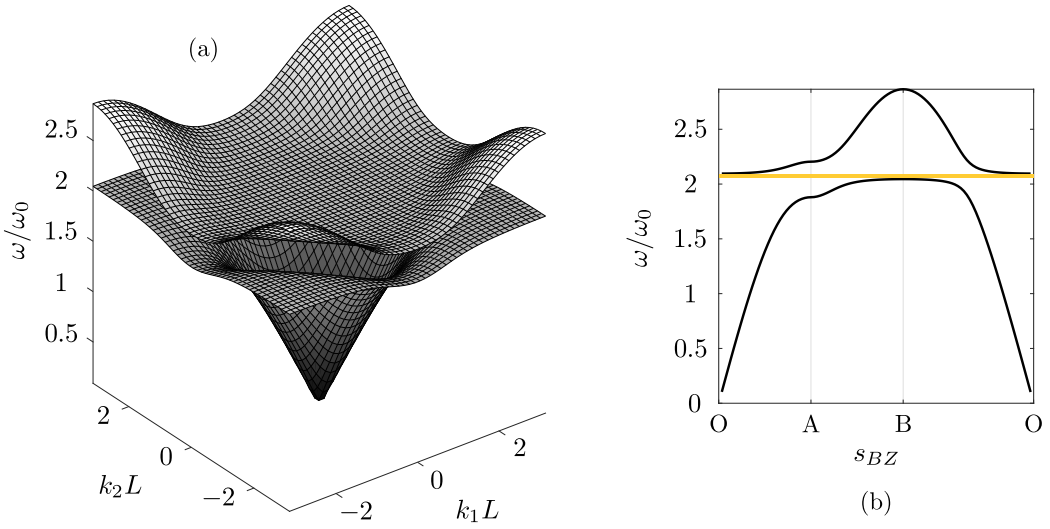


Figure 3.16: Results of the unit cell analysis for a two-dimensional lattice of springs and masses, featuring out-of-plane spring-mass resonators. (a) Dispersion surfaces. (b) Band diagram (the yellow region indicates the resonator-induced bandgap).

is motivated by the fact that we want our resonators to interact with the anisotropic wave patterns inherent to the baseline architecture without resonators.

### 3.3.3 Anisotropy overriding: partial bandgaps through strategically-located resonators

We now have all the ingredients necessary to introduce our spatial wave manipulation strategy, which is inherently applicable only to finite-sized structures. To do so, we consider an array of 45×45 masses and we place resonators on selected masses. Throughout this analysis, the excitation is always applied at the center of the lattice, i.e. at the point corresponding to $(n_1, n_2) = (0, 0)$, while the response is sensed at the four corners of the lattice, i.e. at $(n_1, n_2) = (-22, 22)$, $(n_1, n_2) = (22, -22)$, $(n_1, n_2) = (22, 22)$ and $(n_1, n_2) = (-22, 22)$. These characteristic points are color coded in the sketch of the lattice in Fig. 3.17a. In this sketch, and in the following ones in this Section, the yellow masses feature resonators while the white ones do not. Fig. 3.17b represents the steady state response of the lattice with omnipresent resonators shown in Fig. 3.17a. The response is given in terms of transmissibilities obtained by normalizing the displacement

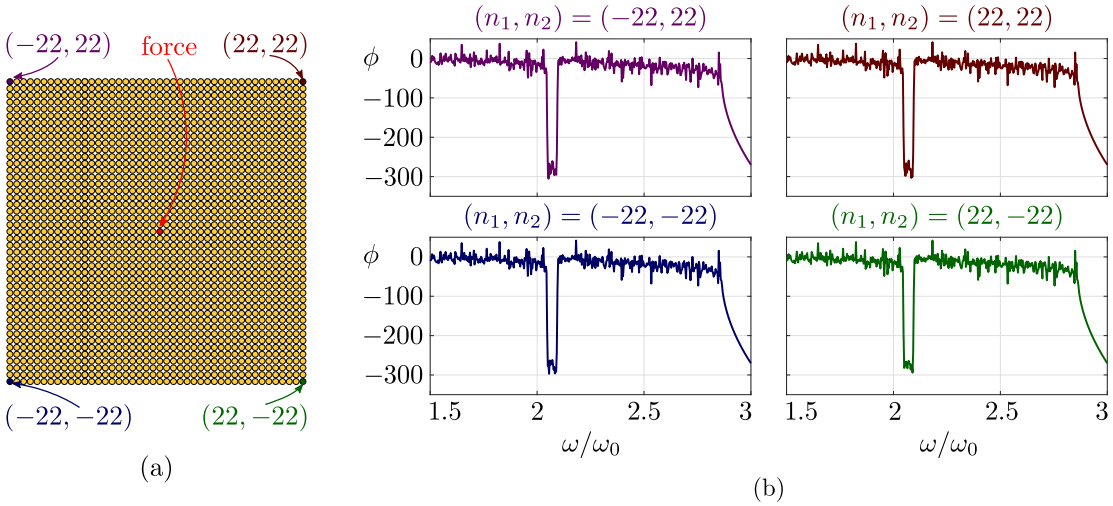


Figure 3.17: Steady state response of a lattice in which all masses are connected to resonators. (a) Illustration of the square lattice structure. In this representation, yellow masses feature resonators, while white ones do not. The red point indicates the node where the force is applied. The corner nodes are color coded. (b) Transmissibilities recorded at the four corner nodes of the lattice.

recorded at the four corners of the lattice by the displacement of the excitation point. As expected, all four corners display a bandgap in their transmissibility; this attenuation region matches the one observed in the unit cell analysis of the same configuration (Fig. 3.16b). Note that the cut-off observed at $\omega \approx 2.8\,\omega_0$, which is consistent with the absence of modes above that frequency in the dispersion relation, is due to the discrete nature of our model (which has a finite number of degrees of freedom). In Fig. 3.18, on the other hand, we report the response of a lattice where the only masses featuring resonators (yellow masses in Fig. 3.18a) are located in the top-right quadrant. As shown in Fig. 3.18b, this modification of the lattice causes the appearance of a partial bandgap along the direction connecting the excitation point to the $(22, 22)$ mass, while the responses along the other directions are not significantly affected by the presence of the resonators. Clearly, placing resonators in other sub-regions would produce partial bandgaps along other directions.

Our strategy relies on the mutual interaction between the inherent anisotropy of the response of a periodic medium and the partial bandgaps generated by strategically placing resonators as in Fig. 3.18. To harness the strongest anisotropy, we excite the lattice

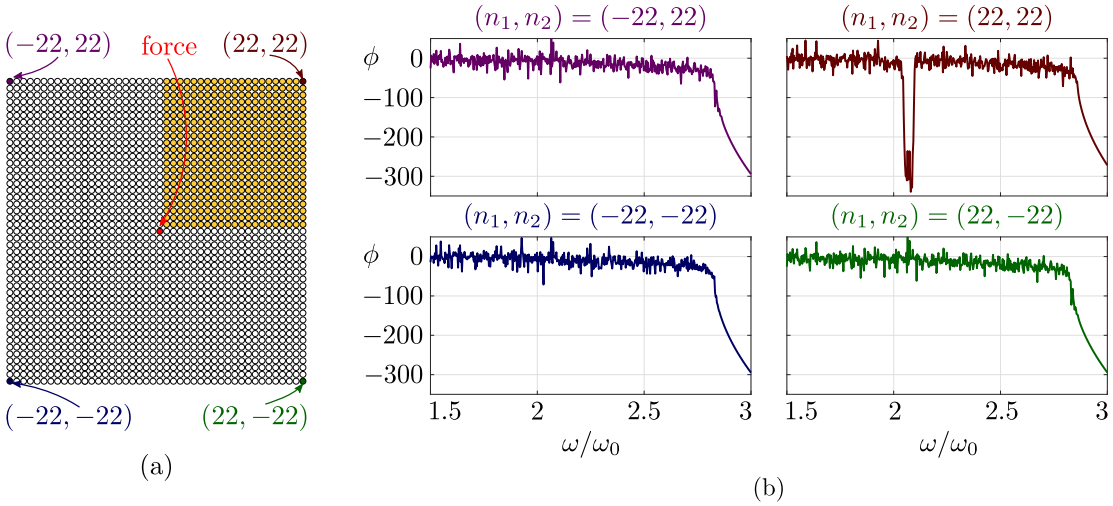


Figure 3.18: Steady state response of a lattice with resonators located in the top-right quadrant only. (a) Illustration of the square lattice structure. In this representation, yellow masses feature resonators, while white ones do not. The red point indicates the node where the force is applied. The corner nodes are color coded. (b) Transmissibilities recorded at the four corner nodes of the lattice.

with a burst signal with carrier frequency $2.07\,\omega_0$. To maximize the influence of the resonators on the transient wave, and recalling that the onset of a locally-resonant bandgap coincides with the resonators' natural frequency, we tune them at the carrier frequency of the burst. Recall, from Fig. 3.14, that this frequency corresponds to a propagation pattern with beaming along $\pm 45^{\circ}$-oriented directions for a lattice without resonators. The response of a $45\times45$ pristine lattice, shown in Fig. 3.19a, to a signal whose time evolution and frequency spectrum are shown in Fig. 3.19b, is reported in Figs. 3.19c-d. The wavefields show an "x-shaped" response that is consistent with the unit cell analysis prediction, and their main feature is represented by four spatially confined packets propagating along the $\pm 45^{\circ}$-oriented directions. Our goal is to remove one (or multiple) of these packets through the introduction of resonators and the activation of partial bandgaps. The first example of the application of this strategy is shown in Fig. 3.20, where all the masses in the top-right quadrant of the domain feature resonators. The wavefields in Fig. 3.20c and the time histories at the corner nodes in Fig. 3.20d show that, as expected, the top-right portion of the domain is significantly de-energized by the presence of the resonators. As a result, one of the four original packets is attenuated

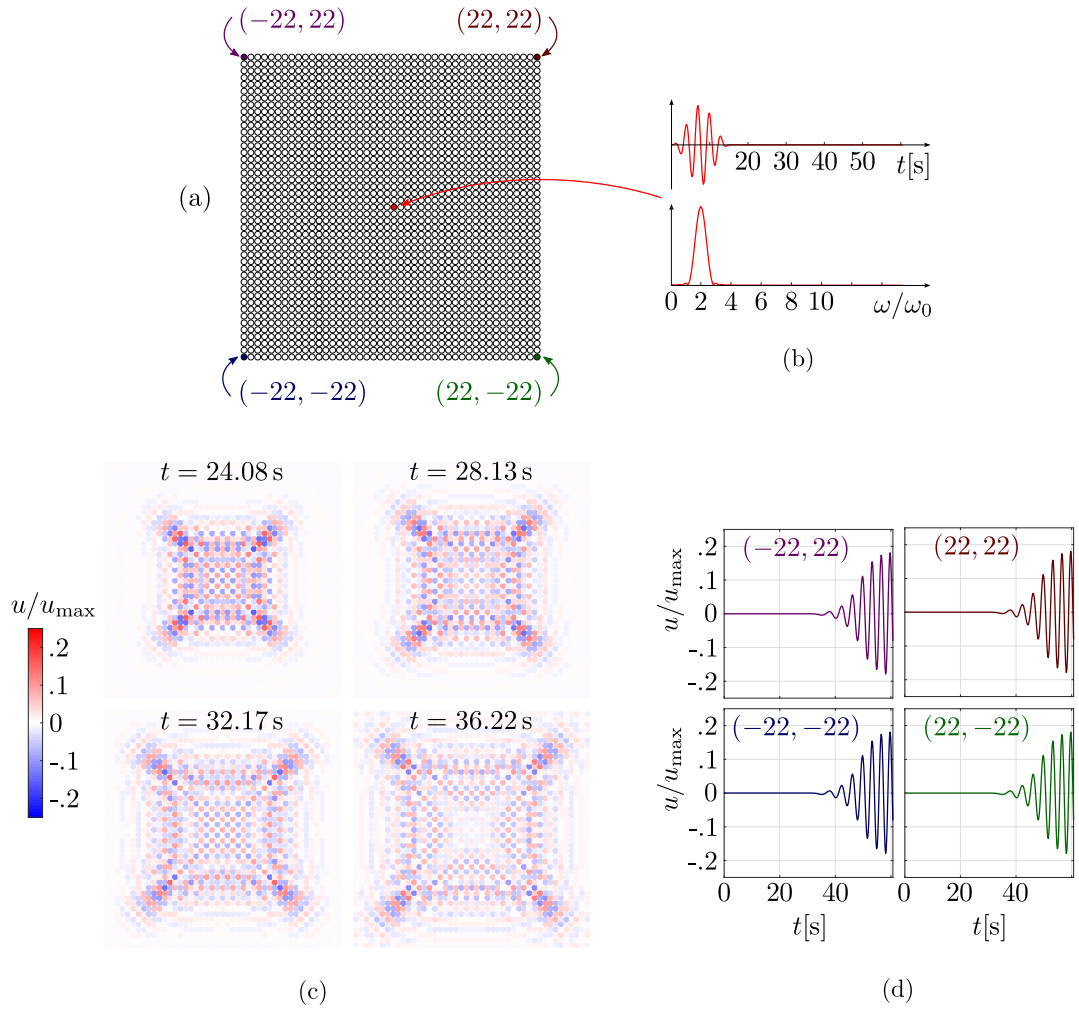


Figure 3.19: Transient response of a square lattice of springs and masses, without resonators. (a) Lattice configuration with color-coded key points. (b) Input signal—5 cycle burst with carrier frequency $\Omega = 2.07\,\omega_0$. (c) Displacement wavefields at four time instants. (d) Time histories at the four corners of the lattice.

and the wave response loses its two-fold symmetry. Other wave focusing scenarios can be obtained by introducing resonators in other portions of the domain. As an example, in Fig. 3.21, we show the response of the lattice shown in Fig. 3.21a, where the masses in both the top-right and the bottom-right quadrants are connected to resonators. As expected, the response is attenuated in the whole right portion of the domain. It is worth pointing out that the amount of distinct wave focusing effects achievable with

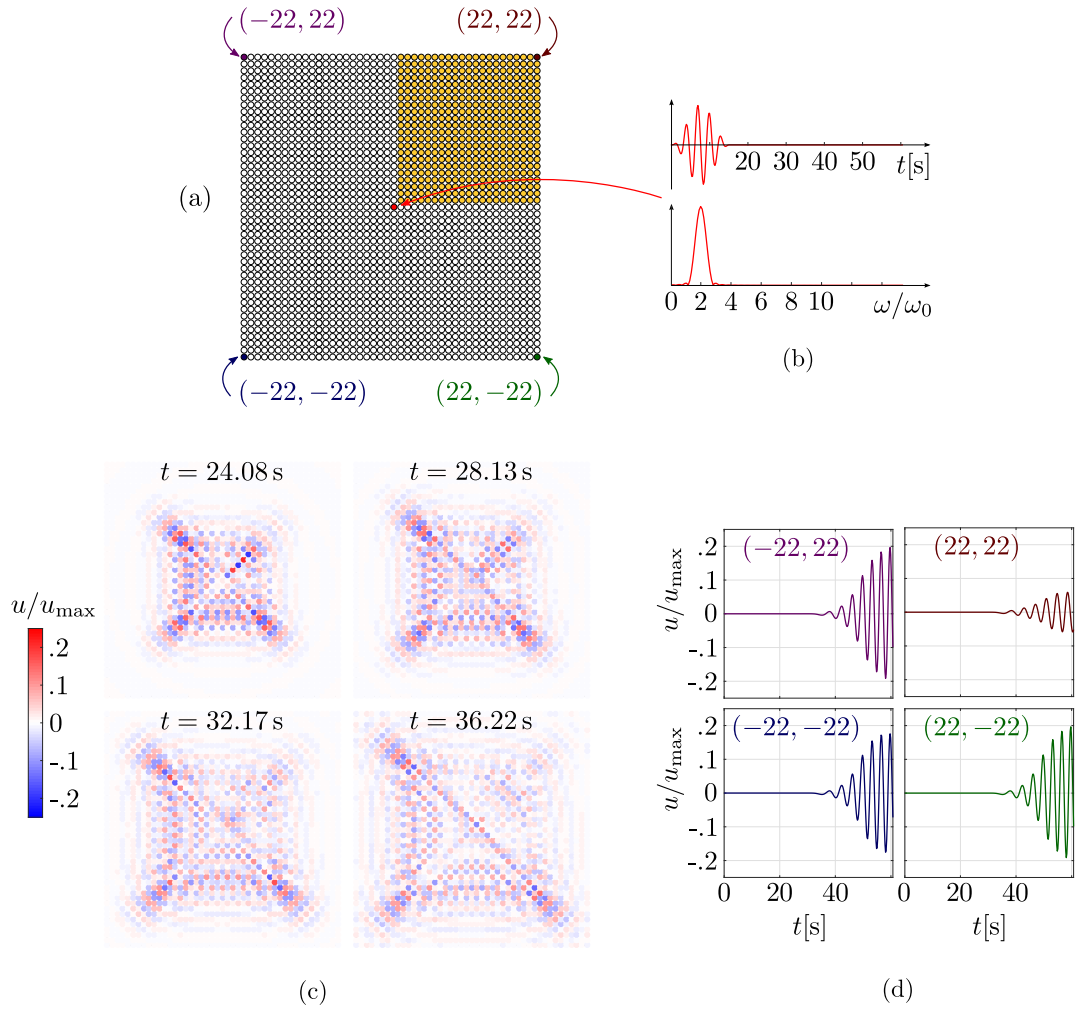


Figure 3.20: Transient response of a square lattice of springs and masses, with resonators connected to the masses belonging to the top-right quadrant of the domain. (a) Lattice configuration with color-coded key points. (b) Input signal—5 cycle burst with carrier frequency $\Omega = 2.07\,\omega_0$. (c) Displacement wavefields at four time instants. (d) Time histories at the four corners of the lattice.

this strategy is symbiotic to the richness of anisotropic characteristics of the considered cellular medium. In the case of the mono-modal spring mass lattice discussed in this section, the wave focusing scenarios that can be produced are inevitably limited.

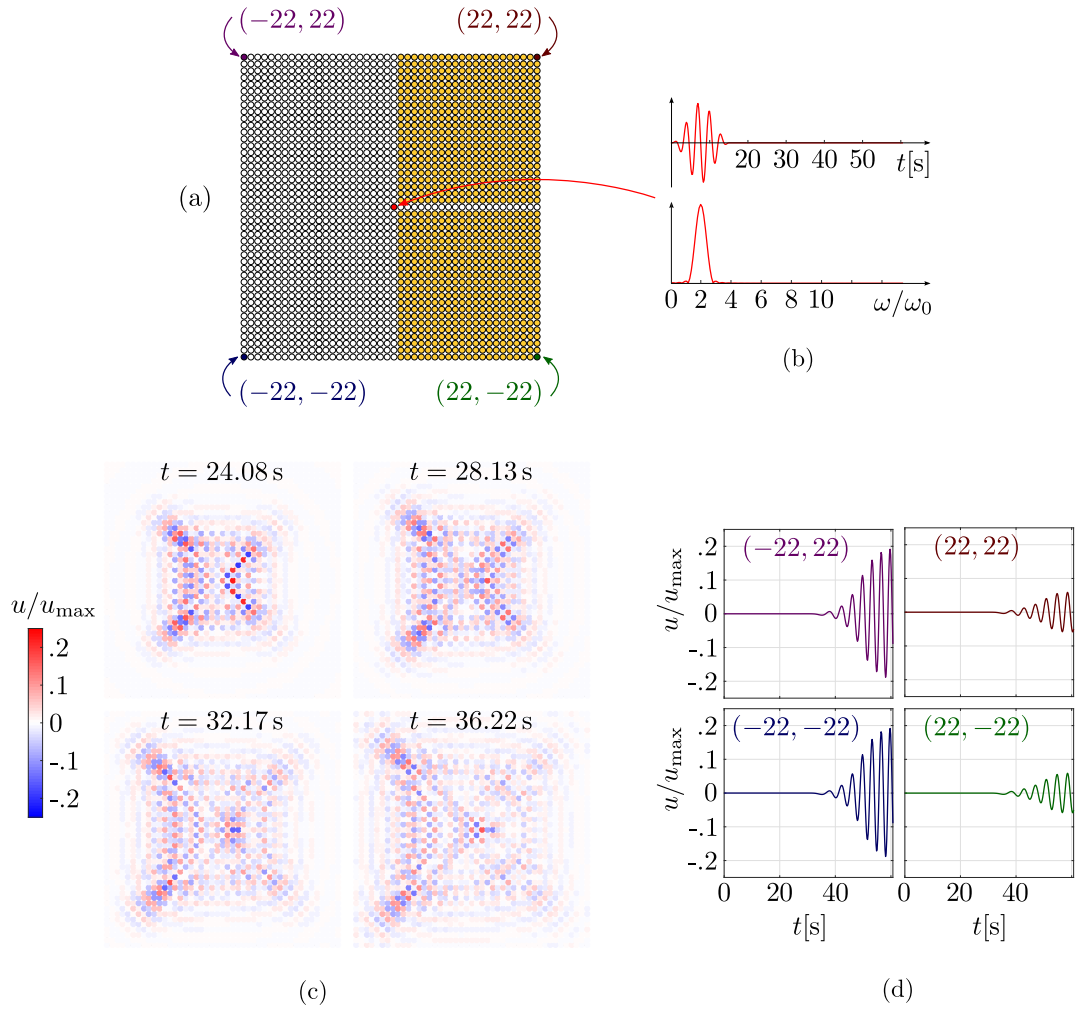


Figure 3.21: Transient response of a square lattice of springs and masses, with resonators connected to the masses belonging to the top-right and bottom-right quadrants of the domain. (a) Lattice configuration with color-coded key points. (b) Input signal—5 cycle burst with carrier frequency $\Omega = 2.07\,\omega_0$. (c) Displacement wavefields at four time instants. (d) Time histories at the four corners of the lattice.

### 3.3.4 Minimizing the number of resonators

So far, we have shown the effectiveness of the anisotropy overriding strategy in the context of lattice structures where entire quadrants of the domain feature resonators. Deploying large numbers of resonators may however be impractical in experimental

applications. With these constraints in mind, we are now interested in understanding how the number of resonators impacts the achievable symmetry modification of the anisotropic patterns, thus determining some lower bounds that can be valuable in designing effective—yet parsimonious—wave control strategies. To carry out this parametric analysis, we only introduce resonators in a square portion of the domain (with varying number of masses per side labeled by N) whose bottom left corner is fixed to the $(1, 1)$ mass. Some of the considered square sub-domains are highlighted by yellow boxes in Fig. 3.22. The comparison between different configurations is carried out by

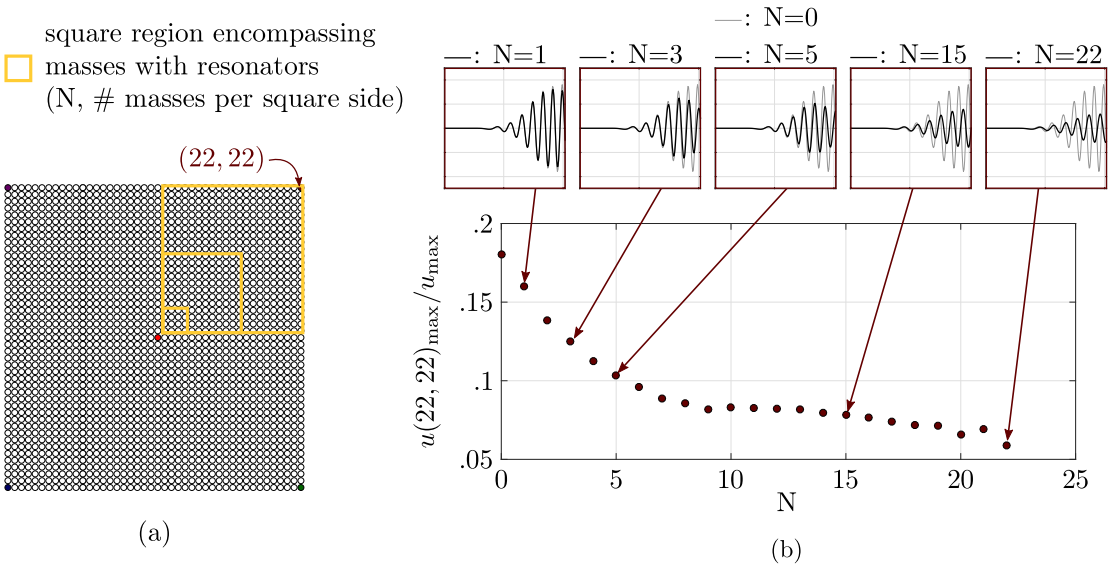


Figure 3.22: Dependence of anisotropy overriding on the number of resonators. (a) Lattice featuring a varying number of resonators arranged within a square portion of the domain comprising N masses per side and having bottom-left corner at the $(1, 1)$ mass. (b) Maximum displacement recorded at the $(22, 22)$ corner, versus N. The black lines in the inserts show the wave responses for selected numbers of masses, while the baseline gray lines represent the case without resonators.

plotting the maximum displacement recorded at the top-right corner, $u_{\max}(22, 22)$ (normalized by the maximum displacement recorded in the whole domain, $u_{\max}$) against the number of masses per each side of the square subdomain featuring resonators. This trend is illustrated in Fig. 3.22b. For N smaller than 10, the amplitude of the displacement decreases exponentially with N, while for N greater than 10, the decrease is much less pronounced. This suggests that introducing more than $10\times10$ resonators

does not produce any significant advantage in terms of attenuation. Most importantly, the exponential nature of the first part of the curve highlights how we can obtain significant attenuation effects and therefore obtain the desired wave patterns even with a limited number of resonators. This fact will be crucial in Chapter 5 when we will try to experimentally validate a tunable version of this strategy.

### 3.3.5 Final notes on anisotropy overriding

While a spatial wave manipulation strategy based on relaxed cell symmetry allows to obtain focused wavefields, it requires a large number of unit cells and, due to the fact that each cell comprises several resonators, a large number of resonators. With an eye towards experimental implementations of our ideas, we introduced a strategy based on anisotropy overriding by means of resonator-induced partial bandgaps, and we have shown how—in finite structures—this strategy allows to alter anisotropic propagation patterns even when only few strategically-placed resonators are involved.

# Chapter 4

# Reconfigurable cell symmetry via shunted-piezo control

## 4.1 An avenue towards tunable relaxed cell symmetry

In Section 3.2 we have proposed a strategy for spatial wavefield manipulation based on a microstructure-induced relaxation of the unit cell symmetry in cellular periodic structures. This methodology allows to achieve significant wave beaming in extremely low-frequency regimes, where wave propagation in conventional microstructure-free cellular solids would be either isotropic or directional with stellar multi-lobed features. As presented in the previous Chapter, however, this strategy presents one main drawback: the spatial manipulation that we can achieve is passive; attaining wave beaming along a different direction would require the design of a new medium (e.g. by selecting a different non-symmetric population of cantilevers in each unit cell).

To address the passivity issue, we devise a tunability strategy with a number of distinctive features with respect to pre-existing efforts. Let us recall that our one of our objectives is to keep the wave control functionality decoupled from the static behavior of the host lattice, whose shape, size, and ability to be integrated in larger structural systems ought to be preserved throughout the wave reconfiguration process. For this reason, we require the tunability strategy to only involve localized modifications at the auxiliary microstructure level. The key ingredients of this strategy are the following. We consider a unit cell architecture with a symmetric population of microstructural

elements (as shown in Fig. 3.1b), instrumented with piezoelectric elements (here piezo patches, i.e. thin wafers of piezoelectric material bonded to the cantilevers' sides). Note that piezoelectric materials, e.g. piezoelectric ceramic (PZT), allow to efficiently convert mechanical energy into electrical energy and vice-versa. Through this electromechanical coupling, we can modify the behavior of the piezoelectric phase of the composite cantilever beams; by tuning different cantilevers in a different fashion, we can either relax the symmetry of the unit cell geometry or the symmetry of the mechanical properties' distribution throughout the cell. This selective tuning results in the reversible activation and de-activation of distinct wave anisotropy patterns.

In this Chapter, following this philosophy, we pursue a strategy based on a local modification of the mechanical properties of the piezoelectric material phase through the tuning of passive circuits, or *shunts*, connected to the piezoelectric patches [61]. In the shunting circuit paradigm, piezoelectric elements convert the mechanical energy resulting from a vibration event into electrical energy, which is in turn manipulated at the circuital level. The unit cell of a cellular periodic structure featuring a symmetric population of microstructural elements instrumented with shunted piezoelectric patches, is shown in Fig. 4.1. One key aspect of our strategy is the independent controllability

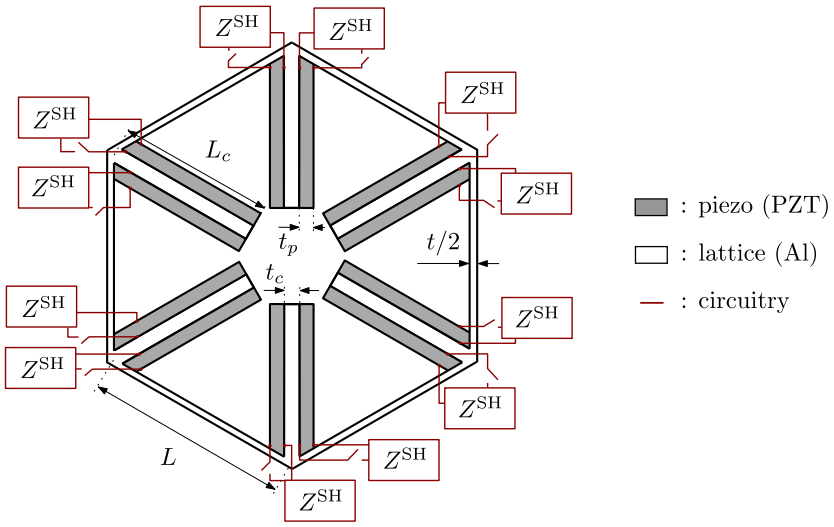


Figure 4.1: Unit cell with reconfigurable cell symmetry; the shaded regions correspond to piezoelectric patches. $Z^{\mathrm{SH}}$ is the equivalent electrical impedance of a shunting circuit.

of patches belonging to different cantilevers, which allows to endow them with different

equivalent mechanical properties and to attain non-symmetric, reconfigurable stiffness distributions throughout the cell.

## 4.2 Modeling PZT-Al composite lattices: Hagood and von Flotow formulation

As a benchmark case to test our strategy, we consider a regular hexagonal lattice with a symmetric population of piezo-instrumented cantilevers, sketched in Fig. 4.1. As usual, the links are modeled as Timoshenko beams. The characteristic dimensions used in the following are $L_c = 0.8\,L$, $t = 1/15\,L$, $t_c = t$, $t_p = t$. Each cantilever is instrumented with two thin piezoelectric elements. Note that, at this stage, patches are considered to be ideally bonded to the substrate and to extend to the roots of the cantilevers. The lattice has the material properties of Aluminum: $E = 71$ GPa (Young's modulus), $\rho = 2700\ \mathrm{kg\,m^{-3}}$ (density), $\nu = 0.33$ (Poisson's ratio). The piezo patches have the following properties: $E_p = 63$ GPa (Young's modulus), $\nu_p = 0.3$ (Poisson's ratio), $\rho_p = 7800\ \mathrm{kg\,m^{-3}}$ (density), $k_{31} = 0.35$ (electromechanical coupling factor when the only nonzero stress is along the patch axis). Each patch is considered to be connected to a separate passive shunting circuit, which realizes an electrical "extension" of the mechanical behavior of the cantilever [112].

Throughout the years, several shunting circuits have been proposed to attain control of mechanical vibrations. Among others, the most used have been the *resonant resistor-inductor* circuit, which causes the patch+circuit system to behave as an electromechanical resonator, and the *negative capacitance* circuit, which produces a broadband influence on the vibrational response of a structure. Regardless of the chosen circuit and its equivalent impedance, the behavior of shunted piezo patches can be studied by resorting to the theory developed by Hagood and von Flotow [113]. Starting from the linear piezoelectric theory, Hagood and von Flotow derived a formula for the equivalent mechanical modulus of the piezoelectric material ($E_p^{\mathrm{SH}}$) as a function of the equivalent impedance of the shunting circuit ($Z^{\mathrm{SH}}$):

$$E_p^{\mathrm{SH}}(\omega) = \frac{E_p}{1-k_{31}^2}\left(1 - k_{31}^2 \frac{1}{1 + i\omega\, C_p^{\varepsilon}\, Z^{\mathrm{SH}}(\omega)}\right) \quad , \tag{4.1}$$

where $E_p$ is the Young's modulus of the piezo medium (corresponding to a short-circuit

configuration), $k_{31}$ is the electromechanical coupling factor when the only nonzero stress is along the patch axis, $\omega$ is the frequency and $C_p^{\varepsilon}$ is the capacitance of the piezoelectric material at constant strain. It is interesting to see that setting $Z^{\mathrm{SH}}(\omega) = 0$ leads to the short-circuit modulus of the piezo medium, i.e., $E_p^{\mathrm{SH}}(\omega) = E_p$, while $Z^{\mathrm{SH}}(\omega) \to \infty$ leads to $E_p^{\mathrm{SH}}(\omega) = E_p/(1 - k_{31}^2)$, the open-circuit modulus. The electrical impedance $Z^{\mathrm{SH}}(\omega)$ depends on the selected shunting circuit configuration.

Once we select a shunting circuit and its parameters, we can calculate the equivalent properties of the composite cantilever microstructures. The cross section of one of the cantilever beams with two bonded piezoelectric patches, representative of a microstructural element, is shown in Fig. 4.2. Due to symmetry, the centroid of the cross section

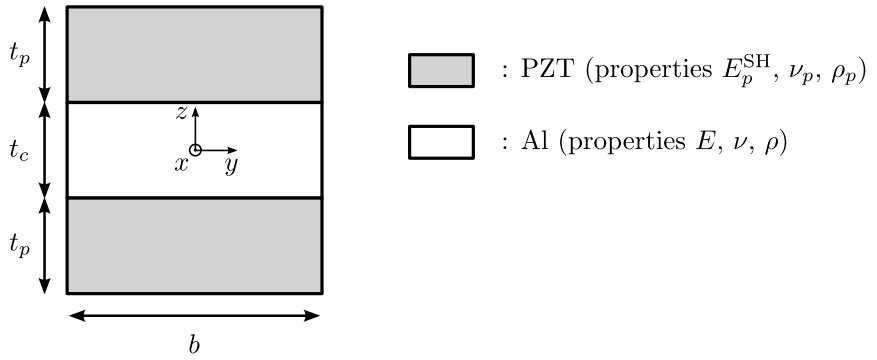


Figure 4.2: Cross-section of a composite beam made of two piezoelectric layers bonded to an Aluminum core. Note that the subscript $c$ is used for the geometrical quantities pertaining to the Al phase.

is located at the origin of the axes shown in the figure and the neutral axis is directed along $x$. Due to the composite nature of the beam, its properties are constant along $y$, and step-wise defined along the $z$ axis. In particular:

$$E(z) = \begin{cases} E & -t_c/2 < z < t_c/2 \\ E_p^{\mathrm{SH}} & -t_p - t_c/2 < z < -t_c/2\,,\ \ t_c/2 < z < t_p + t_c/2 \end{cases}, \tag{4.2}$$

and

$$\rho(z) = \begin{cases} \rho & -t_c/2 < z < t_c/2 \\ \rho_p & -t_p - t_c/2 < z < -t_c/2\,,\ \ t_c/2 < z < t_p + t_c/2 \end{cases}. \tag{4.3}$$

From beam theory, the distributed mass (mass per unit length, $m$) axial stiffness ($S$) and bending stiffness ($H$, with respect to bending about the $y$ axis) of a beam undergoing

bending and extension/compression are defined as

$$m = \int_{A_{cs}} \rho(z)\, dA \quad , \quad S = \int_{A_{cs}} E(z)\, dA \quad , \quad H = \int_{A_{cs}} E(z) z^2\, dA \quad , \tag{4.4}$$

where $A_{cs} = b\,(2t_p + t_c)$ is the cross-sectional area of the beam. Substituting Eq. 4.2 and Eq. 4.3 into Eq. 4.4, we obtain the equivalent properties of the cantilever beam with two bonded piezo patches [55]. The equivalent distributed mass is:

$$m_{c+p} = \rho\, t_c\, b + 2\, \rho_p\, t_p\, b \quad ; \tag{4.5}$$

the equivalent axial stiffness is:

$$S_{c+p} = E\, t_c\, b + 2\, E_p^{\mathrm{SH}}\, t_p\, b \quad , \tag{4.6}$$

and the equivalent bending stiffness is:

$$H_{c+p} = \frac{E\, b\, t_c^3}{12} + \frac{E_p^{\mathrm{SH}}\, b\left[(t_c + 2\, t_p)^3 - t_c^3\right]}{12} \quad . \tag{4.7}$$

Note that the depth of the cantilever, $b$, is set to 1.

## 4.3 The negative capacitance shunt

The shunting circuit we consider in this chapter is the negative capacitance. This circuit is based on the negative impedance converter (NIC) shown in Fig 4.3a and whose fundamental element is an operational-amplifier (Op-Amp). The equivalent impedance of the NIC is:

$$Z_{\mathrm{eq}} = -\frac{Z_3\, Z_1}{Z_2} \quad , \tag{4.8}$$

where $Z_1$, $Z_2$ and $Z_3$ are the impedances shown in Fig 4.3a. A sketch of one of the possible configurations of the negative capacitance circuit is shown in Fig. 4.3b where, out of the many implementations available, we choose to follow the guidelines given by Beck et al. [114, 115, 116]. Since this is a shunting circuit, its equivalent impedance is labeled $Z^{\mathrm{SH}}$ and consists of two parts in series: a resistive part, due to the presence of $R_{\mathrm{S}}$, and a part that can be calculated following the same logic used for the NIC, with the following impedances

$$Z_1 = \frac{1}{i\omega\, C + \frac{1}{R_2}} \quad , \quad Z_2 = R_4 \quad , \quad Z_3 = R_3 \quad . \tag{4.9}$$

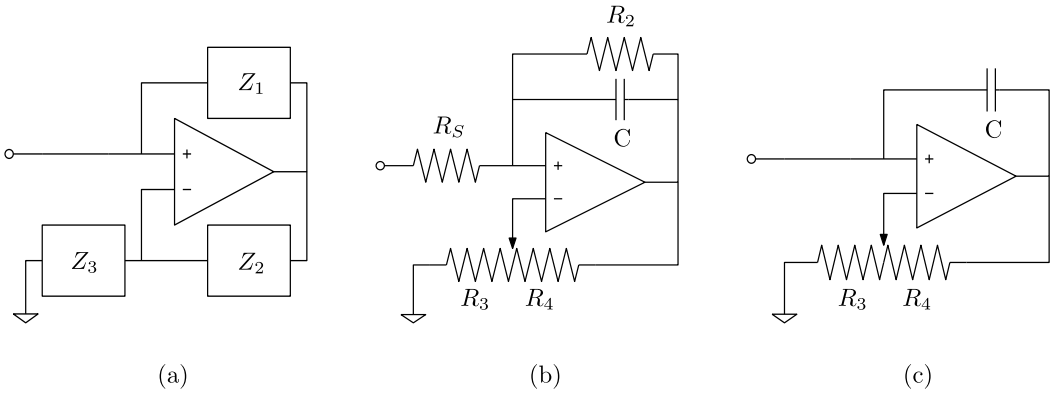


Figure 4.3: (a) Negative impedance converter (NIC). (b) Negative capacitance circuit as discussed in Beck [114]. (c) Simplified negative capacitance circuit used in our analysis.

Therefore, the equivalent impedance of the circuit in Fig. 4.3b is

$$Z^{\mathrm{SH}}(\omega) = R_{\mathrm{S}} - \frac{R_3}{R_4}\,\frac{1}{i\omega\,C + \frac{1}{R_2}} \quad . \tag{4.10}$$

The presence of the capacitor causes $Z^{\mathrm{SH}}$ to depend on the frequency $\omega$. According to Beck et al., the formula in Eq. 4.10 can be simplified without loss of generality. First, the resistor $R_2$, necessary for the stability of the Op-Amp at DC, can be neglected if the operating frequencies are sufficiently high, as in our analysis. $R_{\mathrm{S}}$, whose presence is required in practical realizations of the circuit, can be selected small enough to be negligible. Based on these simplifications, we achieve the simplified circuit sketched in Fig. 4.3c, whose equivalent impedance is

$$Z^{\mathrm{SH}}(\omega) = -\frac{R_3}{R_4}\,\frac{1}{i\omega\,C} = -\frac{1}{i\omega\,C_{eq}} \quad , \tag{4.11}$$

where we defined the equivalent (positive) capacitance of the circuit as $C_{eq} = (R_4\,C)/R_3$.

In light of this discussion, we can derive the equivalent modulus of a piezoelectric medium shunted with a negative capacitance circuit by substituting Eq. 4.11 into Eq 4.1 to obtain

$$E_p^{\mathrm{SH}} = \frac{E_p}{1-k_{31}^2}\left(1 - k_{31}^2\frac{1}{1-\frac{R_3\,C_p^{\varepsilon}}{R_4\,C}}\right) \quad . \tag{4.12}$$

Due to the above-mentioned simplifications, the frequency drops out of the equivalent

modulus formula. Finally, defining the *negative capacitance ratio* as

$$\lambda = \frac{C_{eq}}{C_p^{\varepsilon}} = \frac{R_4}{R_3}\frac{C}{C_p^{\varepsilon}} \quad , \tag{4.13}$$

we obtain the final formula for $E_p^{\mathrm{SH}}$ used in our computations:

$$E_p^{\mathrm{SH}} = \frac{E_p}{1-k_{31}^2}\left(1 - k_{31}^2\frac{\lambda}{\lambda-1}\right) \quad . \tag{4.14}$$

In this negative capacitance case, $E_p^{\mathrm{SH}}$ is a real quantity and, therefore, corresponds to the actual corrected Young's modulus of the piezoelectric material. From this formula, we understand that the tuning of the negative capacitance circuit can be performed, at least theoretically, by modifying the $\lambda$ parameter. Note that, as it will be shown in later Chapters, implementing and tuning shunting circuits is not as simple as it would seem when reading theoretical works on the topic. To understand the influence of the negative capacitance ratio on the equivalent modulus, we plot the ratio $E_p^{\mathrm{SH}}/E_p$ for various $\lambda$ values in Fig. 4.4. As expected from the inspection of Eq. 4.14, $\lambda = 0$ leads

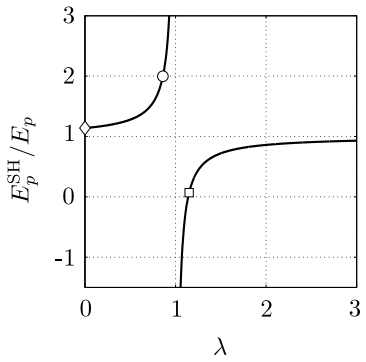


Figure 4.4: Dependence of the ratio $E_p^{\mathrm{SH}}/E_p$ on the negative capacitance ratio $\lambda$. The markers correspond to $\lambda$ values of interest: the diamond corresponds to $\lambda = 0$ (open circuit), the circle to $\lambda = 0.85$ (stiffening) and the rectangle to $\lambda = 1.15$ (softening).

to an open-circuit configuration and $\lambda \to \infty$ to a short-circuit configuration. $\lambda = 1$ is an asymptote of the plot and corresponds to a sudden reversal between the stiffening ($\lambda < 1$) and the softening ($\lambda > 1$) behavior of the circuit. Throughout this work, we either choose a value of $\lambda$ that yields large softening ($\lambda = 1.15$) or resort to an open-circuit configuration ($\lambda = 0$).

## 4.4 Theoretical implications of symmetry relaxation

We now consider a unit cell and shunt only the patches belonging to cantilevers oriented $30^o$ counterclockwise with respect to the horizontal direction (i.e. cantilevers 2 and 5 according to the labeling in Fig. 3.1b), while leaving the others open-circuited. This relaxed cell symmetry configuration, labeled RCS in the following, is shown in Fig. 4.5a, where the darker patches are shunted. Given its symmetry landscape, this cell configuration belongs to group 2 in Fig. 3.4. A negative capacitance ratio $\lambda = 1.15$, corresponding to a softening regime, is selected. We compare the results of a unit cell analysis for the RCS configuration with those for a case with all open-circuited patches, called OPEN configuration and sketched in Fig. 4.5b. Note that, once more, all frequencies are normalized by the first natural frequency of a pinned-pinned beam having length $L$, thickness $t$, unit depth and material properties of Aluminum. The band diagram in Fig. 4.5c shows that, especially in the $4^{th}$ branch region (in the neighborhood of $\Omega = 0.3$), the dispersion relations of the two configurations coincide along the OC direction, but diverge along OA. Iso-frequency contours (Figs. 4.5d-e) and phase velocity plots (Figs. 4.5f-g) for the $4^{th}$ branch and for both configurations highlight that the shunting-induced modification of the spatial distribution of mechanical properties produces a relaxation of the symmetry of the metamaterial response (consistent with the symmetry scenario of the response of group 2 in Fig. 3.4). In particular, from Fig. 4.5f, we can appreciate the generation of single-lobed spatially-confined beams at $\Omega = 0.405$ along a direction that corresponds to OC (according to the nomenclature of the Brillouin zone in Figs. 4.5d-e).

## 4.5 Wave beaming scenarios

The effect of symmetry relaxation on the wave propagation patterns is further analyzed via full-scale simulations of a metamaterial domain comprising $50 \times 48$ unit cells. Note that the large lattice size is here adopted to enhance visualization, while similar effects would also be recorded in smaller domains. The excitation is a 5-cycle tone burst with carrier frequency $\Omega = 0.405$ applied to the midpoint of the upper boundary. In Fig. 4.6a we report the potential energy field (at one time instant) corresponding to a case in which all the unit cells are in the OPEN configuration. Fig. 4.6b corresponds instead to the

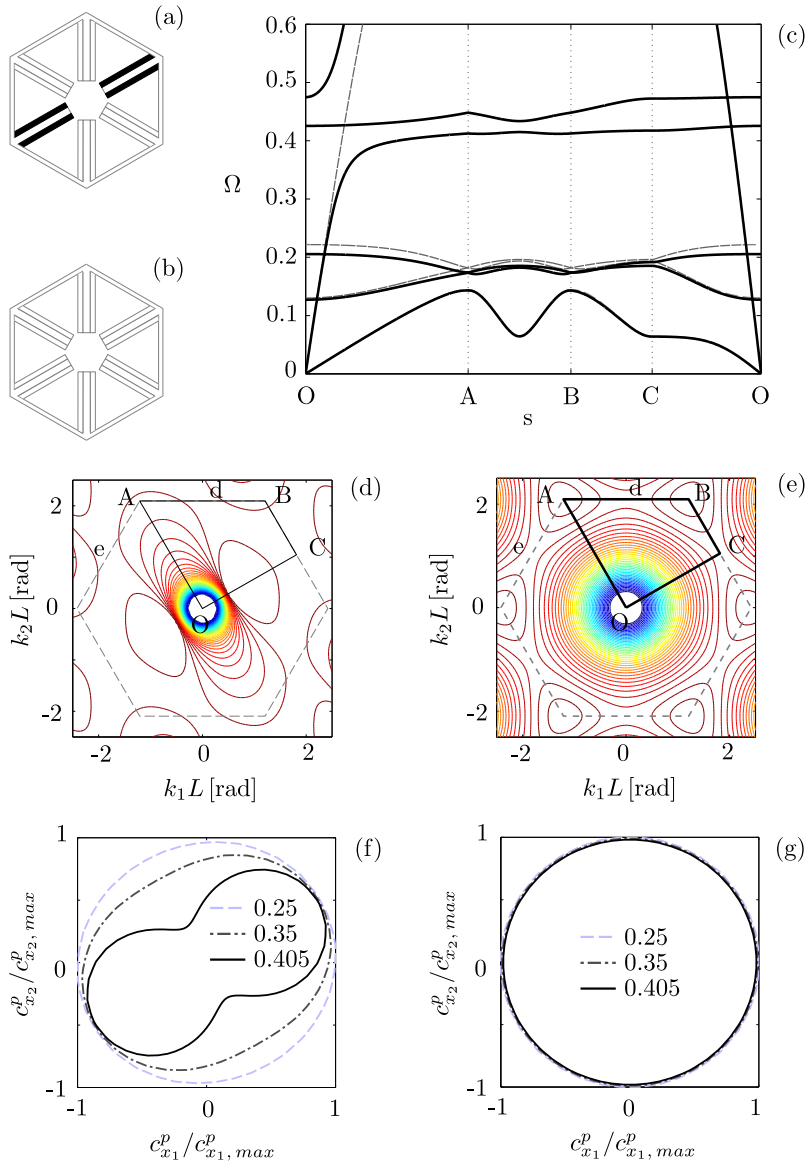


Figure 4.5: (a) RCS cell: 30°-inclined patches (shaded) are shunted with $\lambda = 1.15$, others (white) are open-circuited. (b) OPEN cell: all patches are open-circuited. (c) Band diagram: continuous and dashed lines correspond to RCS and OPEN configurations, respectively. (d), (e) Iso-frequency contours of the $4^{th}$ dispersion surface for RCS and OPEN cases, respectively; lines and letters mark the Brillouin zones. (f), (g) Phase velocity plots of the $4^{th}$ branch for RCS and OPEN configurations.

case where all cells are in the RCS configuration (for the same time instant) . The single-

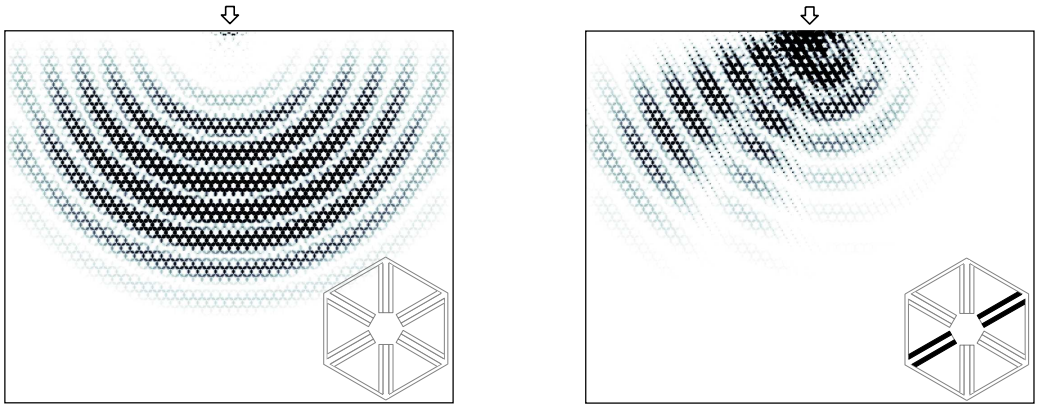

(a) (b)

Figure 4.6: Comparison of potential energy fields (recorded at the same time instant, for an excitation with carrier frequency $\Omega = 0.405$ applied to the point indicated by the white arrow) for two shunting strategies. The shunting configurations are sketched: the white patches are open-circuited and the shaded ones are shunted. (a) All patches are open-circuited. (b) Only the $30^{o}$-inclined patches are shunted with $\lambda = 1.15$.

lobe beaming predicted by the unit cell analysis is confirmed in the transient wavefield: the RCS configuration (Fig. 4.6b), unlike the OPEN one (Fig. 4.6a), produces a highly-directional wavefield with principal direction of propagation along OC, consistently with the phase velocity plot in Fig. 4.5f. Note that, in this venue, we only report one of many tunable directional scenarios that can be activated based on the same unit cell geometry. While the $4^{th}$ branch of the band diagram at frequency $\Omega = 0.405$ offers the most conspicuous steering effects, other branches and frequencies produce appreciable directional patterns. Additionally, other values of $\lambda$ corresponding to different shunting conditions, both softening and stiffening, could also be leveraged to obtain different responses.

So far, we have discussed the ability to control individual subsets of cantilevers, but always prescribing the same activation patterns in each unit cell and preserving periodicity throughout the cellular medium. The ability to control each patch through a dedicated shunt can be exploited to prescribe different activation sequences (and symmetry relaxation patterns) to different sub-regions of the domain. To illustrate this aspect, we report two cases of multi-zone programmability. In both cases, we preserve

the loading conditions of the examples above, while considering a smaller ($50 \times 24$ cells) domain. The wavefield in Fig. 4.7a, obtained by prescribing diverging symmetry

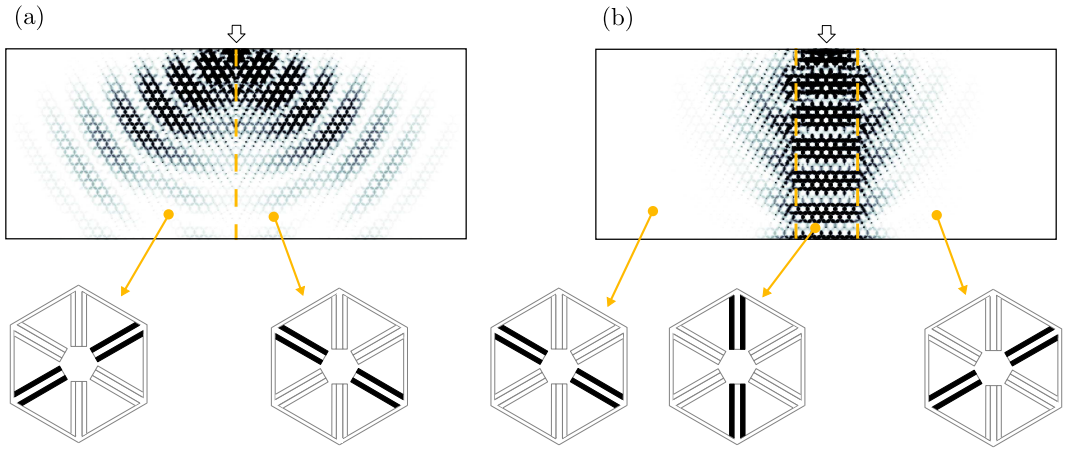


Figure 4.7: Examples of different acoustic ports achievable via multi-zone shunting strategies. Dashed lines are used to separate the regions of the domain whose unit cells are shunted differently. The shunting sequences used in each sub-domain are reported in the schematics underneath the energy fields. (a) *Energy splitting* case. (b) *Energy focusing* case.

relaxation patterns to the left and right zones of the domain, realizes an *energy splitter*, in which the energy is evenly partitioned between the two halves, while the central region remains de-energized. A second shunting strategy, obtained by flipping the symmetry landscapes, results in an *energy-focusing* effect, shown in Fig. 4.7b, where the energy is channeled along the vertical axis of the domain.

## 4.6 An alternative avenue towards tunable relaxed cell symmetry

Recent advances in the field of soft active materials have opened new opportunities for tunability in metamaterial systems [64, 65, 82, 66, 117, 118, 67]. In light of these recent advances, we could leverage *localized* and *reversible* shape modifications as an alternative route to achieve corrections of the spectro-spatial wave control characteristics in the context of soft cellular structures [68]. The shape modifications are internal and *localized*, since, similarly to the equivalent properties modifications discussed in Chapter 4,

they occur at the level of an *auxiliary microstructure* comprising non-structural cantilever elements. The *reversibility* comes from the fact that the cantilevers are equipped with smart actuators (here we consider layers of P(VDF-TrFE-CTFE) electrostrictive terpolymer [119] on a PDMS substrate). Excited with an external (electrical, in this case) stimulus, the actuators cause the auxiliary cantilevers to *curl* (i.e., experience extreme—yet reversible—rolling deformation), thus modifying their dynamic properties and their effect on the global wave manipulation capabilities of the medium. This strategy is a logical continuation of the paradigm discussed in Section 3.2. However, thanks to the dramatic shape modifications that can be achieved, this twist on the relaxed cell symmetry idea is expected to produce more pronounced effects than the previously-discussed implementation, which merely relied on material property corrections. For details on soft microstructural curling, please refer to our article in *Smart Materials and Structures* [68].

# Chapter 5

# Dispersion overriding via tunable electromechanical resonators

## 5.1 Overcoming the impracticality of tunable relaxed cell symmetry

As illustrated in Chapter 4, a spatial wave manipulation strategy based on a relaxation of the unit cell symmetry in cellular periodic structures with auxiliary microstructures is an elegant approach which can be made tunable through the introduction of smart material inserts. However, demonstrating the resulting spatial wave effects in an experimental setting is challenging, due to the fact that all active cantilevers need to be individually instrumented, wired and tuned, and since large numbers of unit cells are needed to establish these effects. On the other hand, as shown in Section 3.3, a strategy based on anisotropy overriding only requires a limited number of resonators to achieve potentially significant effects—making it more amenable to proof-of-concept experimental investigations. In this Chapter, we discuss the experimental realization of this strategy by resorting to tunable electromechanical resonators consisting of piezoelectric patches shunted with resistor-inductor circuits. This experimental campaign comprises two sequential efforts. First, we implement and characterize the tunable dispersion overriding capabilities (frequency distillation) of single—and arrays of—electromechanical resonators in the context of waves propagating in a one dimensional beam/waveguide.

Then, we characterize the wave behavior of a two-dimensional square lattice structure and we show some preliminary results related to tunable anisotropy overriding.

## 5.2 Resistor-inductor shunting circuits

In Chapter 4, we have already introduced some fundamental notions on the behavior of piezoelectric patches shunted with passive electrical circuits. In that context, we introduced the negative capacitance shunt. In this Chapter, we consider another popular shunting circuit, the resistor-inductor (RL), that has already been mentioned when discussing tunability strategies in the literature review of Section 1.3. The interest in this type of shunt comes from the fact that, by placing a RL circuit in series with a piezoelectric element (which can be modeled electrically as a voltage generator in series with a capacitor) we obtain a RLC system, i.e. an electrical resonator. In this case, the resonator we obtain can be considered to be electromechanical due to the coupling provided by a piezoelectric wafer. In analogy with purely-mechanical resonant systems, the electromechanical resonator has a natural frequency that can be determined from the circuit parameters as

$$f_{res} = \frac{1}{2\,\pi}\sqrt{\frac{1}{L\,C_p}}\ , \tag{5.1}$$

where $C_p$ is the capacitance of the piezo. The resistance $R$, which is directly proportional to the level of damping introduced in the structure, if not small, can affect the natural frequency of the resonant shunt.

### 5.2.1 The equivalent mechanical properties of RL-shunted patches

The equivalent mechanical behavior of a piezoelectric element shunted with a RL circuit can be modeled following Hagood and von Flotow's formulation, as we did for the negative capacitance shunt in Section 4.2. The equivalent impedance of an RL circuit is

$$Z_{\text{eq}} = R + i\omega L\ , \tag{5.2}$$

where $R$ is the resistance, $L$ is the inductance and $\omega$ is the angular frequency. Let us now recall Hagood and von Flotow's formula for the equivalent modulus of a piezoelectric

medium as a function of $Z_{\text{eq}}$ (Eq. 4.1):

$$E_p^{\text{SH}}(\omega) = \frac{E_p}{1-k_{31}^2}\left(1 - k_{31}^2 \frac{1}{1 + i\omega\, C_p^{\varepsilon}\, Z^{\text{SH}}(\omega)}\right) \ , \tag{5.3}$$

where $E_p$ is the Young's modulus of the piezoelectric medium (corresponding to a short-circuit configuration), $k_{31}$ is the electromechanical coupling factor when the only nonzero stress is along the patch axis, and $C_p^{\varepsilon}$ is the capacitance of the piezoelectric material at constant strain. Plugging Eq. 5.2 into Eq. 5.3, we obtain

$$E_p^{\text{SH}}(\omega) = \frac{E_p}{1-k_{31}^2}\left(1 - k_{31}^2 \frac{1}{1 + i\omega\, C_p^{\varepsilon}\, R - \omega^2 C_p^{\varepsilon}\, L}\right) \ . \tag{5.4}$$

The formula highlights that the presence of a resistor—the electrical analog of a damper—leads to a complex modulus $E_p^{\text{SH}}$. Moreover, unlike the negative capacitance shunt case, the modulus depends on the frequency $\omega$. This frequency dependence makes the time-domain modeling of the transient behavior of structures with RL-shunted piezos challenging, especially when the signals involved have a broadband frequency content. To bypass this difficulty, we move straight to implementing an approach based on experimental characterizations only.

### 5.2.2 Experimental implementation of the RL shunt

Given the very small capacitance values of the piezoelectric patches we adopt (of the order of 1 nF), and given the fact that we want to operate at relatively low frequencies (of the order of 1000 Hz), the inductances required to achieve resonant conditions in the desired range could vary in between 0.01 H and 10 H. Such values of inductance are achievable with conventional coil-based inductors, using devices with characteristic sizes of the order of few centimeters. To avoid working with inductors of impractical dimensions, it is customary to resort to *synthetic inductors*, i.e. circuits which artificially mimic the electrical behavior of conventional inductors. An example is the *Antoniou circuit* [120], that involves two operational amplifiers, a capacitor and four resistors, arranged as sketched in Fig. 5.1a. The equivalent inductance can be calculated as:

$$L_{eq} = \frac{R_1\, R_3\, R_4\, C}{R_2} \quad . \tag{5.5}$$

Another major advantage of using this circuit is the fact that the value of the equivalent inductance can be modified by simply tuning one of the components. This feature is

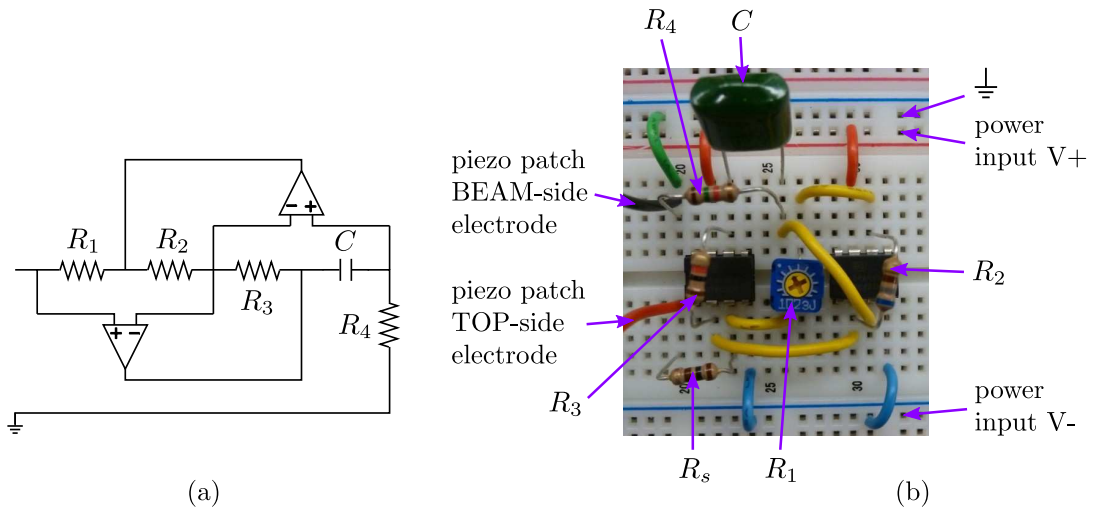


Figure 5.1: Antoniou's circuit, used in our work as synthetic inductor. (a) Circuit schematic. (b) Realization of the circuit on a breadboard, featuring a series resistor $R_s$ and a tunable potentiometer in lieu of $R_1$.

especially important in the context of our work, as tunability of the response is a key objective. In our case, as visible in the realization of the circuit on a breadboard shown in Fig. 5.1b, the tunable component is the potentiometer corresponding to $R_1$, which can assume values in the 100–1000 Ω range. Tuning $R_1$ allows to modify the equivalent impedance $L_{\text{eq}}$ and, in return, the resonant frequency of the circuit, thus effectively modifying the way in which the patch interacts with an incident wave. Another important aspect of the circuit realization is represented by the fact that it is best to choose circuit components providing a minimal *parasitic resistance*—a resistance that is inherent to any circuit component [121, 63]. For this reason, we use capacitors of the Mylar type, instead of electrolytic ones. Also, all the results in this Chapter have been obtained with circuits featuring operational amplifiers of the OPA445 type (TI OPA445AP). The amplifiers are powered by two DC power supplies (BK Precision 1667) arranged in series as to share the same ground and produce a voltage difference of ±30 V. It is important to point out that the ground terminal coming from the power supplies is used as reference ground for the circuits as well as for the patches.

## 5.3 Tunable dispersion overriding in 1D

In this Section, we study the interaction of flexural elastic waves with RL-shunted piezoelectric patches bonded to a long Aluminum beam. Our aim is to characterize the behavior of these electromechanical resonators and their tunable characteristics, in order to understand how to properly deploy them in the context of anisotropy overriding. First, we consider a beam featuring a single piezoelectric patch. Then, we show that more dramatic effects (both in terms of strength and broadbandedness) can be achieved when using multiple shunted patches simultaneously.

### 5.3.1 Experimental setup

Our experimental setup for the case of a beam featuring a single piezoelectric patch is shown in Fig. 5.2a. Note that the setup is identical, albeit comprising more circuits, to

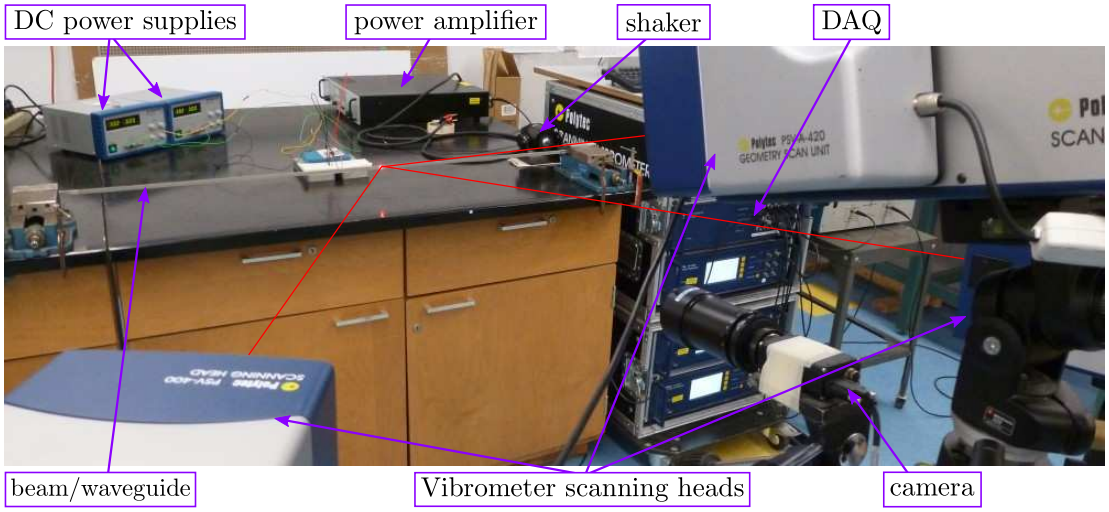


Figure 5.2: Experimental setup to investigate the behavior of beams featuring piezoelectric patches shunted with RL circuits.

the one we will later on consider for the experiments on beams with multiple patches. The specimen we consider is a 6061 Aluminum beam clamped at both ends (the total length of the beam is 117.4 cm, its thickness is $t = 1.27$ mm and its width $t = 9$ mm). A detail of the beam is shown in Fig. 5.3a. The beam features a single piezoelectric patch (STEMiNC, part number SMPL7W8T02412WL), whose dimensions are $8\,\text{mm} \times 7\,\text{mm} \times$

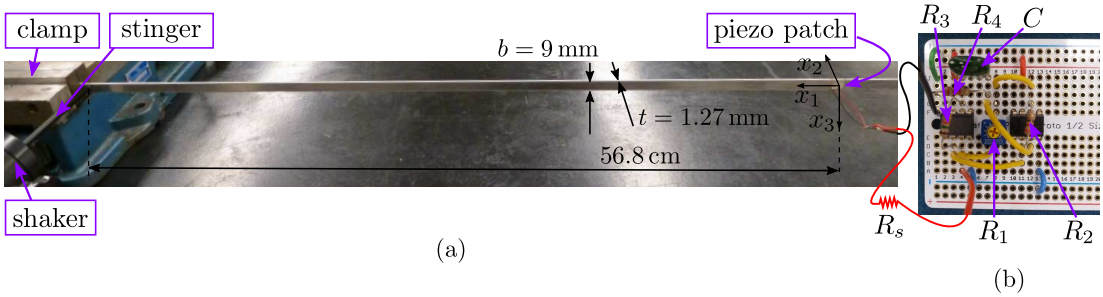


Figure 5.3: (a) Detail of the beam, with its characteristic dimensions, in the single-patch configuration. (b) Detail of the synthetic inductor built on a solderable breadboard.

0.2 mm along $x_1$, $x_3$ and $x_2$, respectively, located roughly at the center of the beam. The patches are bonded to the Al substrate by means of a two-part epoxy glue (3M Scotch-Weld 1838 B/A). The electrodes of the patch are connected to a synthetic inductor, shown in Fig. 5.3b, which is built on a solderable breadboard (Adafruit ADA571). Throughout this work, solderable breadboards are used in place of conventional ones to obtain more reliable permanent connections. As far as the circuitry is concerned, for the single-patch case, we select a capacitor with capacitance $C = 0.22\,\mu\text{F}$, and resistors $R_2 = 220\,\Omega$, $R_3 = 1500\,\Omega$, and $R_4 = 2200\,\Omega$. $R1$ is a potentiometer (Copal Electronics CT6EP102-ND) with tunable resistance ranging from $100\,\Omega$ to $1000\,\Omega$. By tuning the potentiometer, each piezo+RL circuit can resonate approximately between 2.5 and 8 kHz. A series resistor $R_s$ will also be used to connect the circuit to the positive electrode of the patch, to introduce dissipation in the system and to avoid unstable behavior.

Time-varying transient signals are imparted to the beam specimen by means of an electromechanical shaker (Brüel & Kjær Type 4810) and a stinger, that exert out-of-plane excitations that generate flexural waves. Signal generation and acquisition are performed through the same platform. The generated signals are amplified (amplifier type Brüel & Kjær Type 2718) before being sent to the shaker. The acquisition is carried out through a 3D Scanning Laser Doppler Vibrometer (3D-SLDV, model: Polytec PSV-400-3D), a non-contact measurement device capable of measuring the in-plane and out-of plane velocities at multiple points (one at a time) of the surface of a vibrating object. In our case, the measurement is made on the surface opposite to the one where the patch is bonded. The scanning grid comprises points in a range that extends from 30 cm to

the left to 30 cm to the right of the patch. To improve reflectivity, and therefore the quality of the optical measurements, the measured surface of the beam is painted with retro-reflective paint. The response to the chirp signal is recorded in time at a sampling frequency of 51.2 kHz. At each scan point, the measurement is repeated 10 or 15 times and averaged; a bandpass filter extending from 0.1 kHz to 16 kHz is also employed to minimize noise.

### 5.3.2 Wave response of the beam

The signals we use to probe the system are bursts, i.e. windowed sinusoids, which present a narrow-banded frequency spectrum about the carrier frequency (the frequency of the sinusoid). The first signal we consider is a 9-cycle burst with carrier frequency 3.5 kHz. The space-time evolution of this signal through the scanned region of the beam is shown in Fig. 5.4a. The response presents two main features. For $t < 4.5$ ms, we can see a

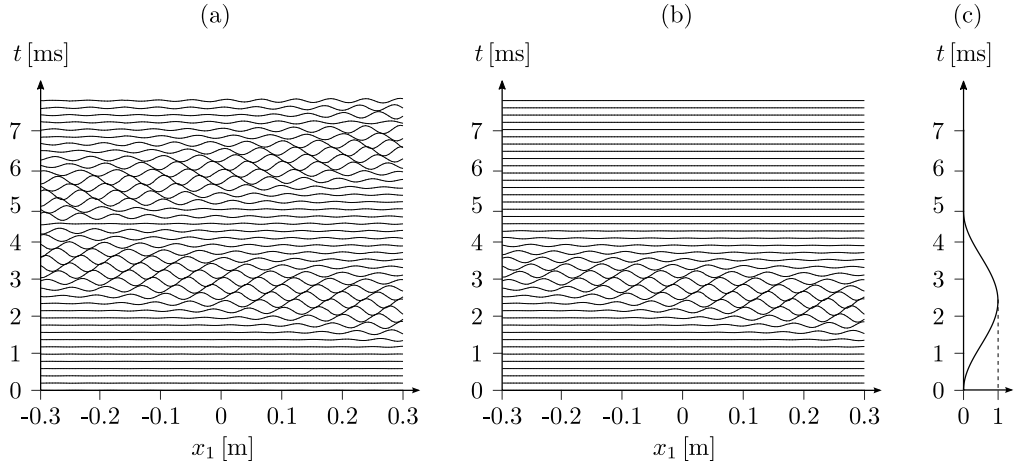


Figure 5.4: Spatio-temporal evolution of a 9-cycle burst with carrier frequency 3.5 kHz within the scanned region of the beam. (a) Pristine signal, featuring a left-going packet and a right-going boundary reflection. (b) Filtered signal, without boundary reflection. (c) Time-domain filter used to obtain (b) from (a).

left-going wave traveling from the source to the opposite clamp; for $t > 4.5$ ms, we can see a packet propagating towards the source due to boundary reflections. In order to eliminate the effects of the boundary from our problem and to be able to treat this as a pure propagating wave problem (i.e. lifting or mitigating the possibility for standing

waves to be established in the beam due to interference of incident and reflected waves), we apply the time-domain filter shown in Fig. 5.4c and obtain the filtered data shown in Fig. 5.4b. Since the separation between the two packets is not very pronounced, filtering will affect the signal for values of $x_1$ which are towards the left of the domain. A filtering procedure similar to this one will be applied to all the data obtained in these 1D experiments.

In order to evaluate the influence of the non-shunted piezoelectric patch on the beam response, we probe the beam with multiple 5-cycle burst signals centered at 1, 1.5, 2, 2.5, 3, 3.5, 4, 4.5, 5, 5.5 kHz. In this case, we use 5-cycle bursts to improve the separation between left-going and reflected waves and to assure that the signals are not distorted by our filtering procedure. For each burst, we apply the 2D Discrete Fourier Transform (DFT) to the recorded space-time data, and obtain a frequency versus wavenumber representation for the considered signal. Normalizing the response we obtain for each burst, and patching all the results together, we can reconstruct the dispersion relation as shown in Fig. 5.5. In this plot, the experimental data is reported as contours (there are

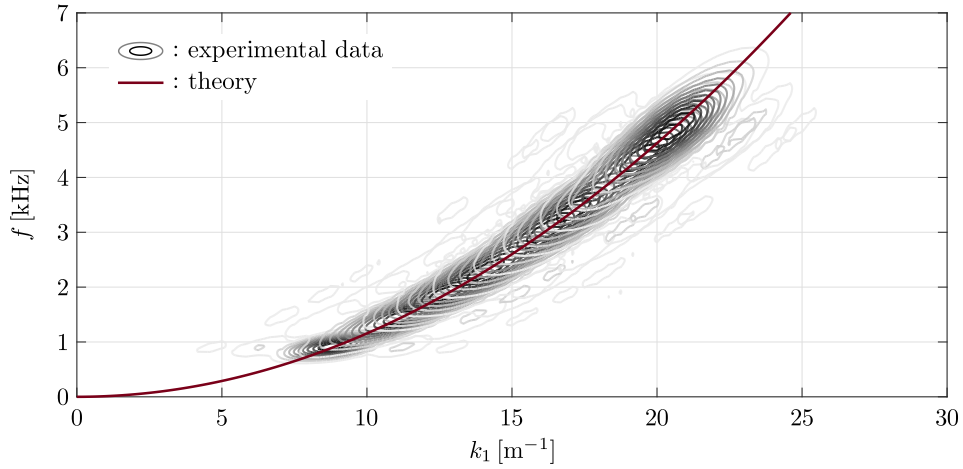


Figure 5.5: Comparison between the experimentally reconstructed dispersion relation for the beam featuring a single piezoelectric patch (gray-to-black contours, where the dark color indicates larger spectral values) and the dispersion branch calculated from beam theory (superimposed red line).

10 sets of contours, each one coming from one of the excitation signals mentioned above), where the darker lines correspond to larger values of the spectral amplitude $V_3$, i.e. the

Fourier transform of the out-of-plane velocity data $v_3$. This reconstructed dispersion portrait is compared to the theoretical dispersion relation for an Euler-Bernoulli beam (pristine, without piezoelectric patch), i.e.

$$\omega = k_1^2 \sqrt{\frac{EI}{\rho A}} \,, \tag{5.6}$$

where the Young's modulus of 6061 Aluminum is $E = 68\,\mathrm{GPa}$, its density is $\rho = 2700\,\mathrm{kg\,m^{-3}}$, the second moment of area is $I = (b\,t^3)/12$ and the cross-sectional area is $A = b\,t$ (the values given to $b$ and $t$ are those of the actual beam). The values of $k_1$ obtained from Eq. 5.6 are then normalized by $2\pi$, to obtain units of $\mathrm{m^{-1}}$ consistently with those obtained from the experimental data. The reconstructed and calculated dispersion relations match extremely well, and this highlights how the wave response of the beam is only marginally affected by the physical presence of the piezoelectric patch. In light of this, we can conclude that the electromechanical resonators obtained by shunting the piezo patch with RL circuits are extremely non-invasive—an aspect which is desirable in a spatial wave manipulation strategy, as discussed in Section 3.1.

### 5.3.3 Instability-enabled circuit tuning

In this work, precise tuning of the electromechanical resonators is achieved by exploiting some electrical instabilities that arise during the shunting process. When connecting a synthetic inductor to a piezoelectric patch, in the absence of a series resistor $R_s$, the system is unstable and this instability manifests as a vibration of the patch at the resonant frequency of the patch+circuit system. An audible manifestation of this instability is a "screaming" single-pitch noise coming from the patch. Instabilities need to be avoided because they generally cause a temperature increase that could damage the circuit components. This behavior, well known but seldom discussed in the literature, has also been documented by dell'Isola et al. [122]. For example, the black line in Fig. 5.6 represents the frequency spectrum of the signal recorded at one point of the beam when the only excitation causing the beam to vibrate is the self-driven instability-based vibration of the patch (no external excitation is provided). Note that the power necessary to generate these vibrations is given by the DC power supplies, that power the operational amplifiers in the synthetic inductors. Since the peak in this frequency

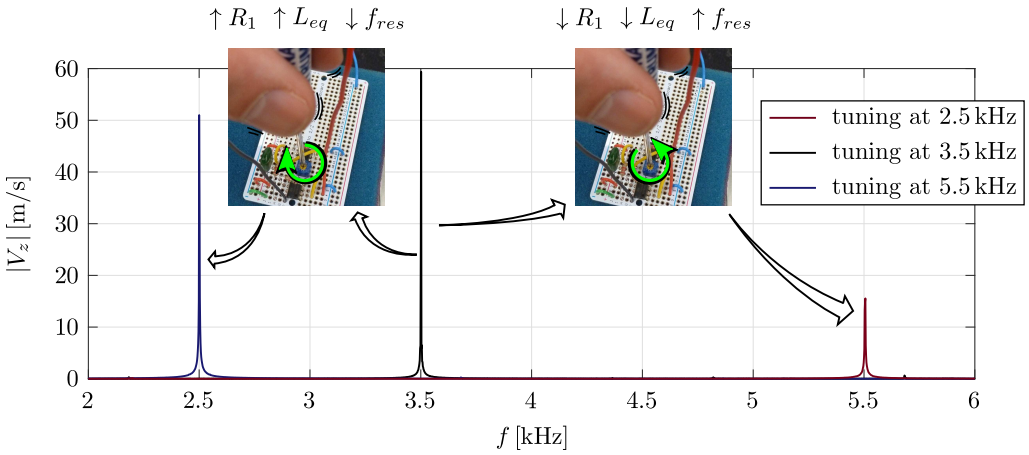


Figure 5.6: Illustration of the phenomenon of circuit instabilities, that manifest as self-excited single-frequency vibrations. Each one of the three superimposed lines corresponds to a different tuning frequency, which coincides with the location of the resonant peak.

response is correlated to the frequency at which the patch+shunt system is tuned, we can precisely tune the circuit at the frequency we want by acting on the potentiometer and by monitoring the position of this instability peak. The black line corresponds to a tuning frequency of 3.5 kHz. For example, if we want to change the tuning frequency to 2.5 kHz from 3.5 kHz, we increase the value of $R_1$ (rotating the potentiometer clockwise) and, therefore, we increase $L_{\text{eq}}$ while decreasing the resonant frequency of system. This way, we can move the instability peak towards lower frequencies, until it is positioned at the desired frequency, as shown by the blue line in Fig. 5.6. Similarly, we can rotate the potentiometer counterclockwise in order to, for example, move the tuning frequency of the system to 5.5 kHz (see the red line in Fig. 5.6). Note that, in order to avoid the afore-mentioned overheating of the circuit components, it is suggested not to keep shunt and circuit connected without $R_s$ for a long time. This instability-enabled procedure can substitute others that are based on the electrical testing of the synthetic inductor within a testing RLC circuit [121]—a procedure which heavily relies on the knowledge of the precise values of the circuit components and of the patch capacitance.

When using the electromechanical resonators to control elastic waves, we need to use a large enough series resistance in the shunting circuit in order to avoid instabilities. In the following, the resistance we use for the single-patch experiments is $R_s = 330\,\Omega$.

However, we noticed that this frequency value causes a shift in the resonant frequency of the electromechanical resonator with respect to the value predicted during any tuning procedure. For this reason, we should be mindful of this shift when programming our resonators and offset the tuning frequency accordingly. Note that, at the moment, we do not have a way to precisely predict what this shift amounts to, how it depends on $R_s$ and if it is constant across tuning frequencies.

### 5.3.4 Wave control with a single resonator

We now have all the ingredients to test how the shunt+patch system interacts with a propagating flexural wave. The excitation signal we use in this Section is the same 9-cycle burst with carrier frequency 3.5 kHz whose space-time evolution throughout the beam was shown in Fig. 5.4a. In order to evaluate the influence of the electromechanical resonator on the shape of the wave packet and its frequency content, we consider the response at a single point of the beam, located at $x_1 = -6.34$ cm (a point that is located between the patch and the clamp that is furthest away from the excitation location).

The time response of the beam at the location mentioned above, when the shunt+patch system is tuned as to resonate at 3.5 kHz, is shown in Fig. 5.7. In particular, Fig. 5.7a

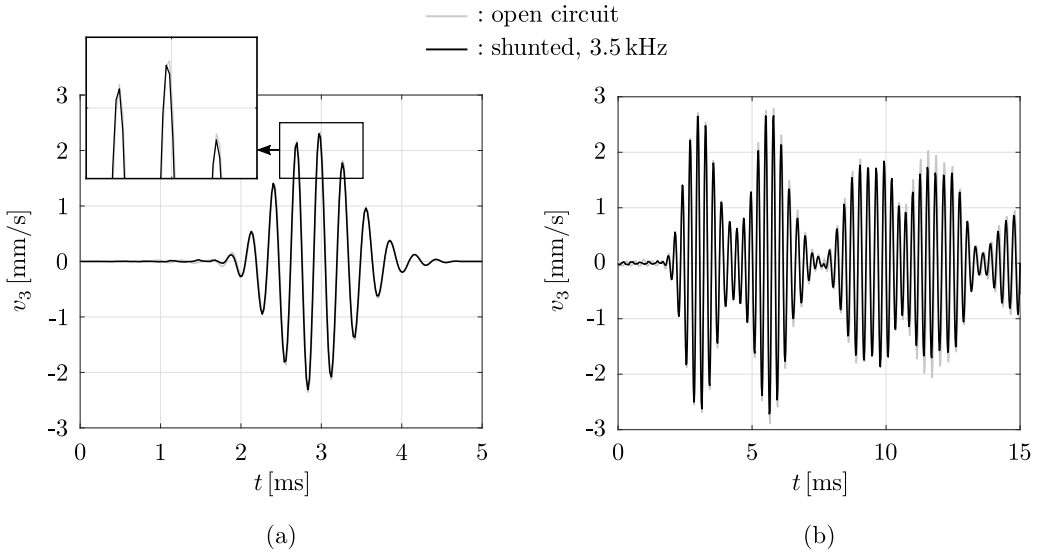


Figure 5.7: Influence of a single RL-shunted piezo, tuned at 3.5 kHz, on a 9-cycle burst signal with carrier frequency 3.5 kHz. (a) Filtered signal. (b) Unfiltered signal.

represents the evolution of the filtered time signal. From the detail, we can see that the shunt introduces a slight modification of the wave packet with respect to the open circuit case (gray line in the background). When looking at the evolution of the unfiltered signal in Fig. 5.7b, we can see that the difference between shunted and open circuit cases is more significant for the reflected wave packets (those that can be seen starting at 5 ms); this is due to the fact that those packets have interacted with the electromechanical resonator multiple times, thus having been more influenced by its presence.

To better understand how the shunted patch influences the characteristics of the wave packet, we now analyze its behavior in the frequency domain. In Fig. 5.8a, we show the frequency spectra of the filtered bursts recorded at the same measuring point for different shunting configurations. The light gray line corresponds to an open-circuit

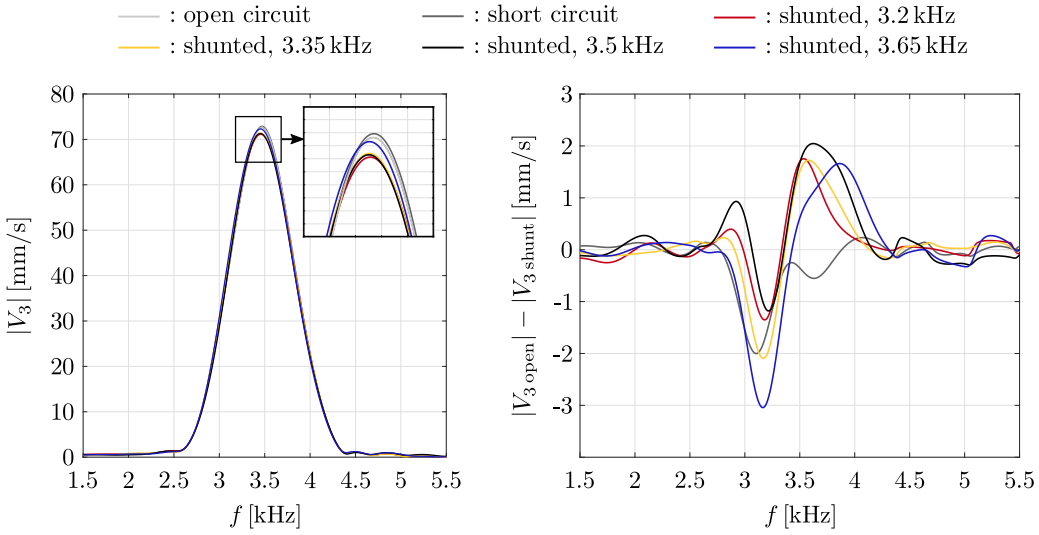


Figure 5.8: Influence of a single RL-shunted piezo, tuned at 3.2, 3.35, 3.5, 3.65 kHz or short circuited, on the frequency content of a 9-cycle burst signal with carrier frequency 3.5 kHz. (a) Frequency spectra, where the light gray line represents the baseline open circuit case. (b) Difference between the open circuit spectrum and each of the spectra obtained for the other shunting scenarios. Positive values represent attenuation while negative ones represent amplification with respect to the baseline case.

patch, and is used as "baseline" case. The dark gray line represents the short circuit case,

while the red, yellow, black and blue lines represent the responses obtained by tuning the electromechanical resonator at 3.2, 3.35, 3.5, 3.65 kHz, respectively. Note that we consider multiple tuning frequencies to demonstrate the tunability of our platform. From the insert in the figure, we can see that even simply connecting the patch's electrodes as in the short circuit case leads to a modification with respect to the open circuit scenario. However, the most significant modifications seem to take place for resonators tuned at 3.2, 3.35 and 3.5 kHz. To better evaluate the attenuating performance of the different shunting configurations, we plot in Fig. 5.8(b) the difference between the open circuit spectrum and each of the spectra for the shunted/shorted cases, versus frequency. Values greater than 0, in this plot, imply that the wave is attenuated, while values smaller than 0 correspond to amplification regions. The short circuit scenario clearly does not produce any attenuation with respect to the open circuit case. The shunted scenarios all produce some amplification around 3.1 kHz, followed by an attenuation region near 3.6 kHz. Consistently with our expectations, increasing the tuning frequency causes the attenuation region to be shifted towards higher frequencies. The black line, corresponding to a tuning frequency of 3.5 kHz, displays the most significant attenuation characteristics.

### 5.3.5 Tunable wave control with multiple resonators

To better appreciate the effects that tunable electromechanical resonators can have on a wave packet, we consider another specimen featuring multiple piezoelectric elements, each connected to a separate RL shunt [63, 123]. A detail of this multi-patch beam, analyzed by means of the same experimental setup illustrated in Fig. 5.2, is shown in Fig. 5.9. We can see that the specimen comprises seven patches, which are randomly

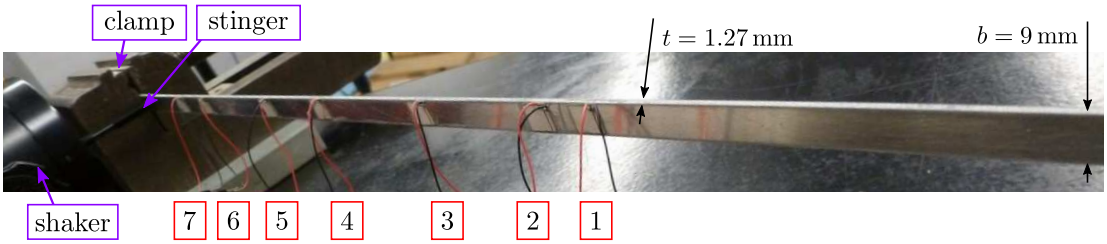


Figure 5.9: Detail of the beam in the multiple-patch configuration.

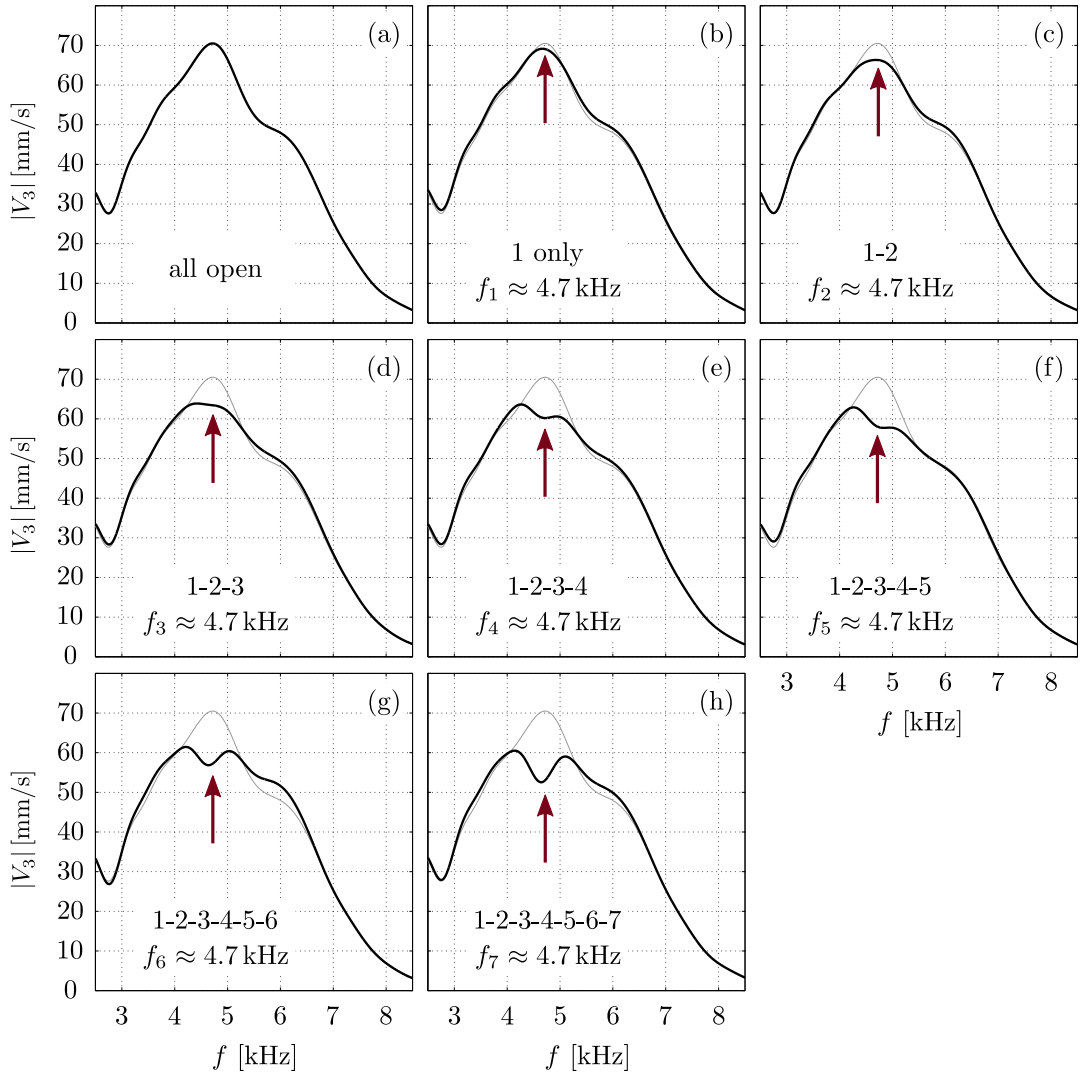


Figure 5.10: 2.5 kHz to 8.5 kHz chirp wave attenuation through *uniform* circuit tuning ($f_1 = f_2 = f_3 = f_4 = f_5 = f_6 = f_7$). The frames represent the DFT of the time signals recorded at successive stages of the activation sequence. (a) Open circuit response. (b-h) Response after the sequential shunting of patches 1, 2, 3, 4, 5, 6 and 7. The gray line in the background of (b-h) is the baseline open circuit case. The arrows indicate the frequencies at which the circuits are tuned (in this case, all arrows are overlapping).

placed along a region of the beam which is close to the excitation. We adopted a random arrangement to demonstrate that, in a linear wave control problem involving locally-resonant mechanisms, the location of the resonators is not influent on the wave

manipulation effects. Note that the characteristics of the beam and the patches are the same as in the previous experiment. In this case, however, we select a capacitor with capacitance $C = 0.22\,\mu$F, and resistors $R_2 = 680\,\Omega$, $R_3 = 1000\,\Omega$, and $R_4 = 1500\,\Omega$. By tuning the potentiometer, $R_1$, each piezo+RL circuit can now resonate approximately between 4 and 15 kHz.

In Fig. 5.10, we report the frequency spectrum of the beam response to a chirp signal, with frequency content linearly increasing from 2.5 to 8.5 kHz, recorded at a point which is located between the array of patches and the clamp which is furthest away from the wave source. In all plots, the baseline gray line represents the frequency spectrum of the signal in the open circuit case, also shown in Fig. 5.10a. All the other frames, from Fig. 5.10b to h, have been obtained by incrementally shunting all the patches in the domain. Note that all the shunted patches are tuned as to resonate at the same frequency, 4.7 kHz. Incrementally shunting multiple patches at the same time produces significant attenuation effects on the signal, as highlighted by the frame in Fig. 5.10h, where all the resonators are activated.

To offer a compelling piece of evidence on the tunability of our system, we now consider the same specimen and the same circuits, but we tune each potentiometer in each circuit as to shift the resonant frequencies of all electromechanical resonators to 6.5 kHz. We now probe the specimen with a chirp with frequency content linearly increasing from 4.5 to 10.5 kHz. The results in terms of frequency spectra of the recorded time histories at the same measurement point as in the previous case, obtained by incrementally shunting all the patches in the domain, are shown in Fig. 5.11. Also in this case, the wave attenuation caused by the action of multiple patches is quite significant.

As a side note, we also report some experimental results on the performance of the system when each shunt+patch pair is tuned at adjacent—yet not coincident—frequencies. A device of this type, capable of attenuating waves over a broader frequency range with respect to the uniform-shunting scenario, has been defined as a *rainbow trap* in the literature [24, 23, 63]. The attenuation performance of the beam, subjected to the same chirp with frequency content linearly increasing from 4.5 to 10.5 kHz used for the previous set of results, when the resonators are tuned at distinct frequencies in the 5.3 to 7.7 kHz, is shown in Fig. 5.12. With respect to the uniform-tuning results for the

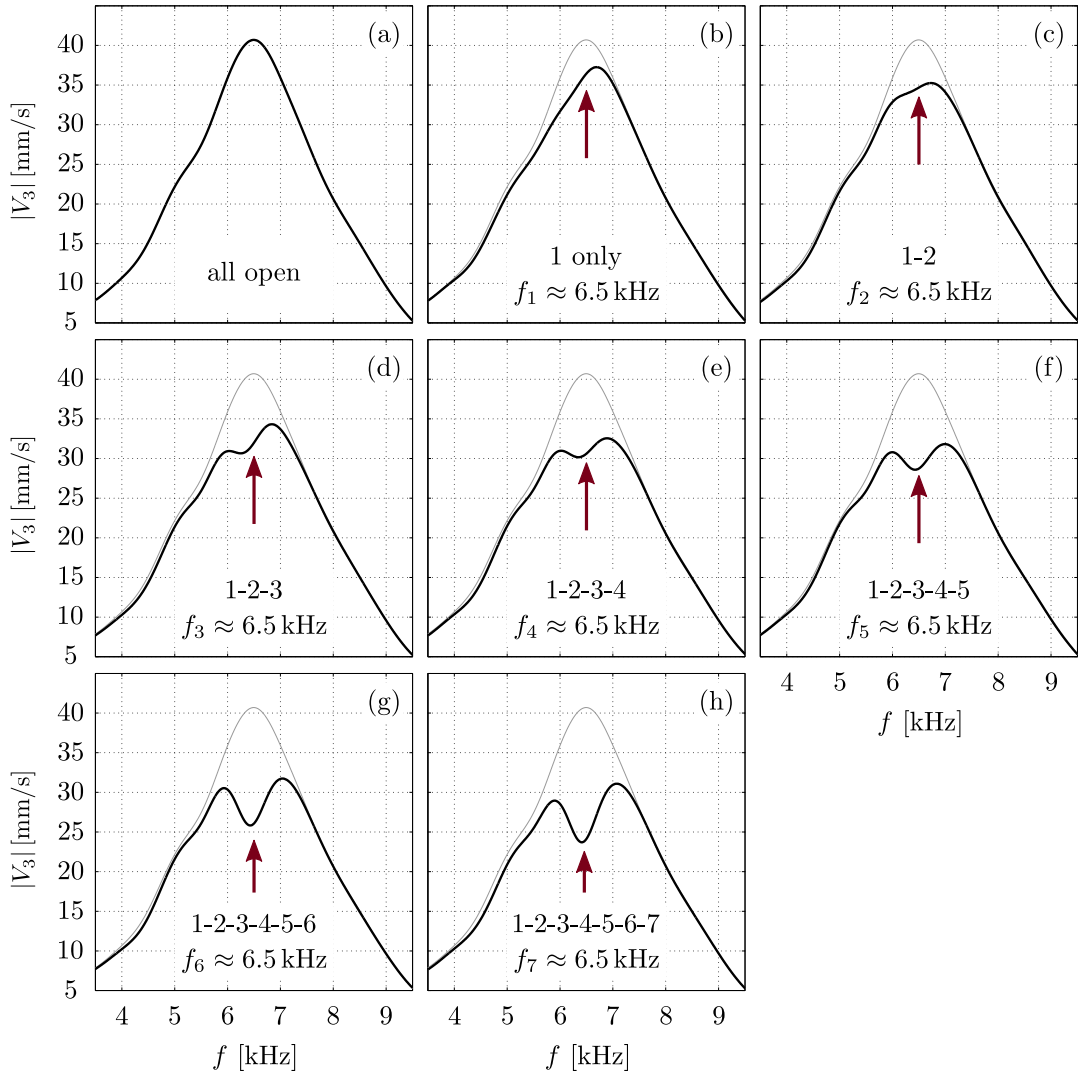


Figure 5.11: 4.5 kHz to 10.5 kHz chirp wave attenuation through *uniform* circuit tuning ($f_1 = f_2 = f_3 = f_4 = f_5 = f_6 = f_7$). (a) Open circuit response. (b-h) Response after the sequential shunting of patches 1, 2, 3, 4, 5, 6 and 7. The gray line in the background of (b-h) is the baseline open circuit case. The arrows indicate the frequencies at which the circuits are tuned (in this case, all arrows are overlapping).

same excitation signal, which were characterized by a marked dip around 6.5 kHz, the rainbow trap distills energy from a broader range of frequencies ranging from 5 kHz to 8 kHz. This broad attenuation comes at the expense of the attenuation intensity, which is clearly reduced. To conclude this aside, our tunable system based on RL-shunted

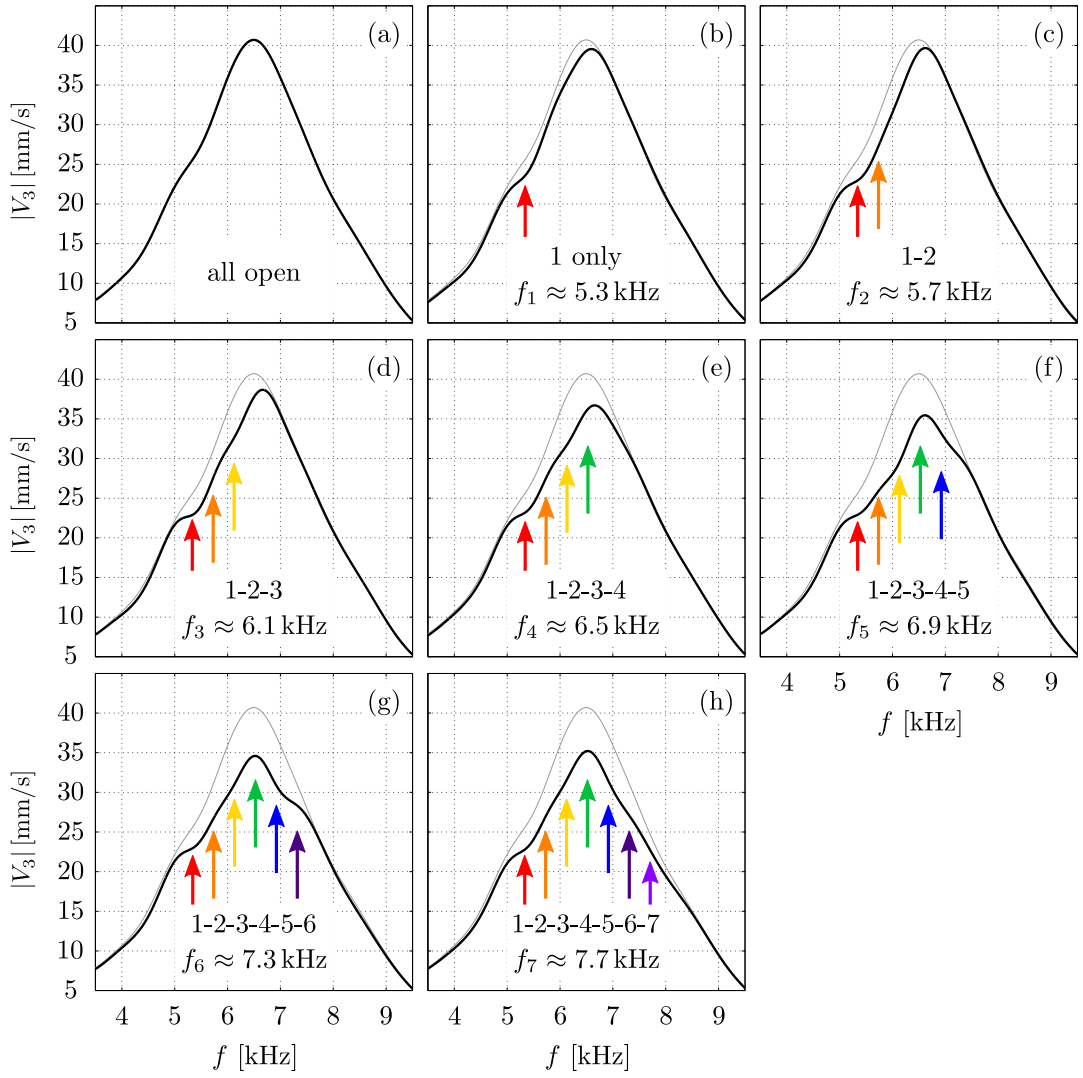


Figure 5.12: 4.5 kHz to 10.5 kHz chirp wave attenuation through *non-uniform* circuit tuning ($f_1 \neq f_2 \neq f_3 \neq f_4 \neq f_5 \neq f_6 \neq f_7$). (a) Open circuit response. (b-h) Response after the sequential shunting of patches 1, 2, 3, 4, 5, 6 and 7. The gray line in the background of (b-h) is the baseline open circuit case. The arrows indicate the frequencies at which the circuits are tuned.

arrays of patches is so flexible to allow targeting both a specific, critical frequency and a broad frequency range, depending on the application of interest.

## 5.4 Experiments on tunable anisotropy overriding

After providing a characterization of the behavior of electromechanical resonators consisting of piezoelectric patches shunted with resistor-inductor circuits in the context of a one-dimensional wave problem, we can now leverage the same tunable components to provide a proof of concept demonstration of anisotropy overriding in two-dimensional lattice structures. The problem we consider to validate our idea is that of flexural waves propagating in a square lattice.

### 5.4.1 Experimental setup

The setup for this experiment is shown in Fig. 5.13. Once again, we use the 3D-SLDV

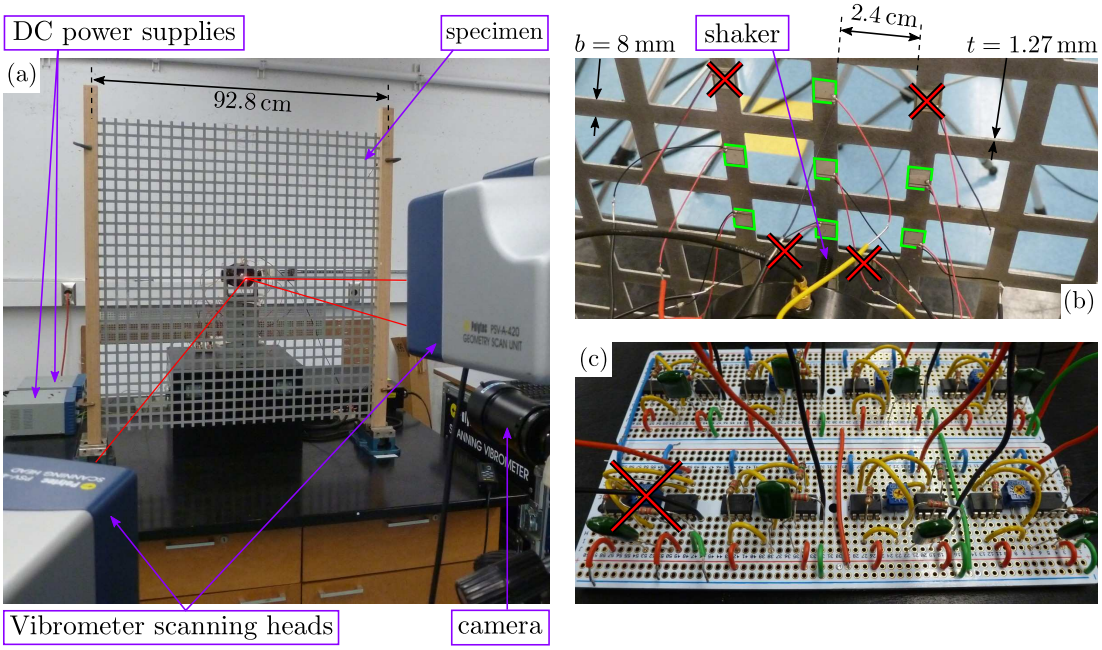


Figure 5.13: Experimental setup to test anisotropy overriding in a two-dimensional square lattice with RL+piezo resonators. (a) View of the specimen and of the measurement device. (b) Detail of the rear side of the specimen, near the excitation location (the patches bordered in green are the ones we use, while the crossed-out ones are not relevant to the experiments discussed in this venue). (c) Circuit board.

system to acquire the out-of-plane velocity at multiple locations of a specimen. The specimen is a two-dimensional square lattice structure, with unit cell size $L = 3.2\,\mathrm{cm}$

and strut width $b = 8\,\text{mm}$, obtained via water-jet cutting from a 1.27 mm-thick 6061 Al plate. Overall, the specimen comprises 29 $\times$ 29 unit cells, for a total size of 92.8 cm $\times$ 92.8 cm. Excitations are imparted to the center of the structure (as shown in Figs. 5.13a-b), through the same shaker-and-stinger assembly introduced in previous Sections. As shown in Fig. 5.13b, which captures a detail of the central portion of the rear side of the structure, the lattice features a number of piezoelectric patches bonded near the point of excitation. Of the many patches that are currently attached to our test specimen, we only activate seven (since, at this stage of our experimental campaign, seven is the maximum number of circuits that we are able to simultaneously power with our DC supplies). In Fig. 5.13b, the unused patches are crossed out, while the ones we employ are bordered by green boxes. Each patch is connected to a separate circuit (comprising a synthetic inductor and a series resistor). The circuit board, comprising the seven synthetic inductors we use throughout these experiments, is shown in Fig. 5.13c. The circuits have characteristics which are identical to those discussed in Section 5.3.1, i.e., each piezo+RL system can resonate approximately between 2.5 and 8 kHz. In each shunt, in order to avoid instabilities, we use a series resistance $R_s = 330\,\Omega$.

### 5.4.2 Numerical and experimental analysis of the pristine lattice

We now resort to a unit cell analysis to benchmark the wave behavior of the considered lattice architecture (pristine, without piezoelectric patches). The unit cell is modeled with Mindlin-Reissner plate elements, and we apply Bloch's periodicity-enforcing boundary conditions as discussed in Chapter 2. A sketch of the unit cell is shown in Fig. 5.14a. The low-frequency wave response of an infinite lattice is illustrated by the band diagram in Fig. 5.14b. We concentrate our attention on two modes of wave propagation: the red line is mode 1, while the the higher-frequency mode highlighted in blue is mode 2. To the trained eye, this band diagram immediately shows that the two modes display complementary anisotropic characteristics. Mode 1 features a partial bandgap along OA in the frequency range between 1.95 kHz and 2.75 kHz. This aspect, coupled to the fact that this is the only mode available in that specific frequency range, suggests that waves at these frequencies propagate mainly along OB (and along directions that are analogous to OB given the 2-fold symmetry of the lattice and of its response), i.e., along directions that are $\pm 45^{\text{o}}$-oriented with respect to the horizontal axis of the structure.

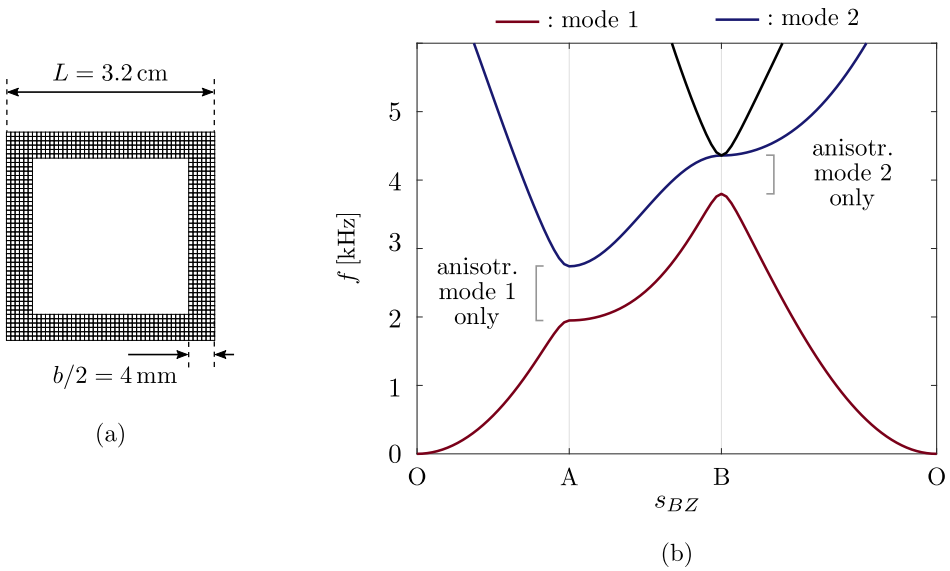


Figure 5.14: Flexural waves in the square lattice structure, from a unit cell analysis standpoint. (a) Unit cell, with its characteristic dimensions. (b) Band diagram, highlighting some frequency ranges of interest.

On the contrary, between 3.8 kHz and 4.4 kHz, waves adhere to the characteristics of mode 2 only, and propagate mainly along the horizontal and vertical axes of the structure (i.e. along OA, due to the presence of partial bandgaps impeding wave propagation along OB).

The predictions from the unit cell analysis are now validated experimentally by analyzing velocity wavefields obtained by spatially interpolating the data measured on a scanning grid comprising 16 × 16 unit cells around the center of the structure (where the excitation is applied). Note that, at this stage, all piezoelectric patches are open-circuited. The wavefields recorded at four time instants in response to a 11-cycle burst with carrier frequency 2.35 kHz—a frequency that falls in the middle of the partial bandgap of mode 1—are shown in Figs. 5.15a-d. The highly-beamed cross-shaped patterns we observe match our predictions from the unit-cell analysis (propagating, indeed, along $\pm 45^{\circ}$-oriented directions). The results in Figs. 5.15e-h show the response to a 11-cycle burst with carrier frequency 4.1 kHz—a frequency that corresponds to the middle of the partial bandgap of mode 2, in a region where this is the only existing mode. As expected, the wave profile presents complementary features with respect to those of

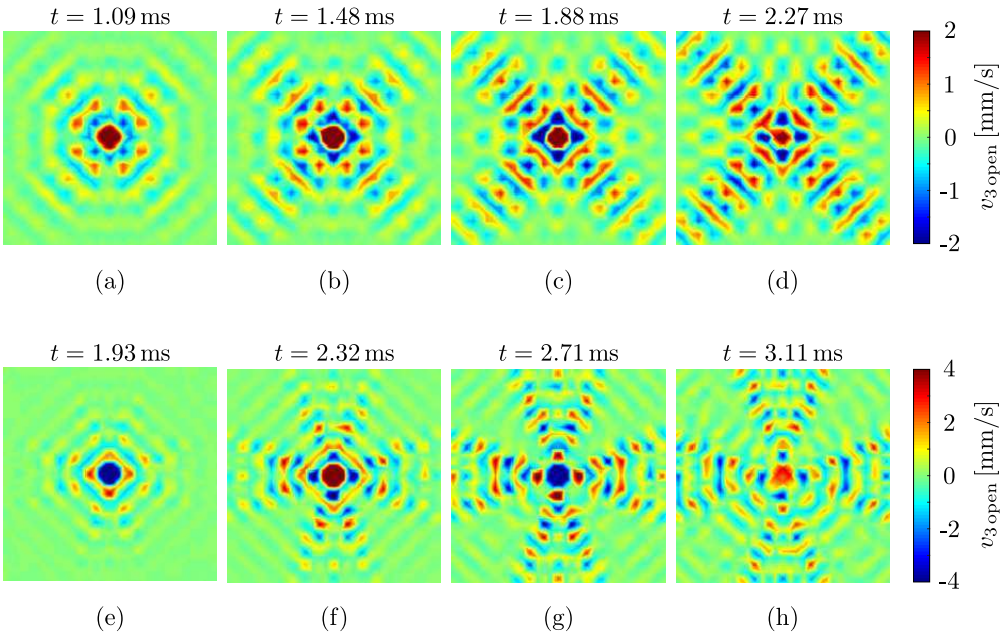


Figure 5.15: Experimentally-reconstructed anisotropic wavefields in our square lattice specimen. (a), (b), (c), (d) Response to a burst with 2.35 kHz carrier frequency. (e), (f), (g), (h) Response to a burst with 4.1 kHz carrier frequency.

mode 1: we now observe waves propagating mainly along the horizontal and vertical axes of the structure, as to form a cross pattern. All wavefields shown in Fig. 5.15, despite the specimen featuring non-symmetrically-placed piezoelectric patches, seem to obey the 2-fold symmetry of the pristine lattice architecture; in addition to the results on dispersion relation reconstruction for a beam with a piezo patch shown in Sec. 5.3.2, this represents another piece of evidence supporting the non-invasiveness of the extremely thin electromechanical resonators.

### 5.4.3 Preliminary results on anisotropy overriding

In this Section, we finally combine our knowledge of the anisotropy characteristics of the lattice and our understanding of piezoelectric patches shunted with resistor-inductor circuits in order to provide a first proof-of-concept demonstration of tunable anisotropy overriding. At this stage, we are only able to override the anisotropy characteristics of the cross-shaped mode 2. This is due to technological reasons: we found it challenging

to assemble sufficiently-stable shunts resonating below 3 kHz. The patch arrangement shown in Fig. 5.13b is actually designed to maximize interactions with a wave packet propagating upwards from the source/center of the lattice, similarly to the upward-going wave feature shown in Figs. 5.15e-h. To interact with a wave at these frequencies, the resonators are all tuned at 4.1 kHz, following the procedure discussed in Section 5.3.3. Fig. 5.16 shows the results on anisotropy overriding, including a comparison between open circuit and shunted cases. In Figs. 5.16a-d we report once again the wavefields at four time instants in the open circuit case. Figs. 5.16e-h, on the other hand, are the wavefields obtained when all the active patches are shunted with the aforementioned circuits. At a first glance, there seems to be little to no difference between the two sets of wavefields. In order to better quantify how and where the open and shunted results differ from each other, we plot the spatial evolution of the absolute value of the difference between the two wavefields, i.e., $|v_{3\,\mathrm{open}} - v_{3\,\mathrm{shunt}}|$ (where $v_{3\,\mathrm{open}}$ and $v_{3\,\mathrm{shunt}}$ are the open circuit and shunted responses, respectively). This spatio-temporal evolution is shown in Figs. 5.16i-l, where larger differences are darker in color. Clearly, the most significant modifications are observed in the region above the source. As a result, even though the effects are one order of magnitude smaller than the amplitude of the wave and therefore almost negligible at the macroscopic level, we were indeed able to correct the anisotropy of the medium as desired. Of course, a more systematical design of the electromechanical resonators (especially the circuits) could result in more pronounced effects (actually fully overriding the default anisotropy of the lattice), as would using simultaneously a larger number of resonators. By distributing patches along other directions, we would certainly be able to target other features of the anisotropic waves excited at 4.1 kHz. Finally, the presence of patches all around the source could allow us to fully leverage the reconfigurability of our tunable resonators and to target different anisotropic patterns at different frequencies through a single tunable platform.

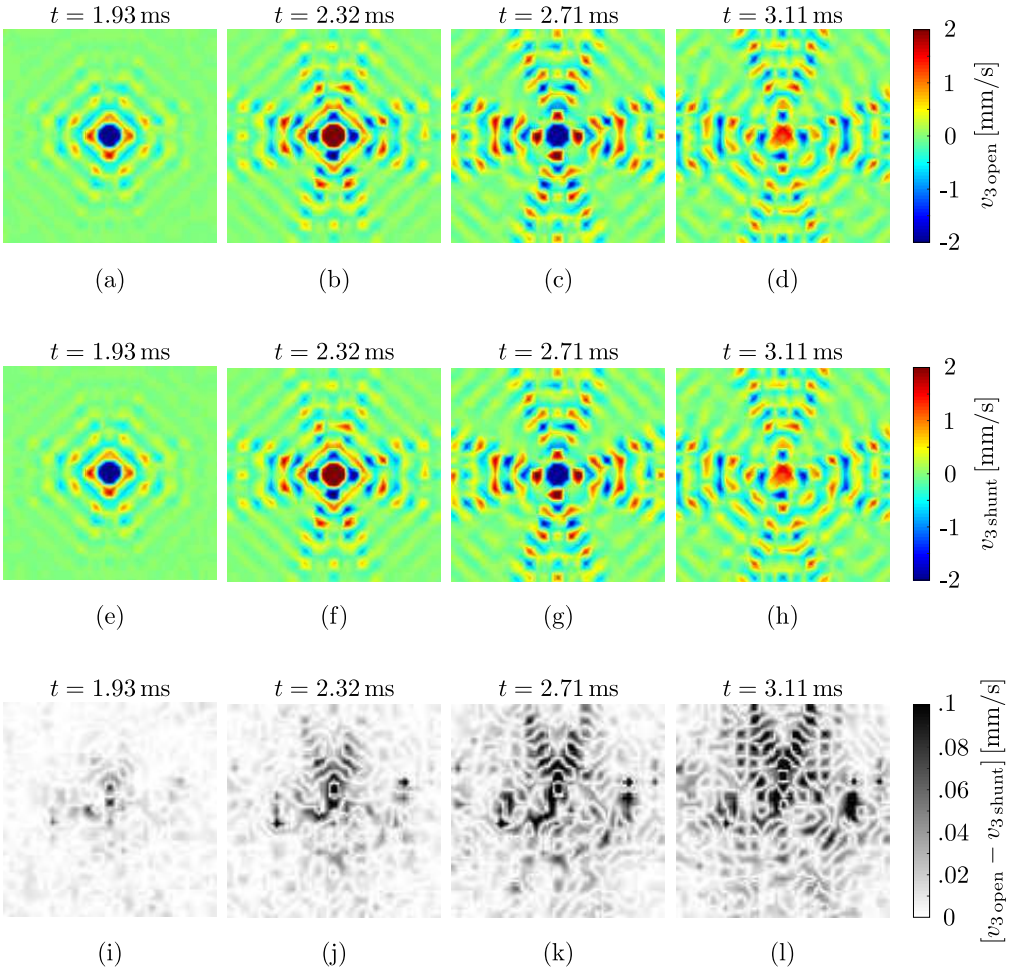


Figure 5.16: Preliminary experimental evidence of anisotropy overriding via tunable electromechanical resonators. All wavefields represent the response to a burst with 4.1 kHz carrier frequency. (a), (b), (c), (d) Open-circuit results. (e), (f), (g), (h) Lattice response when all the patches are shunted and tuned as to resonate at 4.1 kHz. (i), (j), (k), (l) Space-time evolution of the difference between the open circuit response and the shunted response. Dark regions indicate large resonators-induced modifications.

# Chapter 6

# Conclusions and future outlook

In this work, we have investigated the spatial wave manipulation capabilities of periodic cellular solids. In particular, our main aim has been to develop minimally invasive and tunable strategies to tailor and enhance their inherent, frequency-specific anisotropic wave behavior, while minimally affecting other functionalities.

The first strategy we proposed is based on the concept of relaxed cell symmetry. Our starting point is a lattice structure featuring a symmetric population of auxiliary microstructural elements—cantilevers stemming from each nodal location. By considering only selected cantilevers in each unit cell, it is possible to alter its symmetry landscape. This relaxation at the geometrical level produces a symmetry relaxation of the lattice's directional wave response. The most remarkable effect is a departure from the default highly-symmetric stellar nature of the response, to achieve wave patterns that present a clear principal direction of propagation. Since we adopt resonators that are auxiliary in nature, i.e. located at the nodes of the lattice, they only marginally effect the static properties of the cellular medium, making our strategy particularly enticing in applications where the wave management functionality should not interfere with other structural functionalities. We also propose and test numerically two avenues to attain tunable relaxed cell symmetry, both based on the inclusion of smart material inserts within the auxiliary microstructural elements. A first implementation is based on localized corrections of the mechanical properties; to this end, we explored the possibility of using piezoelectric elements connected (shunted) to negative capacitance circuits. By acting on a tunable resonator in the circuit, it is possible to alter the equivalent

Young's modulus of the corresponding piezoelectric element, thus affecting how elastic waves propagate through the smart lattice. Another implementation mentioned in this work, developed for soft polymeric lattices, involves reversible shape modifications enabled by electroactive polymer inserts; upon the application of an electric field, it is possible to curl the auxiliary resonators and to alter their dynamic characteristics. Selectively curling some resonators within each unit cell allows achieving tunable relaxed cell symmetry.

Motivated by technological limitations that prevented us from pursuing a proof of concept experimental validation of the tunable relaxed cell symmetry paradigm, we developed another strategy for spatial wave management that requires a much smaller number of resonators. This strategy, based on the idea of anisotropy overriding, relies on the interaction between the highly-beamed wave features of an anisotropic wave pattern and a network of strategically-located, tunable resonators. By tuning the resonators as to create landscapes of wave attenuation mechanisms at those frequencies where wave patterns are highly beamed, it is possible to override selected features of a propagating wavefield, thus enabling selective wave propagation along pre-determined directions. We demonstrated the potential of this strategy through numerical simulations, and we carried out some preliminary experimental tests using electromechanical resonators obtained by shunting piezoelectric patches with resistor-inductor circuits. We have also investigated in detail the behavior of these electromechanical resonators through simple one-dimensional experiments. Our results highlight that tunable spatial wave manipulation in smart cellular solids is achievable even by resorting to a limited number of resonators.

This work has illustrated the potential of smart cellular solids with reconfigurable wave and vibration control characteristics. Future efforts could be directed towards obtaining more tangible manipulation effects. This could be achieved by resorting to integrated manufacturing of the electromechanical resonators and improved circuitry, which would result in the possibility to simultaneously activate larger numbers of resonators. The adoption of other electromechanical (or magnetoelastic) resonators featuring a stronger coupling could be another plausible route to enhance the observed spatial manipulation effects. At the same time, to close the gap between fundamental research and practical applications, efforts should be directed towards broadening the

frequency ranges where spatial anisotropy is observed; in this sense, a number of available optimization techniques could play a crucial role in designing new metamaterial architectures with enhanced wave directivity capabilities.

# References


[1] L. Brillouin. *Wave propagation in periodic structures*. Dover Publications, second edition, 1953.

[2] E. Yablonovitch and T. J. Gmitter. Photonic band structure: The face-centered-cubic case. *Physical Review Letters*, 63(18):1950–1953, 1989.

[3] M.S. Kushwaha, P. Halevi, L. Dobrzynski, and B. Djafari-Rouhani. Acoustic band structure of periodic elastic composites. *Physical Review Letters*, 71(13):2022–2025, 1993.

[4] M. M. Sigalas and E. N. Economou. Band structure of elastic waves in two dimensional systems. *Solid State Communications*, 86(3):141–143, 1993.

[5] Robert F. Service. Next wave of metamaterials hopes to fuel the revolution. *Science*, 327(5962):138–139, 2010.

[6] D. R. Smith, Willie J. Padilla, D. C. Vier, S. C. Nemat-Nasser, and S. Schultz. Composite medium with simultaneously negative permeability and permittivity. *Physical Review Letters*, 84(18):4184–4187, 2000.

[7] R. Lakes. Foam structures with a negative poisson's ratio. *Science*, 235(4792):1038–1040, 1987.

[8] R. Lakes, T. Lee, A. Bersie, and Y. C. Wang. Extreme damping in composite materials with negative-stiffness inclusions. *Nature*, 410(1):565–567, 2001.

[9] Z. Liu, X. Zhang, Y. Mao, Y. Y. Zhu, Z. Yang, C. T. Chan, and P. Sheng. Locally resonant sonic materials. *Science*, 289(5485):1734–1736, 2000.

[10] H.H. Huang, C.T. Sun, and G.L. Huang. On the negative effective mass density in acoustic metamaterials. *International Journal of Engineering Science*, 47(4):610–617, 2009.

[11] M. I. Hussein, M. J. Leamy, and M. Ruzzene. Dynamics of phononic materials and structures: Historical origins, recent progress, and future outlook. *Applied Mechanics Reviews*, 66(4):040802, 2014.

[12] J. D. Joannopoulos, S. G. Johnson, J. N. Winn, and R. D. Meade. *Photonic crystals: Molding the flow of light*. Princeton University Press, second edition, 2008.

[13] V. G. Veselago. The electrodynamics of substances with simultaneously negative values of $\epsilon$ and $\mu$. *Soviet Physics Uspekhi*, 10(4):509, 1968.

[14] J.B. Pendry, A.J. Holden, D.J. Robbins, and W.J. Stewart. Magnetism from conductors and enhanced nonlinear phenomena. *IEEE Transactions on Microwave Theory and Techniques*, 47(11):2075–2084, 1999.

[15] F. Lemoult, N. Kaina, M. Fink, and G. Lerosey. Wave propagation control at the deep subwavelength scale in metamaterials. *Nature Physics*, 9(1):55–60, 2013.

[16] Y. Achaoui, V. Laude, S. Benchabane, and A. Khelif. Local resonances in phononic crystals and in random arrangements of pillars on a surface. *Journal of Applied Physics*, 114(10):104503, 2013.

[17] M. Rupin, F. Lemoult, G. Lerosey, and P. Roux. Experimental demonstration of ordered and disordered multiresonant metamaterials for lamb waves. *Physical Review Letters*, 112(23):234301, 2014.

[18] P. Celli and S. Gonella. Manipulating waves with LEGO® bricks: A versatile experimental platform for metamaterial architectures. *Applied Physics Letters*, 107(8):081901, 2015.

[19] Y. Pennec, B. Djafari-Rouhani, H. Larabi, J. O. Vasseur, and A. C. Hladky-Hennion. Low-frequency gaps in a phononic crystal constituted of cylindrical dots deposited on a thin homogeneous plate. *Physical Review B*, 78(10):104105, 2008.

[20] T.-T. Wu, Z.-G. Huang, T.-C. Tsai, and T.-C. Wu. Evidence of complete band gap and resonances in a plate with periodic stubbed surface. *Applied Physics Letters*, 93(11):111902, 2008.

[21] M. Oudich, M. Senesi, M. B. Assouar, M. Ruzenne, J.-H. Sun, B. Vincent, Z. Hou, and T.-T. Wu. Experimental evidence of locally resonant sonic band gap in two-dimensional phononic stubbed plates. *Physical Review B*, 84(16):165136, 2011.

[22] S. Brûlé, E. H. Javelaud, S. Enoch, and S. Guenneau. Experiments on seismic metamaterials: Molding surface waves. *Physical Review Letters*, 112(13):133901, 2014.

[23] S. Krödel, N. Thomé, and C. Daraio. Wide band-gap seismic metastructures. *Extreme Mechanics Letters*, 4:111–117, 2015.

[24] J. Zhu, Y. Chen, X. Zhu, F. J. Garcia-Vidal, X. Yin, W. Zhang, and X. Zhang. Acoustic rainbow trapping. *Scientific Reports*, 3:1728, 2013.

[25] A. Colombi, V. Ageeva, R. J. Smith, A. Clare, R. Patel, M. Clark, D. Colquitt, P. Roux, S. Guenneau, and R. V. Craster. Enhanced sensing and conversion of ultrasonic Rayleigh waves by elastic metasurfaces. *arXiv*, 1704.01553, 2017.

[26] M. Torres, F. R. Montero de Espinosa, D. García-Pablos, and N. García. Sonic band gaps in finite elastic media: Surface states and localization phenomena in linear and point defects. *Physical Review Letters*, 82(15):3054–3057, 1999.

[27] J. S. Jensen. Phononic band gaps and vibrations in one- and two-dimensional massspring structures. *Journal of Sound and Vibration*, 266(5):1053–1078, 2003.

[28] A. Khelif, A. Choujaa, S. Benchabane, B. Djafari-Rouhani, and V. Laude. Guiding and bending of acoustic waves in highly confined phononic crystal waveguides. *Applied Physics Letters*, 84(22):4400–4402, 2004.

[29] Y. Pennec, B. Djafari Rouhani, H. Larabi, A. Akjouj, J. N. Gillet, J. O. Vasseur, and G. Thabet. Phonon transport and waveguiding in a phononic crystal made up of cylindrical dots on a thin homogeneous plate. *Physical Review B*, 80(14):144302, 2009.

[30] M. Addouche, M. A. Al-Lethawe, A. Elayouch, and A. Khelif. Subwavelength waveguiding of surface phonons in pillars-based phononic crystal. *AIP Advances*, 4(12):124303, 2014.

[31] R.S. Langley. The response of two-dimensional periodic structures to point harmonic forcing. *Journal of Sound and Vibration*, 197(4):447–469, 1996.

[32] R.S. Langley, N.S. Bardell, and H.M. Ruivo. The response of two-dimensional periodic structures to harmonic point loading: A theoretical and experimental study of a beam grillage. *Journal of Sound and Vibration*, 207(4):521–535, 1997.

[33] M. Ruzzene, F. Scarpa, and F. Soranna. Wave beaming effects in two-dimensional cellular structures. *Smart Materials and Structures*, 12(3):363–372, 2003.

[34] S. Gonella and M. Ruzzene. Analysis of in-plane wave propagation in hexagonal and re-entrant lattices. *Journal of Sound and Vibration*, 312(1-2):125–139, 2008.

[35] A. Spadoni, M. Ruzzene, S. Gonella, and F. Scarpa. Phononic properties of hexagonal chiral lattices. *Wave Motion*, 46(7):435–450, 2009.

[36] A. S. Phani, J. Woodhouse, and N. A. Fleck. Wave propagation in two-dimensional periodic lattices. *The Journal of the Acoustical Society of America*, 119(4):1995–2005, 2006.

[37] F. Casadei and J.J. Rimoli. Anisotropy-induced broadband stress wave steering in periodic lattices. *International Journal of Solids and Structures*, 50(9):1402–1414, 2013.

[38] A. J. Zelhofer and D. M. Kochmann. On acoustic wave beaming in two-dimensional structural lattices. *International Journal of Solids and Structures*, pages –, 2017.

[39] P. Celli and S. Gonella. Laser-enabled experimental wavefield reconstruction in two-dimensional phononic crystals. *Journal of Sound and Vibration*, 333(1):114–123, 2014.

[40] P. Celli and S. Gonella. Low-frequency spatial wave manipulation via phononic crystals with relaxed cell symmetry. *Journal of Applied Physics*, 115(10):103502, 2014.

[41] J. Christensen and F. J. G. de Abajo. Anisotropic metamaterials for full control of acoustic waves. *Physical Review Letters*, 108(12):124301, 2012.

[42] R. Zhu, X. N. Liu, G. K. Hu, C. T. Sun, and G. L. Huang. Negative refraction of elastic waves at the deep-subwavelength scale in a single-phase metamaterial. *Nature Communications*, 5:5510, 2014.

[43] S. Yang, J. H. Page, Z. Liu, M. L. Cowan, C. T. Chan, and P. Sheng. Focusing of sound in a 3d phononic crystal. *Physical Review Letters*, 93(2):024301, 2004.

[44] A. Sukhovich, L. Jing, and J. H. Page. Negative refraction and focusing of ultrasound in two-dimensional phononic crystals. *Physical Review B*, 77(1):014301, 2008.

[45] J. Bucay, E. Roussel, J. O. Vasseur, P. A. Deymier, A-C. Hladky-Hennion, Y. Pennec, K. Muralidharan, B. Djafari-Rouhani, and B. Dubus. Positive, negative, zero refraction, and beam splitting in a solid/air phononic crystal: Theoretical and experimental study. *Physical Review B*, 79(21):214305, 2009.

[46] V. M. García-Chocano, J. Christensen, and J. Sánchez-Dehesa. Negative refraction and energy funneling by hyperbolic materials: An experimental demonstration in acoustics. *Physical Review Letters*, 112(14):144301, 2014.

[47] J.-F. Robillard, J. Bucay, P. A. Deymier, A. Shelke, K. Muralidharan, B. Merheb, J. O. Vasseur, A. Sukhovich, and J. H. Page. Resolution limit of a phononic crystal superlens. *Physical Review B*, 83(22):224301, 2011.

[48] C. Goffaux and J. P. Vigneron. Theoretical study of a tunable phononic band gap system. *Physical Review B*, 64(7):075118, 2001.

[49] S-C. S. Lin and T. J. Huang. Tunable phononic crystals with anisotropic inclusions. *Physical Review B*, 83(17):174303, 2011.

[50] V. Romero-Garcìa, C. Lagarrigue, J-P. Groby, O. Richoux, and V. Tournat. Tunable acoustic waveguides in periodic arrays made of rigid square-rod scatterers: theory and experimental realization. *Journal of Physics D: Applied Physics*, 46(30):305108, 2013.

[51] F. Lemoult, M. Fink, and G. Lerosey. Acoustic resonators for far-field control of sound on a subwavelength scale. *Physical Review Letters*, 107(6):064301, 2011.

[52] O. Thorp, M. Ruzzene, and A. Baz. Attenuation and localization of wave propagation in rods with periodic shunted piezoelectric patches. *Smart Materials and Structures*, 10(5):979–989, 2001.

[53] A. Spadoni, M. Ruzzene, and K. A. Cunefare. Vibration and wave propagation control of plates with periodic arrays of shunted piezoelectric patches. *Journal of Intelligent Material Systems and Structures*, 20(8):979–990, 2009.

[54] F. Casadei, M. Ruzzene, L. Dozio, and K. A. Cunefare. Broadband vibration control through periodic arrays of resonant shunts: experimental investigation on plates. *Smart Materials and Structures*, 19(1):015002, 2010.

[55] L. Airoldi and M. Ruzzene. Design of tunable acoustic metamaterials through periodic arrays of resonant shunted piezos. *New Journal of Physics*, 13(11):113010, 2011.

[56] J. H. Oh, K. I. Lee, P. S. Ma, and Y. Y. Kim. Active wave-guiding of piezoelectric phononic crystals. *Applied Physics Letters*, 99(8):083505, 2011.

[57] G. Wang, S. Chen, and J. Wen. Low-frequency locally resonant band gaps induced by arrays of resonant shunts with antoniou's circuit: experimental investigation on beams. *Smart Materials and Structures*, 20(1):015026, 2011.

[58] F. Casadei, T. Delpero, A. Bergamini, P. Ermanni, and M. Ruzzene. Piezoelectric resonator arrays for tunable acoustic waveguides and metamaterials. *Journal of Applied Physics*, 112(6):064902, 2012.

[59] A. Bergamini, T. Delpero, L. De Simoni, L. De Lillo, M. Ruzzene, and P. Ermanni. Phononic crystal with adaptive connectivity. *Advanced Materials*, 26(9):1343–1347, 2014.

[60] Y. Y. Chen, G. L. Huang, and C. T. Sun. Band gap control in an active elastic metamaterial with negative capacitance piezoelectric shunting. *Journal of Vibration and Acoustics*, 136(6):061008, 2014.

[61] P. Celli and S. Gonella. Tunable directivity in metamaterials with reconfigurable cell symmetry. *Applied Physics Letters*, 106(9):091905, 2015.

[62] K. Yi, M. Collet, M. Ichchou, and L. Li. Flexural waves focusing through shunted piezoelectric patches. *Smart Materials and Structures*, 25(7):075007, 2016.

[63] D. Cardella, P. Celli, and S. Gonella. Manipulating waves by distilling frequencies: a tunable shunt-enabled rainbow trap. *Smart Materials and Structures*, 25(8):085017, 2016.

[64] W.-P. Yang and L.-W. Chen. The tunable acoustic band gaps of two-dimensional phononic crystals with a dielectric elastomer cylindrical actuator. *Smart Materials and Structures*, 17(1):015011, 2008.

[65] M. Gei, S. Roccabianca, and M. Bacca. Controlling bandgap in electroactive polymer-based structures. *IEEE/ASME Transactions on Mechatronics*, 16(1):102–107, 2011.

[66] M. A. Nouh, O. J. Aldraihem, and A. Baz. Periodic metamaterial plates with smart tunable local resonators. *Journal of Intelligent Material Systems and Structures*, 27(13):1829–1845, 2016.

[67] R. Getz, D. M. Kochmann, and G. Shmuel. Voltage-controlled complete stopbands in two-dimensional soft dielectrics. *International Journal of Solids and Structures*, 113-114:24–36, 2017.

[68] P. Celli, S. Gonella, V. Tajeddini, A. Muliana, S. Ahmed, and Z. Ounaies. Wave control through soft microstructural curling: bandgap shifting, reconfigurable

anisotropy and switchable chirality. *Smart Materials and Structures*, 26(3):035001, 2017.

[69] J.-F. Robillard, O. Bou Matar, J. O. Vasseur, P. A. Deymier, M. Stippinger, A.-C. Hladky-Hennion, Y. Pennec, and B. Djafari-Rouhani. Tunable magnetoelastic phononic crystals. *Applied Physics Letters*, 95(12):124104, 2009.

[70] O. Bou Matar, J. F. Robillard, J. O. Vasseur, A.-C. Hladky-Hennion, P. A. Deymier, P. Pernod, and V. Preobrazhensky. Band gap tunability of magneto-elastic phononic crystal. *Journal of Applied Physics*, 111(5):054901, 2012.

[71] M. Schaeffer and M. Ruzzene. Wave propagation in multistable magneto-elastic lattices. *International Journal of Solids and Structures*, 56-57:78–95, 2015.

[72] M. Schaeffer and M. Ruzzene. Wave propagation in reconfigurable magneto-elastic kagome lattice structures. *Journal of Applied Physics*, 117(19):194903, 2015.

[73] J.-Y. Yeh. Control analysis of the tunable phononic crystal with electrorheological material. *Physica B: Condensed Matter*, 400(1-2):137–144, 2007.

[74] Z. Xu, F. Wu, and Z. Guo. Shear-wave band gaps tuned in two-dimensional phononic crystals with magnetorheological material. *Solid State Communications*, 154:43–45, 2013.

[75] M. Ruzzene and A. Baz. Control of wave propagation in periodic composite rods using shape memory inserts. *Journal of Vibration and Acoustics*, 122(2):151–159, 2000.

[76] E. Walker, D. Reyes, M. M. Rojas, A. Krokhin, Z. Wang, and A. Neogi. Tunable ultrasonic phononic crystal controlled by infrared radiation. *Applied Physics Letters*, 105(14):143503, 2014.

[77] F. Casadei and K. Bertoldi. Wave propagation in beams with periodic arrays of airfoil-shaped resonating units. *Journal of Sound and Vibration*, 333(24):6532–6547, 2014.

[78] K. Bertoldi and M. C. Boyce. Mechanically triggered transformations of phononic band gaps in periodic elastomeric structures. *Physical Review B*, 77(5):052105, 2008.

[79] P. Wang, J. Shim, and K. Bertoldi. Effects of geometric and material nonlinearities on tunable band gaps and low-frequency directionality of phononic crystals. *Physical Review B*, 88(1):014304, 2013.

[80] P. Wang, F. Casadei, S. Shan, J. C. Weaver, and K. Bertoldi. Harnessing buckling to design tunable locally resonant acoustic metamaterials. *Physical Review Letters*, 113(1):014301, 2014.

[81] S. Rudykh and M. C. Boyce. Transforming wave propagation in layered media via instability-induced interfacial wrinkling. *Physical Review Letters*, 112(3):034301, 2014.

[82] A. Bayat and F. Gordaninejad. Band-gap of a soft magnetorheological phononic crystal. *Journal of Vibration and Acoustics*, 137(1):011011, 2015.

[83] A. Spadoni and C. Daraio. Generation and control of sound bullets with a nonlinear acoustic lens. *Proceedings of the National Academy of Sciences*, 107(16):7230–7234, 2010.

[84] R. Narisetti. A perturbation approach for predicting wave propagation in one-dimensional nonlinear periodic structures. *Journal of Vibration and Acoustics*, 132(3):031001, 2010.

[85] R. Narisetti. A perturbation approach for analyzing dispersion and group velocities in two-dimensional nonlinear periodic lattices. *Journal of Vibration and Acoustics*, 133(6):061020, 2011.

[86] C. M. Donahue, P. W. J. Anzel, L. Bonanomi, T. A. Keller, and C. Daraio. Experimental realization of a nonlinear acoustic lens with a tunable focus. *Applied Physics Letters*, 104(1):014103, 2014.

[87] C. Coste, E. Falcon, and S. Fauve. Solitary waves in a chain of beads under hertz contact. *Physical Review E*, 56(5):6104–6117, 1997.

[88] C. Daraio, V. F. Nesterenko, E. B. Herbold, and S. Jin. Tunability of solitary wave properties in one-dimensional strongly nonlinear phononic crystals. *Physical Review E*, 73(2):026610, 2006.

[89] R. Martinez-Sala, J. Sancho, and J. V. Sanchez. Sound attenuation by sculpture. *Nature*, 378:241, 1995.

[90] N. A. Fleck, V. S. Deshpande, and M. F. Ashby. Micro-architectured materials: past, present and future. *Proceedings of the Royal Society A*, 466(2121):2495–2516, 2010.

[91] E. Baravelli and M. Ruzzene. Internally resonating lattices for bandgap generation and low-frequency vibration control. *Journal of Sound and Vibration*, 332(25):6562–6579, 2013.

[92] T. A. Schaedler, A. J. Jacobsen, A. Torrents, A. E. Sorensen, J. Lian, J. R. Greer, L. Valdevit, and W. B. Carter. Ultralight metallic microlattices. *Science*, 334(6058):962–965, 2011.

[93] X. Zheng, H. Lee, T. H. Weisgraber, M. Shusteff, J. DeOtte, E. B. Duoss, J. D. Kuntz, M. M. Biener, Q. Ge, J. A. Jackson, S. O. Kucheyev, N. X. Fang, and C. M. Spadaccini. Ultralight, ultrastiff mechanical metamaterials. *Science*, 344(6190):1373–1377, 2014.

[94] L. R. Meza, S. Das, and J. R. Greer. Strong, lightweight, and recoverable three-dimensional ceramic nanolattices. *Science*, 345(6202):1322–1326, 2014.

[95] P. G. Martinsson and A. B. Movchan. Vibrations of lattice structures and phononic band gaps. *The Quarterly Journal of Mechanics and Applied Mathematics*, 56(1):45–64, 2003.

[96] M. Ruzzene, L. Mazzarella, P. Tsopelas, and F. Scarpa. Wave propagation in sandwich plates with periodic auxetic core. *Journal of Intelligent Material Systems and Structures*, 13(9):587–597, 2002.

[97] M. Ruzzene. Vibration and sound radiation of sandwich beams with honeycomb truss core. *Journal of Sound and Vibration*, 277(45):741–763, 2004.

[98] A. Spadoni, M. Ruzzene, S. Gonella, and F. Scarpa. Phononic properties of hexagonal chiral lattices. *Wave Motion*, 46(7):435–450, 2009.

[99] G. Trainiti, J.J. Rimoli, and M. Ruzzene. Wave propagation in undulated structural lattices. *International Journal of Solids and Structures*, 97-98:431–444, 2016.

[100] S. M. Jeong and M. Ruzzene. Experimental analysis of wave propagation in periodic grid-like structures. *Smart Structures and Materials*, 5760(404):518–525, 2005.

[101] S. Gonella, A. C. To, and W. K. Liu. Interplay between phononic bandgaps and piezoelectric microstructures for energy harvesting. *Journal of the Mechanics and Physics of Solids*, 57(3):621–633, 2009.

[102] S. Krödel, T. Delpero, A. Bergamini, P. Ermanni, and D. M. Kochmann. 3d auxetic microlattices with independently controllable acoustic band gaps and quasistatic elastic moduli. *Advanced Engineering Materials*, 16(4):357–363, 2014.

[103] P. Wang, F. Casadei, S. H. Kang, and K. Bertoldi. Locally resonant band gaps in periodic beam lattices by tuning connectivity. *Physical Review B*, 91(2):020103, 2015.

[104] A. Spadoni, R. Höhler, S. Cohen-Addad, and V. Dorodnitsyn. Closed-cell crystalline foams: Self-assembling, resonant metamaterials. *The Journal of the Acoustical Society of America*, 135(4):1692–1699, 2014.

[105] V. F. Chernow, H. Alaeian, J. A. Dionne, and J. R. Greer. Polymer lattices as mechanically tunable 3-dimensional photonic crystals operating in the infrared. *Applied Physics Letters*, 107(10):101905, 2015.

[106] A. Spadoni, M. Ruzzene, and F. Scarpa. Dynamic response of chiral truss-core assemblies. *Journal of Intelligent Material Systems and Structures*, 17(11):941–952, 2006.

[107] Y. Liebold-Ribeiro and C. Körner. Phononic band gaps in periodic cellular materials. *Advanced Engineering Materials*, 16(3):328–334, 2014.

[108] N.C. Perkins and C.D. Mote. Comments on curve veering in eigenvalue problems. *Journal of Sound and Vibration*, 106(3):451–463, 1986.

[109] A.-C. Hladky-Hennion, J. O. Vasseur, G. Haw, C. Croënne, L. Haumesser, and A. N. Norris. Negative refraction of acoustic waves using a foam-like metallic structure. *Applied Physics Letters*, 102(14):144103, 2013.

[110] E. B. Tadmor and R. E. Miller. *Modeling Materials: Continuum, Atomistic, and Multiscale Techniques*. Cambridge University Press, 2011.

[111] G. Trainiti and M. Ruzzene. Non-reciprocal elastic wave propagation in spatiotemporal periodic structures. *New Journal of Physics*, 18(8):083047, 2016.

[112] R. L. Forward. Electronic damping of vibrations in optical structures. *Applied Optics*, 18(5):690–697, 1979.

[113] N. W. Hagood and A. von Flotow. Damping of structural vibrations with piezoelectric materials and passive electrical networks. *Journal of Sound and Vibration*, 146(2):243–268, 1991.

[114] B. S. Beck. *Negative capacitance shunting of piezoelectric patches for vibration control of continuous systems*. PhD thesis, Georgia Institute of Technology, December 2012.

[115] B. S. Beck, K. A. Cunefare, M. Ruzzene, and M. Collet. Experimental analysis of a cantilever beam with a shunted piezoelectric periodic array. *Journal of Intelligent Material Systems and Structures*, 22(11):1177–1187, 2011.

[116] B. S. Beck, K. A. Cunefare, and M. Collet. The power output and efficiency of a negative capacitance shunt for vibration control of a flexural system. *Smart Materials and Structures*, 22(6):065009, 2013.

[117] K. Jia, M. Wang, T. Lu, J. Zhang, and T. Wang. Band-gap tunable dielectric elastomer filter for low frequency noise. *Smart Materials and Structures*, 25(5):055047, 2016.

[118] P. I. Galich and S. Rudykh. Manipulating pressure and shear waves in dielectric elastomers via external electric stimuli. *International Journal of Solids and Structures*, 91:18–25, 2016.

[119] N. S. Sigamani, S. Ahmed, and Z. Ounaies. Effect of processing conditions on the microstructure and electromechanical response of PVDF TrFE CTFE terpolymers. *Proceedings of ASME SMASIS 2014*, 1:V001T01A030, 2014.

[120] A. Antoniou. Realisation of gyrators using operational amplifiers, and their use in rc-active-network synthesis. *Proceedings of the Institution of Electrical Engineers*, 116(11):1838–1850, 1969.

[121] F. A. C. Viana and J. V. Steffen. Multimodal vibration damping through piezoelectric patches and optimal resonant shunt circuits. *Journal of the Brazilian Society of Mechanical Sciences and Engineering*, 28:293–310, 2006.

[122] F. dell'Isola, C. Maurini, and M. Porfiri. Passive damping of beam vibrations through distributed electric networks and piezoelectric transducers: prototype design and experimental validation. *Smart Materials and Structures*, 13(2):299, 2004.

[123] W. Zhang, P. Celli, D. Cardella, and S. Gonella. A disorder-based strategy for tunable, broadband wave attenuation. *Proc. SPIE*, 10170:101700F, 2017.

# Appendix A

# Beam vs. 2D elasticity models at nodal locations

In this appendix, we discuss whether it is reasonable or not to resort to beam elements when modeling lattice structures featuring populations of auxiliary microstructures. The reason why modeling this specific type of structures could lead to some issues can be understood from Fig. A.1b, which represents a detail of one of the nodal locations of Fig. A.1a (where $L_c = 0.8L$ and $t_c = 3t$). When using beam elements, all the information

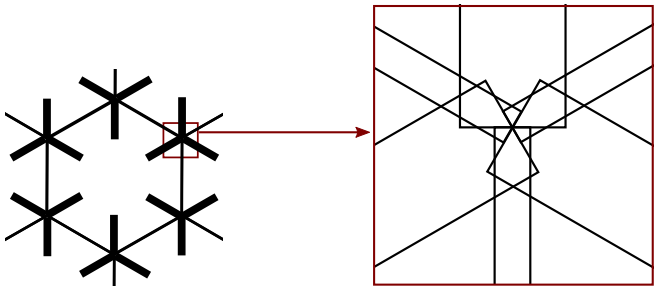

(a) (b)

Figure A.1: (a) Schematic of one of the cells of a lattice with a symmetric population of cantilevers ($L_c = 0.8L$, $t_c = 3t$). (b) Detail of one of the nodal locations.

on the cross sectional properties is carried by points on the neutral axis. For this reason, junctions between beams are treated as points, neglecting their inevitably bulky nature.

To investigate whether the beam model correctly captures what takes place at these

junctions, we compare the band diagrams obtained for two different finite element models of the same architecture (shown in Fig. A.1a). This comparison is shown in Fig. A.2, where the dashed lines correspond to a 2D FE model (4-node isoparametric quadrilaterals) and the continuous lines to a Timoshenko beam model (considering 10 elements per link). We can see that the two dispersion relations showcase very similar features, with

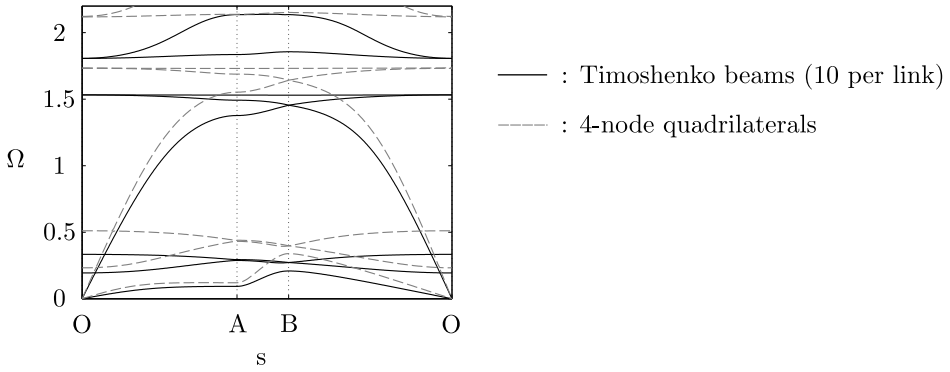


Figure A.2: Comparison between band diagrams for the configuration in Fig. A.1a, obtained with a 2D model (dashed lines) and a Timoshenko beam model (continuous lines).

the only difference being that, in the 2D elasticity model, all the curves are stretched over a larger frequency range. In particular, we can see that the bandgap located around $\Omega = 1.7$ in the beam model is shifted upwards in the 2D model (around $\Omega = 2$). From these observations, we can conclude that the auxiliary cantilevers and the lattice links in the 2D model appear to be stiffer than in the beam-based model. This stiffening is due to the fact that, in the 2D case, due to the presence of a bulky region around the junctions, the effective length of the beams is reduced.